



HAL
open science

Nanoparticules lipidiques de type Janus à compartiment superparamagnétique : du procédé de mise en oeuvre aux applications théranostiques

Elodie Millart

► To cite this version:

Elodie Millart. Nanoparticules lipidiques de type Janus à compartiment superparamagnétique : du procédé de mise en oeuvre aux applications théranostiques. Pharmacie galénique. Université Paris Saclay (COmUE), 2017. Français. NNT : 2017SACLS540 . tel-01982799

HAL Id: tel-01982799

<https://theses.hal.science/tel-01982799>

Submitted on 16 Jan 2019

HAL is a multi-disciplinary open access archive for the deposit and dissemination of scientific research documents, whether they are published or not. The documents may come from teaching and research institutions in France or abroad, or from public or private research centers.

L'archive ouverte pluridisciplinaire **HAL**, est destinée au dépôt et à la diffusion de documents scientifiques de niveau recherche, publiés ou non, émanant des établissements d'enseignement et de recherche français ou étrangers, des laboratoires publics ou privés.

Nanoparticules lipidiques multicompartmentées de type *Janus* à compartiment superparamagnétique : du procédé de mise en œuvre aux applications théranostiques

Thèse de doctorat de l'Université Paris-Saclay
Préparée à l'Université Paris-Sud

École doctorale n°569 : Innovation thérapeutique : du fondamental à
l'appliqué (ITFA)
Spécialité de doctorat : Pharmacotechnie et Biopharmacie

Thèse présentée et soutenue à Châtenay-Malabry, le 15 décembre 2017, par

Elodie MILLART

Composition du Jury :

Véronique ROSILIO Professeure, Université Paris-Sud (– Institut Galien Paris-Sud)	Président
Abdelhamid ELAISSARI Directeur de recherche, Université Lyon 1 (– LAGEP)	Rapporteur
Annabelle GEZE Maître de conférences, HDR, Université Grenoble Alpes (– DPM UMR 5063)	Rapporteur
Sylviane LESIEUR Directrice de recherche, Université Paris-Sud (– Institut Galien Paris-Sud)	Examineur
Christine MENAGER Professeure, Université Pierre et Marie Curie (– PHENIX)	Examineur
Vincent FAIVRE Maître de conférences, HDR, Université Paris-Sud (– Institut Galien Paris-Sud)	Directeur de thèse

A mon père,

Remerciements

Je souhaiterais remercier le directeur de l'Institut Galien, le Professeur Elias FATTAL, de m'avoir donné l'opportunité d'effectuer mon travail de thèse au sein de son unité.

Je voudrais remercier la responsable de l'équipe 2, le Docteur Sylviane LESIEUR, pour ses conseils lors des discussions scientifiques et pour avoir accepté d'être examinateur de cette thèse.

J'aimerais remercier la responsable de l'équipe PHENIX, le Professeur Christine MENAGER pour son encadrement, ses conseils, sa disponibilité et son accueil chaleureux lors de mes nombreuses visites à l'UPMC et pour avoir accepté d'être examinateur de cette thèse.

Je souhaiterais remercier Monsieur Abdelhamid ELAISSARI et Madame Annabelle GEZE, d'avoir accepté d'être rapporteurs de cette thèse ainsi que Madame Véronique ROSILIO d'avoir accepté la responsabilité de présidente du jury.

Je voudrais remercier tous les membres permanents de l'équipe 2, Madame Angelina ANGELOVA, Madame Gillian BARRATT, Madame Claudie BOURGAUX, Monsieur David CHAPRON, Monsieur François-Xavier LEGRAND et Monsieur Jean-Jacques VACHON pour leur aide et leurs conseils tout au long de ces 3 années de thèse.

J'aimerais aussi remercier tous les non-permanents, Caroline, Maëlle, Franck, Paul, Maïwenn, et Eloïsa pour avoir égayé le quotidien du laboratoire.

Je souhaiterais remercier la technicienne chimiste du laboratoire PHENIX, Madame Aude MICHEL TOURGIS de m'avoir initié et formé à toute la technologie des ferrofluides mais également pour son accueil, sa bonne humeur et son soutien lors de mes visites à l'UPMC.

Je voudrais remercier tous mes collègues thésards pour qui l'aventure se termine aussi : Shibin, since your arrival in France until the defense, we have shared all the stages of the PhD, the experiments, the congresses, the submissions of articles and finally the defense. Rania, je ne pensais pas avoir l'opportunité de me faire une amie en venant ponctuellement à l'UPMC mais tu m'as prouvée le contraire. Jimmy, mon meilleur ami, le plus fidèle parmi les fidèles, un paragraphe entier ne suffirait pas à t'exprimer toute ma gratitude. Tu as été là à chaque instant, les bons et surtout les moins bons et sans toi, il n'y aurait pas de manuscrit.

Je souhaiterais également remercier Jérémy, le grand sage, pour son écoute, son soutien et ses conseils qui m'accompagnent depuis quelques années déjà.

Enfin, à la personne sans qui je ne serais pas là aujourd'hui, ma maman. Merci pour tout. Merci d'être là. Merci d'être toi.

Summary

In recent years, our team has developed original compartmented lipid nanometer-sized particles produced by high pressure homogenization, a scalable process, with pharmaceutically approved excipients.

The particles actually belong to the family of *Janus* nano-objects as they are organized in two juxtaposed substructures : one half is a droplet of liquid-state lipids while the other half is vesicle-like and encloses an aqueous core delimited by a phospholipid-containing bilayer shell.

Added to the intrinsic biocompatibility of the constituting lipids, such a system provides a potentially very valuable tool in pharmaceutical and biomedical fields, able to separately incorporate and co-convey hydrophilic and lipophilic substances with distinct activities, for example, a medical imaging agent and a drug for coupling diagnosis and therapy.

Here, we are interested in loading *Janus* nanoparticles with a magnetic fluid composed of superparamagnetic iron oxide nanocrystals (ferrofluid, FF), indeed as efficient contrast agent for magnetic resonance imaging (MRI), being magnetically targetable and providing ability for hyperthermia treatment.

Alternately, hydrophilic or lipophilic FF compatible with the production process have been developed by investigating different stabilization pathways of the nanocrystals depending on the encapsulation compartment.

Résumé

Depuis quelques années, notre laboratoire développe des nanoparticules lipidiques bicompartimentées originales produites par homogénéisation haute pression, un procédé transposable à grande échelle, à partir d'excipients pharmaceutiques validés par différentes pharmacopées (Eur., USP, JP).

Ces particules appartiennent ainsi à la famille des nano-objets *Janus* puisqu'elles sont organisées en deux sous-structures juxtaposées : une moitié est constituée d'une gouttelette huileuse alors que l'autre moitié est composée d'une structure vésiculaire et renferme un cœur aqueux délimité par une bicouche phospholipidique.

En plus de la biocompatibilité intrinsèque des lipides constituants, un tel système représente un outil potentiellement très intéressant et valorisable du point de vue pharmaceutique et biomédical capable d'incorporer séparément et de co-véhiculer des substances hydrophiles et lipophiles aux activités distinctes, par exemple un agent d'imagerie médical et un principe actif pour coupler diagnostique et thérapie.

Ici, nous nous sommes intéressés à charger les nanoparticules *Janus* avec un fluide magnétique composé de nanocristaux d'oxyde de fer (ferrofluide, FF), actif en tant qu'agent de contraste efficace en IRM, étant magnétiquement contrôlable et permettant d'envisager un traitement par hyperthermie.

Tour à tour, des FF hydrophiles ou lipophiles compatibles avec le procédé de production ont été développés en étudiant différentes voies de stabilisation des nanocristaux en fonction du compartiment d'encapsulation.

Table of contents

Remerciements	3
Summary	5
Résumé	6
List of figures	12
List of tables	17
List of abbreviations	19
GENERAL INTRODUCTION.....	23
BIBLIOGRAPHIC PART	30
SUPERPARAMAGNETIC LIPID-BASED HYBRID NANOSYSTEMS FOR DRUG DELIVERY	31
1. Introduction	33
2. Superparamagnetic Iron Oxide Nanoparticles (SPION)	33
2.1. Structure and magnetic properties	33
2.2. Biocompatibility – biodegradability.....	34
2.3. Applications (MRI, magnetophoric mobility, hyperthermia)	35
3. Magnetic-fluid-loaded lipid-based nanoscale systems	43
3.1. Systems based on lyotropic lipids.....	43
3.1.1. Synthetic vesicles : liposomes	43
3.1.1.1. Magnetic guidance.....	43
3.1.1.2. Hyperthermia	46
3.1.2. Natural vesicles : microvesicles and exosomes.....	49
3.1.3. Compartmented nanoparticles	50
3.2. Systems based on non-polar lipids.....	53
3.2.1. Nanoemulsions.....	53
3.2.2. Solid lipid nanoparticles	56
4. Conclusion	58

5. Expert opinion : a focus on co-encapsulation	59
References	64
EXPERIMENTAL PART	78
CHAPTER 1	
SCALABLE PROCESS TO PRODUCE LIPID-BASED INNOVATIVE COMPARTMENTED JANUS NANOPARTICLES WITH PHARMACEUTICALLY APPROVED EXCIPIENTS	79
1. Introduction	81
2. Materials and Methods.....	82
2.1. Materials	82
2.2. Methods.....	82
2.2.1. Preparation of nanodispersions by high-pressure homogenization process.....	82
2.2.2. Particle size and zeta potential measurements	83
2.2.3. X-ray diffraction (XRD)	84
2.2.4. Cryogenic transmission electron microscopy (Cryo-TEM)	84
2.2.5. Optical microscopy	84
3. Results and Discussions.....	85
4. Conclusion	95
Author contributions	96
References	97
CHAPTER 2	
INCORPORATION OF HYDROPHILIC FERRO-FLUIDS INTO LIPID-BASED JANUS NANOPARTICLES	100
1. Introduction	102
2. Materials and Methods.....	102
2.1. Materials	102
2.2. Methods.....	103
2.2.1. Maghemite nanoparticles synthesis.....	103
2.2.2. Maghemite nanoparticles coating.....	103

2.2.3. Particle size	106
2.2.4. Thermogravimetric (TGA) analysis	106
2.2.5. X-ray diffraction (XRD)	106
2.2.6. Small-angles X-ray scatterings (SAXS)	107
2.2.7. Infra-red (IR) spectroscopy	108
2.2.8. Preparation of magnetic nanodispersions by high-pressure homogenization process.....	108
2.2.9. Transmission electron microscopy (TEM)	108
2.2.10. Cryogenic transmission electron microscopy (Cryo-TEM)	108
2.2.11. Optical microscopy	109
3. Results and Discussions.....	109
3.1. FF particle size	109
3.2. FF selection strategy : FF vs. Process compatibility	110
3.3. Characterization of FF-PAA and FF-PAAMA	111
3.3.1. Structural organization.....	111
3.3.2. FTIR.....	114
3.3.3. TGA	117
3.4. Incorporation trials in Janus nanoparticles.....	119
3.5. Aqueous FF influency on the formation mechanism.....	120
3.5.1. SAXS experiments	120
3.5.2. Optical microscopy	123
4. Conclusion	126
References	127

CHAPTER 3

INCORPORATION OF HYDROPHOBIC FERRO-FLUIDS INTO LIPID-BASED JANUS NANOPARTICLES..... 131

1. Introduction	133
2. Materials and Methods.....	134
2.1. Materials	134
2.2. Methods.....	134
2.2.1. Maghemite nanoparticles synthesis.....	134

2.2.2. Maghemite nanoparticles coating.....	134
2.2.3. Infra-red (IR) spectroscopy	136
2.2.4. SAXS ALBA	136
2.2.5. Preparation of magnetic nanodispersions by high-pressure homogenization process.....	137
2.2.6. Purification step.....	137
2.2.7. Iron assay	137
2.2.8. Drug loading (DL) and entrapment efficiency (EE).....	138
2.2.9. Particle size	138
2.2.10. Cryogenic transmission electron microscopy (Cryo-TEM)	138
2.2.11. Magnetic measurement	139
2.2.12. Relaxometry.....	139
2.2.13. Magnetic accumulation : preliminary test	139
3. Results and Discussion	139
3.1. Characterizations.....	139
3.1.1. FT-IR	139
3.1.1.1. Oleic acid	139
3.1.1.2. BNE	141
3.1.2. FF-Labrafils interactions : SAXS analysis	143
3.2. Incorporation trials in Janus nanoparticles.....	148
3.3. Magnetization	150
3.4. Relaxometry	153
3.5. Accumulation.....	156
4. Conclusion	157
References	158
GENERAL DISCUSSIONS	162
GENERAL CONCLUSIONS AND PERSPECTIVES.....	171

ANNEX	174
1. Lipids.....	175
2. Surfactants	176
2.1. Gelucire® 50/13	176
2.2. Phospholipon® 90G	176

List of figures

Figure 1.1. A : Cryo-TEM micrographs of EPC:DSPE-PEG2000 (95:5 mol %) MFL with 1.8 mol of ferrofluid loaded per mol of lipids. Total lipid concentration is equal to 1 mM [55]. B : Total association of RU-MFLs with MCF-7 cells at 37 °C (400 nmol of total lipids and 600 nmol of Fe(III) per 106 cells; [lipids] = 0.4×10^{-3} M; [Fe(III)] = 0.6×10^{-3} M) as a function of incubation period of time and in the presence or absence of a 0.44 T magnet; lipids (a) and iron mass mFe(III) (b) uptakes from rhodamine-fluorescence counting [58]. With permissions. .. 45

Figure 1.2. Release of 5-FU entrapped from magnetoliposomes as a function of the incubation time in PBS (pH = 7.4 ± 0.1) in the absence (■, $37.0 \pm 0.5^\circ\text{C}$), or under the influence (□, $45.0 \pm 1.0^\circ\text{C}$) of a high frequency alternating electromagnetic field gradient [67]. With permission. 48

Figure 1.3. (A) Growth evaluation of hepatoma 22 subcutaneous cancer in Kunming mice after sample administration. Tumor volume was examined every 3 days for 12 consecutive days ; (B) Hepatoma 22 tumor tissues obtained from euthanized mice 12 days after sample administration [77]. 50

Figure 1.4. Cryo-TEM images of mesophase nanoparticles loaded with 8-nm spherical OA-SPION at 0.3 wt% Fe concentration in phytantriol. SPION ordering within the inner bicontinuous cubic structure of the nanoparticles can be seen [84]. With permission. 52

Figure 1.5. Magnetite and poly(N-isopropylacrylamide) were incorporated in monoolein and oleic acid cubosomes. Magnetite generates heat under an alternative current magnetic field, HmPNIPAM in the water channel of the cubosome becomes water-insoluble and assumes a contracted form when the temperature increases above the phase transition temperature. Accordingly, the thermo-sensitive polymer will act as a thermal valve in the water channels of the cubosomes [87]. 53

Figure 1.6. A : Negative stain transmission electron microscopy (TEM) images of the different nanoemulsion formulations [108]. B : Starting at day 6, tumor growth profiles of the PAV

nanoemulsion treated groups compared to saline, control nanoemulsions, FeO nanoemulsions, and free PAV injected groups [109]. With permissions.....	55
Figure 1.7. A : TEM image of non purified IBMSLN; B : cumulative release curve of ibuprofen (IB) from IBMSLN [122]. With permission.	57
Figure 2.1. Summary of the formulation studies depending on the proportion of stabilizers and the lipid phase composition. Filled symbol: successful formulations; open symbol: unsuccessful formulations. Successful attributes have been defined as mean diameter comprised between 100 and 200 nm and stable during at least three months. The concentration of the lipid phase was 20% of the total suspension (w/w).	86
Figure 2.2. Cryo-TEM view of nanodispersions containing (a) linoleoyl polyoxylglycerides / stearoyl macroglycerides / soybean lecithin, (b) caprylic-capric triglycerides / stearoyl macroglycerides / soybean lecithin, (c) oleoyl polyoxylglycerides / stearoyl macroglycerides / soybean lecithin and (d) linoleoyl polyoxylglycerides / stearoyl macroglycerides. (e) schematic views of Janus nanoparticles depending on their orientation.	87
Figure 2.3. SAXS profile at 20 °C of the nanodispersions containing linoleoyl polyoxylglycerides. Inset: log-log representation. Results acquired after 8 days of storage at 20 °C.....	88
Figure 2.4. Long-time size stability of the nanoparticles prepared with 3% of the stearoyl macroglycerides – soybean lecithin (2:1) mixture. (a) mean size \pm SD (nm) and PDI \pm SD; (b) zeta potential \pm SD; n = 3 (three different batches).....	89
Figure 2.5. Janus nanoparticles deformations on concentrated cryo-TEM grid.	90
Figure 2.6. Cryo-TEM view of 1 kg batch of Janus nanoparticles produced by high-pressure homogenization.	91
Figure 2.7. Follow-up of a linoleoyl polyoxylglycerides / water (1:1) mixture during its cooling from 60°C to 25°C and its heating to 60°C. (a) Optical microscopy pictures showing water droplets into linoleoyl polyoxylglycerides. At 25°C, arrows point out phase separation. (b)	

Focus on myelin figures and phase separation at 3 temperatures (47°C, 40°C and 35°C). (c) Mean diameter of a water droplet during its cooling and heating.....	93
Figure 2.8. SAXS patterns with temperature of (a) linoleoyl polyoxylglycerides / water (9:1) between 20°C to 60°C (heating rate: 2°C/min) and (b) pure linoleoyl polyoxylglycerides at 20°C and 60°C.....	94
Figure 3.1. Sodium citrate	104
Figure 3.2. Sodium carboxymethyl dextran	104
Figure 3.3. Sodium polyacrylate	105
Figure 3.4. Poly(acrylic acid-co-maleic acid)	105
Figure 3.5. QELS profiles of FF-PAA before (left) and after (right) HPH process.....	110
Figure 3.6. Nanodispersions obtained after HPH process with FF-cit (left), FF-CMD (middle) and FF-PAA or FF-PAAMA (right).....	111
Figure 3.7. TEM views of FF-PAA (left) and FF-PAAMA (right).	111
Figure 3.8. XRD pattern of FF-PAAMA.	112
Figure 3.9. FTIR analysis of the acidic FF (red), the PAAMA polymer (blue) and the FF-PAAMA (purple).....	115
Figure 3.10. FTIR analysis of the acidic FF (red), the PAA polymer (orange) and the FF-PAA (green).	117
Figure 3.11. TGA analysis of the acidic FF (red), the FF-PAAMA (purple) and the FF-PAA (blue).	119
Figure 3.12. Cryo-TEM view of Janus nanoparticles.	120
Figure 3.13. SAXS experiments on Labrafil® M2125 CS mixed with water (blue), FF-PAAMA (black) or FF-PAA (red).....	121

Figure 3.14. Evolution of the lamellar phase thickness as a function of the FF-PAAMA (black) or FF-PAA (red) concentration. 122

Figure 3.15. SAXS experiments on mixtures of Labrafil® M2125 CS and FF-PAA at 3% in a ratio 9/1 respectively under different temperatures, ▫ intensity of the diffraction peak, ▫ position of the diffraction peak. 122

Figure 3.16. Optical microscopy pictures showing aqueous FF droplets into Labrafil® during cooling from 57°C to 14°C..... 124

Figure 3.17 : Focus on myelin figures at 24°C. 125

Figure 3.18. Optical microscopy pictures showing aqueous FF droplets into Labrafil® during heating from 14°C to 50°C..... 125

Figure 4.1. Oleic acid. 135

Figure 4.2. Phosphoric diester like anionic surfactant. 135

Figure 4.3. FTIR analysis of the acidic FF (red), the oleic acid (green) and the FF-OA (orange). 140

Figure 4.4. FTIR analysis of the acidic FF (red), the BNE (blue) and the FF-BNE (purple). 142

Figure 4.5. SAXS analysis of Labrafil® M1944 CS/FF-AO (black), Labrafil® M1944 CS/FF-BNE (red), Labrafil® M2125 CS/FF-AO (green) and Labrafil® M2125 CS/FF-BNE (blue) mixing..... 143

Figure 4.6. Guinier analysis of Labrafil® M1944 CS/FF-OA (black), Labrafil® M1944 CS/FF-BNE (red), Labrafil® M2125 CS/FF-OA (green) and Labrafil® M2125 CS/FF-BNE (blue) mixing..... 144

Figure 4.7. Evaluation of the particle distance distribution function $p(r)$ (extraction from the GNOM software interface)..... 145

Figure 4.8. SAXS experiments on Labrafil® M2125 CS mixed with water (black), FF-BNE and water (green) or FF-OA and water (red). 146

Figure 4.9. SAXS experiments on Labrafil® M1944 CS mixed with water (black), FF-BNE and water (green) or FF-OA and water (red). 147

Figure 4.10. Evolution of the size of the nanodispersions with the time. Purified FF-2125-JNP in blue, purified FF-1944-JNP in red. 149

Figure 4.11. Cryo-TEM view of Janus nanoparticles. 150

Figure 4.12. Magnetization of the studied nanodispersions versus magnetic field. A) FF-BNE-2125, B) FF-BNE-1944, C) purified FF-2125-JNP and D) purified FF-1944-JNP. 153

Figure 4.13. Dispersed Janus nanoparticles (A) and accumulated ones (B) after exposure to a magnet. 157

List of tables

Table 1.1. Main characteristics of the systems based on lyotropic lipids. Data in italic have been calculated / estimated from the data available in the corresponding publications.	38
Table 1.2. Main characteristics of the systems based on non-polar lipids. Data in italic have been calculated / estimated from the data available in the corresponding publications.....	40
Table 1.3. Summary of the in vivo biological evaluations made with the systems described in this review. Data in italic have been calculated / estimated from the data available in the corresponding publications.	41
Table 3.1. Size and PDI of the FF-cit and the synthesized acidic FF, FF-CMD, FF-PAA and FF-PAAMA.	110
Table 3.2. Indexation and peak position of the FF-PAAMA and FF-PAA diffractograms. Comparison with Fe ₂ O ₃ and Fe ₃ O ₄ references. The peak intensities are classified as weak (w), strong (s) and very strong (vs). * Unfortunately unexpected noise of the sample had disturbed the determination of this reflection position.....	113
Table 3.3. Summary of the different diameters of the FF-PAAMA and FF-PAA grains.....	113
Table 3.3. IR band positions and assignments for acidic FF, PAAMA polymer and FF-PAAMA.	115
Table 3.4. IR band positions and assignments for acidic FF, PAA polymer and FF-PAA....	116
Table 3.4. Evolution of the temperature of disappearance of the lamellar phase peak in function of the iron concentration.....	123
Table 4.1. IR band positions and assignments for acidic FF, OA and FF-OA. The area between 2000 and 2500 cm ⁻¹ represents the absorbance of the diamond used.	141

Table 4.2. IR band positions and assignments for acidic FF, BNE and FF-BNE. The area between 2000 and 2500 cm^{-1} represents the absorbance of the diamond used.	142
Table 4.3. Comparison on the radius of gyration between Guinier analysis and P(r) function analysis.	145
Table 4.4. Evolution of the thickness of the hydrated Labrafil® M2125 CS lamellar phase depending on the presence and type of hydrophobic FF.	146
Table 4.5. Evolution of the thickness of the hydrated Labrafil® M1944 CS lamellar phase depending on the presence and type of hydrophobic FF.	147
Table 4.6. Iron concentration, SPION loading and encapsulation efficiency in purified formulations.	150
Table 4.7. Relaxivities r_1 and r_2 and r_2/r_1 ratio of purified FF-2125-JNP and FF-1944-JNP.	154

List of abbreviations

°C	Degree Celsius
μm	Micrometer
Å	Angstrom
AMF	Alternative magnetic field
API	Active pharmaceutical ingredients
ATR	Attenuated total reflectance
BNE	BeycoStat N B09
cm	Centimeter
CCD	Charge Coupled Device
CB:ZnPc	Cucurbit-7-uril zinc phthalocyanine complex
CMD	Carboxymethyl Dextran
Cryo-TEM	Cryogenic transmission electron microscopy
DDS	Drug delivery system
DL	Drug loading
DLS	Dynamic light scattering
DML	Docetaxel-embedded cationic magnetoliposomes
dMLs	Doxorubicin-embedded magnetoliposomes
DMPG	1,2-dimyristoyl- <i>sn</i> -glycero-3-phosphorylglycerol
DOPC	1,2-dioleoyl- <i>sn</i> -glycero-3-phosphocholine
DOPE	1,2-dioleoyl- <i>sn</i> -glycero-3-phosphoethanolamine
DOPG	1,2-dioleoyl- <i>sn</i> -glycero-3-phospho-(1'- <i>rac</i> -glycerol)
DOX	Doxorubicin
DPPC	Dipalmitoylphosphatidylcholine
DPTAP	1,2-dipalmitoyl-3-trimethylammonium propane
DSPC	1,2-distearoyl- <i>sn</i> -glycero-3-phosphocholine
DSPE-PEG2000	1,2-diacyl- <i>sn</i> -glycero-3-phosphoethanolamine- <i>N</i> -[methoxy (poly (ethylene glycol))-2000]
D-SMNC-EXOs	Doxorubicin-loaded reticulocytes exosome-based superparamagnetic nanoparticle cluster
e.g.	For example
EE	Entrapment efficiency

ELR	Echo-limiting regime
EPC	Egg-yolk L- α -phosphatidylcholine
EPR	Enhanced permeability and retention
F-68	Poloxamer 188
FF-1944-JNP	Labrafil® M1944 CS-based <i>Janus</i> nanoparticles loaded with Beycostat N B09-coated maghemite
FF-2125-JNP	Labrafil® M2125 CS-based <i>Janus</i> nanoparticles loaded with Beycostat N B09-coated maghemite
FF-BNE	Beycostat N B09-coated maghemite
FF-cit	Citrate coated-maghemite
FF-CMD	Carboxymethyl dextran-coated maghemite
FF-OA	Oleic acid-coated maghemite
FF-PAA	Poly(acrylic acid)-coated maghemite
FF-PAAMA	Poly(acrylic acid-co-maleic acid)-coated maghemite
FDA	Food and Drug Administration
FCD	Fixed-dose combination
FF	Ferrofluid
Fol	Folate
FTIR	Fourier-transform infrared spectroscopy
FTML	Folate-targeted cationic magnetoliposomes
5-FU	5-fluorouracil
g	Gram
GML	Gemcitabine-containing magnetoliposomes
GMS	Glycerol monostearate
GRAS	Generally recognized as safe
h	Hour
HCPT	10-hydroxycamptothecin
HLB	Hydrophilic-lipophilic balance
HPH	High pressure homogenization
HSPC	Hydrogenated soybean lecithin
IBMSLN	Ibuprofen-loaded magnetic solid lipid nanoparticles
ICP-AES	Inductively coupled plasma atomic emission spectroscopy
ICP-MS	Inductively coupled plasma mass spectrometry
IM	Intramuscular
IR	Infrared

IV	Intravenous
JNP	<i>Janus</i> nanoparticles
kg	Kilogram
MAR	Motional average regime
MTX	Methotrexate
MFL	Magnetic-fluid-loaded liposomes
mg	Milligram
min	Minute
mL	Milliliter
ML	Magnetoliposomes
mm	Millimeter
MRI	Magnetic resonance imaging
M-Tfs	Magnetic transferrins
MTT	Methylthiazol tetrazolium
NBD-DPPE	1,2-dipalmitoyl-sn-glycero-3-phosphoethanolamine-N-(7-nitro-2-1,3-benzoxadiazol-4-yl)
NE	Nanoemulsions
NH ₃	Ammonia
NLC	Nanostructured lipid carriers
NMRD	Nuclear magnetic resonance dispersion
nm	Nanometer
OA	Oleic acid
OML	Oxaliplatin-containing magnetoliposomes
o/w	Oil in water
PAA	Poly(acrylic acid)
PAAMA	Poly(acrylic acid-co-maleic acid)
PAV	Prednisolone valerate acetate
PBS	Phosphate buffered saline
PC	Phosphatidylcholine
PdI	Polydispersity index
PEG	Polyethylene glycol
PEG750-DMPE	1,2-dimyristoyl-sn-glycero-3-phosphoethanolamine-N-[methoxy(polyethylene glycol)-750]
PRM	Partial refocusing regime
PVA	Poly(vinyl alcohol)

PVP	Poly(vinyl pyrrolidone)
QELS	<i>Quasi</i> -elastic light scattering
R _g	Radius of gyration
rpm	Round per minute
RT	Room temperature
SAR	Specific absorption rate
SAXS	Small-angle X-ray scattering
SC	Subcutaneous
SD	Standard deviation
SDR	Static dephasing regime
SLN	Solid lipid nanoparticles
SLP	Specific loss power
SMNC-EXOs	Reticulocytes exosome-based superparamagnetic nanoparticle cluster
SPION	Superparamagnetic iron oxide nanoparticles
SpL	SPION loading
SQUID	Superconducting quantum interference device
TEM	Transmission electron microscopy
Tf	Transferrin
TGA	Thermogravimetric analysis
TPCS2a	disulfonated tetraphenylchlorin
TMAG	Didodecyl <i>N</i> -(α -(trimethylammonio) acetyl)- <i>D</i> -glutamate chloride
t-PA	Tissue-plasminogen activator
v/v	Volume per volume
VSM	Vibrating sample magnetometer
w/w	Weight per weight
WAXS	Wide-angle X-ray scattering
XRD	X-ray Diffraction

GENERAL INTRODUCTION

Medicine relies on the use of pharmacologically active agents (therapeutics or drugs) to manage or reverse the course of disease. However, pharmacologically active agents are not inherently effective ; their benefit is directly coupled to the manner by which they are administered. There is a need to improve modes of delivery, and a clearer scientific understanding of how drug administration affects safety and efficacy, as new therapeutic molecules are discovered.

Before 1950, all drugs were made into pill or capsule formulations that released the loaded drug immediately in contact with water without any ability to control the drug release kinetics. The first controlled release formulation was introduced by Smith Kline & French in 1952 for 12-hour delivery of dextroamphetamine (Dexedrine) [1]. Then, bioadhesive forms, that increased the residence time in front of absorption windows (skin, mucosa), and microparticulate dosage forms, implantable or smoothing intestinal distribution in case of oral administration, have been developed. At last, nanosized forms were investigated in order to control drug distribution after intravenous administration. Since the first FDA approval of colloidal drug delivery system (DDS), amphotericin B-loaded liposomes in 1990, more than ten DDS based on nanotechnology are now commercially available to treat diverse diseases ranging from cancer to fungal infection and to muscular degeneration [2,3].

The use of nanoparticulate pharmaceutical DDS can overcome several problems that are associated with traditional drugs, such as poor aqueous solubility, low bioavailability and nonspecific distribution in the body. The first generation of nanoparticulate DDS mainly aimed to improve one single aspect, such as the need to increase drug stability *in vivo* and the circulation time in the blood, or the need to target a drug to a specific tissue or pathology. Now, research has led to the development of nanoparticles that can perform two or more functions (either simultaneously or sequentially) to overcome multiple physiological barriers to optimize delivery and distribute their loads (single or multiple) to the required target sites (organs, tissues, cells) or specific pathologies in the body [4].

Multifunctional nanoparticles fabricated using various chemistries with distinctive architectures have been designed and evaluated for potential drug delivery applications [5,6]. In general, nanoparticles can be classified as organic and inorganic.

In organic-based nanomaterials, polymeric nanoparticles, micelles, and liposomes mostly consist of amphiphilic compounds with biocompatibility, while crosslinked nanogels provide a network with highly porous structure, and dendrimers have tree-like branched structures [7–11]. Polymers provide an interesting flexibility in terms of chemistry and structure for

fabricating multifunctional nanoparticles. Organic or polymeric nanoparticles have been widely used in designing DDS and have shown awesome promise in biomedical applications [12–15].

Inorganic nanocarriers such as mesoporous silica, magnetic nanoparticles, gold nanoparticles, and quantum dots have unique properties and provide capabilities for tracking, while their rigid surfaces are suitable to functionalization [16]. They possess a number of characteristics that make them convenient for drug delivery, including robust and durable core materials allowing secure encapsulation of cargo, wide range of functions, and abundantly available materials to reduce cost [17,18]. Moreover, inorganic nanocarriers can also exhibit different imaging modalities, magnetic properties, and photothermal capacities that are not usually seen in lipid and polymer-based nanoparticles. Thus, multifunctional magnetic nanoparticles, mesoporous silica nanoparticles, quantum dots, gold nanoparticles, and carbon nanotubes have been used as DDS [19–23].

In addition to conventional drug-encapsulated nanoparticles, *Janus* particles have an interesting anisotropic structure which makes them very attractive since they can be used to co-deliver two drugs with distinct properties or a drug and an imaging agent [24]. As a demonstration, water soluble (doxorubicin hydrochloride) and water insoluble (paclitaxel) drugs are encapsulated in a single *Janus* particle. Each drug is separately released from the particles [25].

In this PhD thesis, superparamagnetic iron oxide nanoparticles (SPION) are chosen as a diagnostic agent, and incorporated into innovative lipid-based *Janus* nanoparticles to produce a new theranostic tool. Two different ways of stabilization of the SPION were investigated and their further encapsulation in *Janus* nanoparticles.

The thesis consists of four main sections. In the first section, a literature review inventories and describes the recent lipid-based nanosystems encapsulating SPION and their applications in drug delivery. To achieve the different specific aims, the research plan is divided in three chapters.

Chapter 1 : Scalable process to produce lipid-based innovative compartmented *Janus* nanoparticles with pharmaceutically approved excipients. This chapter reports the formation mechanism of the *Janus* nanoparticles and their different physico-chemical characterizations.

Chapter 2 : Synthesis and incorporation of aqueous ferrofluid in *Janus* nanoparticles. In this section, an aqueously stabilized ferrofluid is developed and characterized in order to be incorporated in the aqueous part of the *Janus* nanoparticles.

Chapter 3 : Synthesis and incorporation of lipophilic ferrofluid in *Janus* nanoparticles. In this last part, a hydrophobic ferrofluid is prepared and characterized with the intention of being incorporated in the lipid part of the *Janus* nanoparticles.

At last, general discussion and conclusion will end this manuscript. An annex describing the lipid-based raw materials used in this project has been added to help the reader.

References

- [1] Helfand WH, Cowen DL. Evolution of pharmaceutical oral dosage forms. *Pharm. Hist.* 1983;25:3–18.
- [2] Allen TM. Drug Delivery Systems: Entering the Mainstream. *Science.* 2004;303:1818–1822.
- [3] Adler-Moore J. AmBisome targeting to fungal infections. *Bone Marrow Transplant.* 1994;14 Suppl 5:S3-7.
- [4] Ferrari M. Cancer nanotechnology: opportunities and challenges. *Nat. Rev. Cancer.* 2005;5:161–171.
- [5] Levy L, Sahoo Y, Kim K-S, et al. Nanochemistry: synthesis and characterization of multifunctional nanoclinics for biological applications. *Chem. Mater.* 2002;14:3715–3721.
- [6] Martinez JO, Brown BS, Quattrocchi N, et al. Multifunctional to multistage delivery systems: The evolution of nanoparticles for biomedical applications. *Chin. Sci. Bull.* 2012;57:3961–3971.
- [7] Bi R, Shao W, Wang Q, et al. Spray-freeze-dried dry powder inhalation of insulin-loaded liposomes for enhanced pulmonary delivery. *J. Drug Target.* 2008;16:639–648.
- [8] Oh JK, Drumright R, Siegwart DJ, et al. The development of microgels/nanogels for drug delivery applications. *Prog. Polym. Sci.* 2008;33:448–477.
- [9] Otsuka H, Nagasaki Y, Kataoka K. PEGylated nanoparticles for biological and pharmaceutical applications. *Adv. Drug Deliv. Rev.* 2003;55:403–419.
- [10] Gaucher G, Dufresne M-H, Sant VP, et al. Block copolymer micelles: preparation, characterization and application in drug delivery. *J. Controlled Release.* 2005;109:169–188.
- [11] Cho K, Wang X, Nie S, et al. Therapeutic Nanoparticles for Drug Delivery in Cancer. *Clin. Cancer Res.* 2008;14:1310–1316.

- [12] Elsabahy M, Wooley KL. Design of polymeric nanoparticles for biomedical delivery applications. *Chem. Soc. Rev.* 2012;41:2545.
- [13] Khemtong C, Kessinger CW, Gao J. Polymeric nanomedicine for cancer MR imaging and drug delivery. *Chem. Commun.* 2009;3497.
- [14] Kulkarni A, DeFrees K, Schuldt RA, et al. Multi-armed cationic cyclodextrin:poly(ethylene glycol) polyrotaxanes as efficient gene silencing vectors. *Integr Biol.* 2013;5:115–121.
- [15] Loethen S, Ooya T, Choi HS, et al. Synthesis, Characterization, and pH-Triggered Dethreading of α -Cyclodextrin-Poly(ethylene glycol) Polyrotaxanes Bearing Cleavable Endcaps. *Biomacromolecules.* 2006;7:2501–2506.
- [16] Subbiah R, Veerapandian M, S. Yun K. Nanoparticles: Functionalization and Multifunctional Applications in Biomedical Sciences. *Curr. Med. Chem.* 2010;17:4559–4577.
- [17] Liong M, Lu J, Kovoichich M, et al. Multifunctional Inorganic Nanoparticles for Imaging, Targeting, and Drug Delivery. *ACS Nano.* 2008;2:889–896.
- [18] Mai WX, Meng H. Mesoporous silica nanoparticles: A multifunctional nano therapeutic system. *Integr. Biol.* 2012;5:19–28.
- [19] Madani SY, Naderi N, Dissanayake O, et al. A new era of cancer treatment: carbon nanotubes as drug delivery tools. *Int. J. Nanomedicine.* 2011;6:2963–2979.
- [20] Day ES, Morton JG, West JL. Nanoparticles for Thermal Cancer Therapy. *J. Biomech. Eng.* 2009;131:074001-074001-5.
- [21] Qi L, Gao X. Emerging application of quantum dots for drug delivery and therapy. *Expert Opin. Drug Deliv.* 2008;5:263–267.
- [22] Gao J, Gu H, Xu B. Multifunctional Magnetic Nanoparticles: Design, Synthesis, and Biomedical Applications. *Acc. Chem. Res.* 2009;42:1097–1107.

- [23] Godin B, Chiappini C, Srinivasan S, et al. Discoidal Porous Silicon Particles: Fabrication and Biodistribution in Breast Cancer Bearing Mice. *Adv. Funct. Mater.* 2012;22:4225–4235.
- [24] Tran L-T-C, Lesieur S, Faivre V. Janus nanoparticles: materials, preparation and recent advances in drug delivery. *Expert Opin. Drug Deliv.* 2014;11:1061–1074.
- [25] Xie H, She Z-G, Wang S, et al. One-Step Fabrication of Polymeric Janus Nanoparticles for Drug Delivery. *Langmuir.* 2012;28:4459–4463.

BIBLIOGRAPHIC PART

REVIEW

SUPERPARAMAGNETIC LIPID-BASED HYBRID NANOSYSTEMS FOR DRUG DELIVERY

E. Millart¹, S. Lesieur¹, V. Faivre^{1,*}

¹ UMR CNRS 8612 Institut Galien Paris-Sud, Univ. Paris-Sud, Université Paris-Saclay,
5 rue Jean-Baptiste Clément, 92296 Châtenay-Malabry, France.

* Corresponding author

33.1.46835465

vincent.faivre@u-psud.fr

Revised version submitted to *Expert Opinion on Drug Delivery* on July 24th, 2017

Abstract

Introduction

The development of multifunctional drug carriers opens many opportunities in the field of drug delivery. Among them, carriers loaded with drug and superparamagnetic iron oxide nanoparticles allow the combination of chemotherapy with the possibility to monitor or control the distribution in the body of the nanocarrier, the triggering of the drug release and/or the implementation of a synergistic hyperthermia treatment.

Areas covered

The present review covers biocompatible lipid-based nanotechnologies that have been employed to co-encapsulate drug and iron oxide. Depending on their physico-chemical properties, lipids are able to generate monophasic lipophilic nanodispersions or more complex constructs containing both lipidic and aqueous domains. This review describes the how and why of these nanoobjects.

Expert opinion

A focus has been done on the co-encapsulation aspects of these hybrid systems especially to discuss the possible heterogeneities in drug-to-iron oxide ratio and the difficulties that could be encountered in the construction of such biocompatible multifunctional drug carriers.

Keywords : cubosomes, iron oxide, ISAsomes, liposome, nanoemulsions, NLC, SLN, SPION.

1. Introduction

Superparamagnetic iron oxide nanoparticles (SPION) are iron oxide single-crystal (nanocrystal) which are often coated with inorganic or organic materials of varying chemical properties and primarily used as stabilizers of the colloidal state. The dispersion of SPION into a carrier fluid such as water or organic solvents gives colloidal suspension named ferrofluid. It has long been of scientific and technological challenge to synthesize these systems and control their size distribution and shape. Beside conventional reaction processes based on redox-assisted precipitation of iron salts [1], more recent strategies for obtaining calibrated iron oxide crystals in nanometer range have emerged for the last decade including solvothermal, biomineralization or surfactant-assisted routes [2,3]. In parallel, surface modification or functionalization through covalent or non-covalent binding of molecules or macromolecules have been extensively developed to modulate the solubility of the nanocrystals in different liquid phases while preserving a stable suspension state therein. The most significant example concerns biomedical applications for which stability in physiological fluids is essential. In this last respect, simple surface-coating of SPION has been intentionally replaced/completed by hierarchical formulations leading to their incorporation/encapsulation in protective reservoir systems, possibly functional, while preserving even enhancing their superparamagnetic behaviour. The advantage of this approach is to allow the combination of SPION properties with other actions such as therapeutic activity through the co-encapsulation of drugs. The present review focuses on the latter aspect when lipid-based nanotechnology has been employed.

2. Superparamagnetic Iron Oxide Nanoparticles (SPION)

2.1. Structure and magnetic properties

SPION used for biomedical applications often consist of two components, an iron oxide core and a hydrophilic or hydrophobic surface-coating. The iron oxide core is nanometric and can be composed of magnetite (Fe_3O_4) and/or maghemite ($\gamma\text{-Fe}_2\text{O}_3$) as a rule in the single-crystal state. Maghemite, the ferromagnetic cubic form of Fe(III) oxide, is closely related to the structure of inverse spinel Fe_3O_4 but differs from it by the presence of vacancies distributed on the cation sublattice [4]. The magnetic properties present in some ferromagnetic materials are the result of aligned unpaired electron spins. In a non-magnetized ferromagnetic material, magnetic moments of the magnetic domains (Weiss-domains) are aligned at short range, but at long range, magnetic moments of adjacent domains are anti-aligned. Superparamagnetism

occurs when the size of the crystals is smaller than ferromagnetic domains (0.03 to 0.05 μm) and so, they don't have any magnetic remanence, unlike ferromagnetic materials [5]. Each crystal is then considered to be a fully magnetized single magnetic monodomain, and can be considered to be a monomagnet which is a direct consequence of the spinel structure of the crystal, permitting strong magnetic coupling and consequently perfect alignment of the individual magnetic spins. The temperature at which a particle becomes superparamagnetic is called the blocking temperature (T_B) and defined as :

$$T_B = \frac{KV}{k_B \ln\left(\frac{\tau_m}{\tau_0}\right)} \quad (\text{Equation 1})$$

where K is the magnetic anisotropy constant, V is the volume of a nanoparticle, k_b is the Boltzmann constant, τ_m is the measurement time and τ_0 is a length of time, characteristic of the material, called the *attempt time* or *attempt period* [6]. When SPION are placed in an external magnetic field their moments align in the direction of the magnetic field. This ability to elicit substantial disturbances in the local magnetic field through large magnetic moments leads to a rapid dephasing of surrounding protons, generating a detectable change in the magnetic resonance signal. Thus, the imaging capability provided is not from the SPION intrinsically, but through their influence on longitudinal and transverse relaxation of the surrounding nuclei [7].

2.2. Biocompatibility – biodegradability

Before SPION can be used *in vivo*, biocompatibility is a crucial factor that must be studied. Usually, SPION have a good biocompatibility profile [8,9] and their uptake by macrophages is not associated with cell activation. The biocompatibility extent of SPION mainly depends on the nature of the magnetic content, final NP size and nature of coating. Human tissues may contain iron or iron oxides in the form of haemosiderin, ferritin and transferrin. Normal liver contains approximately 0.2 mg of iron per gram and total human iron stores amount to 3500 mg. The total amount of iron oxide for diagnostic imaging (50 to 200 mg Fe) is small compared to the body's normal iron store. Chronic iron toxicity develops only after the liver iron concentration exceeds 4 mg Fe/g [10]. The particle size affects cellular uptake, biodistribution, and other pharmacokinetics. Size of iron oxide nanoparticles should be optimized to avoid rapid clearance by the body's immune system, and consequently to be accumulated sufficiently in the target tissue or organ. The size ranges could differ depending on the shape, surface

composition and charge [11] but it was reported that very small-sized nanoparticles (hydrodynamic diameter of < 5-10 nm) are excreted renally [12] whereas medium-sized nanoparticles (30-150 nm) offer a broad distribution in the bone marrow, heart, kidney and stomach [13]. Meanwhile, large particles with hydrodynamic diameter of > 50-100 nm are easily taken up by phagocytes [14] and therefore tend to quickly accumulate in tissues such as the liver and spleen [15]. Interestingly, nanoparticles of 10-20 to 100-150 nm tend to accumulate in tumors through enhanced permeability and retention (EPR) effect, because cancerous tissues generally combines fenestration of blood vessels that are hundreds of nanometers in size [16,17] and a poor lymphatic drainage. In order to prolong plasma half-life, amphiphilic coatings are preferred, extending the circulation time of the particulate from minutes to hours [18]. Beside renal excretion, SPION are suggested to also biodegrade and clear from the body through the endogenous iron metabolic pathway [19]. The released iron is first metabolized in the liver and then either used in production of red blood cells or eliminated from body through kidneys.

2.3. Applications (MRI, magnetophoric mobility, hyperthermia)

In addition to tissue density, tissue relaxation properties (T_i) contribute to image contrast in MRI. During the process of T_1 relaxation, protons reorient resulting in recovery of longitudinal magnetization. During the process of T_2 relaxation, protons dephase resulting in decay of transverse magnetization. T_2^* relaxation refers to decay of transverse magnetization caused by a combination of T_2 relaxation and magnetic field inhomogeneity. Superparamagnetic nanoparticles are mostly used because of their negative enhancement effect on T_2 - and T_2^* -weighted sequences. This predominant effect on the T_2 relaxation time doesn't prevent the use of the properties of these agents on the T_1 relaxation time when appropriate imaging sequences are chosen [20,21]. The efficiency of a contrast agent or its relaxivity depends on its ability to accelerate the proton relaxation rate, which is defined as the increase of the relaxation rate of the protons of the solvent (water) induced by 1 mmol.L⁻¹ of the active ion as described in Equation 2.

$$R_i(obs) = \frac{1}{T_i(obs)} = \frac{1}{T_i(dia)} + r_i C ; i = 1 \text{ or } 2 \quad (\text{Equation 2})$$

In this equation, $R_i(obs)$ and $1/T_i(obs)$ are the global relaxation rates in an aqueous system, $T_i(dia)$ is the relaxation time of the system before addition of the contrast agent, C is the concentration of the paramagnetic center expressed in mmol.L⁻¹, and r_i is the relaxivity (s⁻¹.mmol⁻¹.L). The

effectiveness of a T_1 or T_2 contrast agent is defined by the r_2/r_1 ratio : the higher the ratio r_2/r_1 , the more efficient the T_2 agent and the better the contrast. The magnetic relaxation characteristics can be measured by studying the nuclear magnetic resonance dispersion (NMRD) profile, which finally yields information about the mean crystal size, the specific magnetization, and the Néel relaxation time [22]. The dipolar interactions between the superparamagnetic cores and surrounding solvent protons result in an increase in both longitudinal (spin-lattice) and transverse (spin-spin) relaxation rates and thus to an upgrade in the relaxivity, that is to say the effectiveness of the contrast agent. As examples, the r_1 values of commercial Resovist and Endorem are $25 \text{ mM}^{-1} \cdot \text{s}^{-1}$ and $40 \text{ mM}^{-1} \cdot \text{s}^{-1}$ respectively at 0.47 T while their r_2 values was found to be $164 \text{ mM}^{-1} \cdot \text{s}^{-1}$ and $160 \text{ mM}^{-1} \cdot \text{s}^{-1}$ at the same magnetic field strength. Thus, the r_2/r_1 ratio of Resovist and Endorem are 6.2 and 4 respectively [23]. Interesting properties have been obtained with non-commercial SPION [24,25].

Magnetic vehicles are very attractive for delivery of therapeutic agents as they can be targeted to specific locations in the body through the application of a magnetic field gradient [26]. An estimate of the magnetic force exerted onto magnetic nanoparticles by a magnet can be calculated as :

$$\vec{F}_m = N_p \vec{m}_{\text{eff}} \nabla \vec{B} \quad (\text{Equation 3})$$

where N_p is the magnetic nanoparticles number, m_{eff} is the effective magnetic moment and ∇B is the magnetic field gradient. The magnetic localization of a therapeutic agent results in the concentration of the therapy at the target site consequently reducing or eliminating the systemic drug side effects. In magnetic targeting, carriers loaded with drugs and SPION are intravenously or intra-arterially administrated. When applying an external high-gradient magnetic field at the desired site (ex : solid tumor), the magnetic moments of superparamagnetic particles are aligned with the field and the particles undergo a magnetophoretic driving force proportional to the field gradient which moves them towards the stronger field : the drug/SPION composites can be accumulated locally [27–29]. In most cases, the magnetic field gradient is generated by a strong permanent magnet, fixed outside the body over the target site. When the magnetic forces exceed the linear blood flow rates in arteries (10 cm/sec) or capillaries (0.05 cm/sec), the magnetic particles are retained at the target site by the external magnetic field. Once the carrier is concentrated at the targeted location, the drug can be released either via passive diffusion or physiological triggers such as pH, osmolality, temperature or enzymatic activity, and may be

internalized, as SPION, by cells of the target tissue or tumor cells. The intravenous injection of magnetic nanocarriers needs to be balanced against a potentially higher reticuloendothelial system clearance and requires sufficient energy magnetic fields [30,31]. The clinical success of magnetic drug targeting depends on strong magnets being able to produce high magnetic field gradients at the target sites and the modality of their application.

Magnetic hyperthermia offers the possibility of taking a drug-free approach to the treatment of cancer by localized heating of cancer cells from inside. When submitted to an alternating high-frequency magnetic field, magnetic fluids are able to release heat as a consequence of Neel and Brownian relaxation losses in single-domain particles [28,32,33]. Moderate raising the intracellular temperature to 41-47°C results in cancer cell apoptosis, whereas normal cells can tolerate this temperature [34,35]. The microenvironmental factors such as pH, oxygenation, blood perfusion, *etc.* explained such tumour sensitivity [36]]. The heating ability of a magnetic fluid is defined by the specific absorption rate (SAR), also called specific loss power (SLP), measured in Watts per g of magnetic material. It depends on the nature, the size and the structure of the particle [37]. Interesting and promising results have been obtained *in vivo* in this field for examples against osteosarcoma [38] and breast cancers [39].

An extensive surface chemistry has been developed on SPION to design coatings that allows incorporation of multiple functionalities into each grain. Among others, such modifications tend to bypass the physiological barriers such as reticulo-endothelial system, optimize circulation times, maximize targeting and uptake by the desired cells, promote intracellular trafficking or enable controlled drug release. These strategies of direct modification of the iron nanoparticles are not developed in this review but readers will find more information on reviews devoted to them [40–43]. The lipid nanoassemblies are classified here into lyotropic or non-polar lipid-based systems depending on the lipid material properties. Tables 1 and 2 summarize the description of the different systems while Table 3 focuses on the *in vivo* applications of these SPION-loaded lipid based nanoassemblies.

Table 1.1. Main characteristics of the systems based on lyotropic lipids. Data in italic have been calculated / estimated from the data available in the corresponding publications.

System type	Preparation process	Lipid composition	mean diameter (nm)	SPION			Drug			Ref
				Stabilizer	Concentration	Encapsulation Efficiency	Name	Concentration	Encapsulation efficiency	
Liposomes	Ultrasonication	*	164	PEG	<i>200 mg/mL</i>	nd	Nimodipine	<i>> 100 µg/mL</i>	95%	[54]
Liposomes	Film hydration + extrusion	DPPC Cholesterol	142-145	Citrate	Molar ratio (theoretical) : 8 mol% vs. lipid	36%	Gemcitabine	Molar ratio (theoretical) : 6 mol%	54%	[65]
Liposomes	Film hydration + extrusion	EPC- DSPE-PEG ₂₀₀₀	200	Citrate	0.53 ± 0.05 mol of Fe (III)/mol of total lipid	nd	RU 58668	3.5 mol%	nd	[55-58]
Liposomes	Film hydration + extrusion	TMAG DLPC DOPE	100	nd	187 mg/mL	nd	Docetaxel	56.8 µg/ml	nd	[61-62]
Liposomes	Film hydration + extrusion	L- α -phosphatidylcholine cholesterol, stearylamine	150-200	Citrate	nd	nd	cucurbit[7]uril zinc phthalocyanine complex	nd	nd	[63]
Liposomes	Reverse phase evaporation	DPPC DSPC DSPE-PEG ₂₀₀₀	150	Citrate	6 fg / liposome	nd	m-THPC	[m-THPC](µM) / [Fe](M) = 120 ± 15	nd	[64]
Liposomes	Film hydration + extrusion	PC	65	nd	nd	nd	5-fluorouracil	10 ⁻⁴ M	95%	[67]
Liposomes	Reverse phase evaporation + ultrasonication	Cholesterol DOPC- DPTAP- NBD-DPPE- PEG ₇₅₀ -DMPE- Fol-PEG ₂₀₀₀ -DSPE	174	Oleic acid and hydrolyzed poly (maleic anhydride-alt-1-octadecane)	1 µM	89%	Doxorubicin	2 µM	nd	[68-69]
Liposomes	Reverse phase evaporation + ultrasonication	PC Cholesterol DMPG	228	nd	nd	68%	Gemcitabine Oxaliplatin	nd	73% 78%	[59]
Liposomes	Film hydration + ultrasonication	DPPC DOPG	227	Citrate	Mass ratio (theoretical) : 25 wt% vs. lipid	83%	Paclitaxel	nd	75%	[66]
Microvesicles	Centrifugation	Natural membrane	670	Citrate	nd	nd	Foscan	0.5 µM	nd	[76]

	Magnetic sorting						Doxorubicin t-PA TPCS2a			
Exosomes	Conjugation	Natural membrane	40-110	Carboxyl-group	0.4 μg iron/ μg exosome	nd	Doxorubicin	nd	10%	[77]
Cubosomes	Film hydration + sonication	Monoolein	230	Oleic acid	nd	nd	Rhodamine 110 Octadecyl rhodamine B	nd	17%	[85]

* Composition described in the supporting informations which were not easily accessible.

Table 1.2. Main characteristics of the systems based on non-polar lipids. Data in *italic* have been calculated / estimated from the data available in the corresponding publications.

System type	Preparation process	Lipid composition	mean diameter (nm)	SPION			Drug			Ref
				Stabilizer	Concentration*	Encapsulation Efficiency	Name	Concentration*	Encapsulation efficiency	
Nanoemulsions	Solvent removing + sonication	DSPC PEG-DSPE soybean oil Cy7 PEG- DSPE	50	Oleic acid	<i>375 µg/mL</i>	100%	Prednisolone acetate vlerate	<i>0.13 mg/mL</i>	68%	[108-110]
Solid lipid nanoparticles	oil-in-water emulsion + sonication	Cetyl palmitate	248	Unknown polymer (commercial SPION)	3 wt%	> 80%	Sorafenib	$6.35 \cdot 10^{-6}$ M	90%	[119]
Solid lipid nanoparticles	Film scattering + sonication	GMS HSPC F-68	224	Oleic acid	2.16 mg/mL	nd	Cisplatin	nd	69%	[120]
Solid lipid nanoparticles	Ultrasonic dispersion	Stearic acid	127	Oleic acid			Ibuprofen	nd	80%	[121]
Solid lipid nanoparticles	solvent diffusion	Monostearin	228	Oleic acid	nd	19-83%	Doxorubicin	3%	65%	[123]
Solid lipid nanoparticles	oil-in-water emulsion + homogenization	Trilaurin	100-180	Octadecyltri-methoxysilane	20 mg/mL	40-65%	Tetracaine	$1.3 \cdot 10^{-3}$ M	nd	[124]
Solid lipid nanoparticles	High shear homogenization	Cetyl palmitate Stearic acid Tween 60	206	Oleic acid	1 wt%	nd	Methotrexate	1 wt%	98%	[125]
Solid lipid nanoparticles	Solvent diffusion	Nucleolipids DOPC	100-150	Nucleolipids	<i>100 µg/mL</i>	nd	α -tocopherol Prostacyclin	<i>0.05 mg/mL</i>	10%	[123]

Table 1.3. Summary of the in vivo biological evaluations made with the systems described in this review. Data in italic have been calculated / estimated from the data available in the corresponding publications.

System type	Drug	Objectives	In vivo evaluation						Ref
			Model	Administration route	SPIO dose	Drug dose	Magnetic field parameters	Main results	
Liposomes	Nimodipine	Magnetic guidance Imaging Early diagnosis Chemotherapy	Parkinson disease rat model (6-OHDA injection)	IP	nd	1 mg/kg/day	Magnet D10x5 mm, N35 Imaged at a 3T MRI	2.5x increase of drug concentration compared to drug solution Neuroprotective effect of drug loaded liposomes	[54]
Liposomes	RU 58668	Imaging Magnetic guidance Chemotherapy	human U87 glioblastoma	IV	12.8 μ mol/g	0.15 μ mol	Imaged at a 7T MRI	Magnetic accumulation of RU-MFLs RU 58668 anti-proliferative activity	[55-58]
Liposomes	Docetaxel	Chemotherapy Hyperthermia	Human MKN45 gastric cancer cells in Balb-c/nu/nu mice	IV	nd	7.5–15 mg/kg	a 6.36-kA/m magnetic field alternating at 478 kHz with an output power of 1 kW	Reduction of tumor volume Increase in survival rate	[61-62]
Liposomes	Gemcitabine Oxaliplatin	Chemotherapy	MCF-7 cell in BALB/c nude mice	IV	nd	9-35 μ g/g 1.25-5 mg/kg	5000 G	Minimization of tumor size Inhibition of MCF-7cell growth	[59]
Liposome	Foscan	Imaging Hyperthermia Phototherapy	Carcinoma A431 cells into NMRI nude mice	Intratumoral	<i>90 mg/kg</i>	<i>0.16 mg/kg</i>	30 mT at 111 kHz for 30 min Imaged at 4.7T	Complete tumor regression with the dual therapy	[64]
Exosomes	Doxorubicin	Chemotherapy	Kunming mice bearing a subcutaneous H22 cancer	IV	nd	5 mg/kg	Magnet 1T	Enhancement of cancer targeting under external magnetic field Suppression of tumor growth	[76]
Nanoemulsion functionalized with RGD peptide	Prednisolone valerate acetate	Imaging Chemotherapy	Colon cancer model (LS174T) in Swiss nude mice	IV (tail vein)	30 mg/kg	10 mg/kg	Imaged at a 3T whole body MR scanner	Significant accumulation of the nanoemulsion in the tumors. Potent inhibitory effect on tumor growth in all animals treated with drug loaded nanoemulsion.	[108-110]
Magnetic Solid Lipid Nanoparticles	Cisplatin	Chemotherapy	human cervical carcinoma SiHa cells into	IV (tail vein)	nd	0.6 mg/kg	cylindrical rubidium iron boron rare earth	High drug concentrations	[120]

			female mice AIB/C)	nude (B				magnet (4500 G)		
--	--	--	--------------------------	------------	--	--	--	--------------------	--	--

3. Magnetic-fluid-loaded lipid-based nanoscale systems

3.1. Systems based on lyotropic lipids

3.1.1. Synthetic vesicles : liposomes

Described first in the 1960s by Bangham [44], liposomes are core-shell structures defined as closed vesicles delimited by one or several concentric hydrated lipid bilayers that entrap a part of the aqueous phase where they have been formed. Usually, liposomes are mainly composed of phospholipids. The advantage of these structures lies in their double ability to incorporate hydrophobic or amphiphilic compounds in their bilayer shell and to encapsulate hydrophilic substances in their inner aqueous core. The latter property has been successfully exploited to load liposomes with a hydrophilic magnetic fluid conveniently stabilized either through electrostatic repulsion of the iron oxide nanocrystals ensured by surface-binding of charged molecules, typically trisodium citrate, or through steric repulsion obtained by surface-coating with hydrophilic polymers such as chitosan, poly(ethylene glycol) (PEG), dextran, poly(vinyl alcohol) (PVA), poly(vinyl pyrrolidone) (PVP), alginate [45–50]. Magnetic-fluid-loaded liposomes (MFL), also referred to as magnetoliposomes, have been often prepared by lipid film hydration with the aqueous suspension of superparamagnetic grains to be encapsulated, followed by sequential extrusion that provides calibrated unilamellar vesicles of submicronic size. This procedure advantageously preserves the individuality of the iron oxide nanocrystals constituting the magnetic fluid and then their initial superparamagnetic behaviour. The last preparation step corresponds to liposome purification by removal of the non-encapsulated material. While many works and several reviews [7,51–54] deal with liposomes incorporating SPION, the following descriptions focus on systems where drugs are co-encapsulated and are classified regarding the main role of SPION.

3.1.1.1. Magnetic guidance

Martina *et al.* succeeded in the production of MFL composed of Egg-yolk L- α -phosphatidylcholine (EPC) and 1,2-diacyl-SN-glycero-3-phosphoethanolamine-*N*-[methoxy (poly (ethylene glycol))-2000] (DSPE-PEG₂₀₀₀), used as steric stabilizer, and encapsulating a concentrated suspension of maghemite nanoparticles obtained by coprecipitation of Fe²⁺/Fe³⁺ salts and electrostatically stabilized with trisodium citrate [55]. Sequential extrusion followed by size exclusion chromatography to remove non-encapsulated material led to liposomes with a mean hydrodynamic diameter of 200 ± 50 nm and an iron loading of 0.53 ± 0.05 mole of Fe(III) per mole of total lipid (Figure 1.1A). The associate relaxivities are 18.6 ± 0.5 mM⁻¹.s⁻¹

and $116.0 \pm 5.8 \text{ mM}^{-1} \cdot \text{s}^{-1}$ at 0.47 T for r_1 and r_2 respectively and the r_2/r_1 ratio is 6.2 whereas the relaxivities of the ferrofluid are $36,0 \pm 1,0 \text{ mM}^{-1} \cdot \text{s}^{-1}$ and $108.0 \pm 5.4 \text{ mM}^{-1} \cdot \text{s}^{-1}$ for r_1 and r_2 respectively and the r_2/r_1 ratio is 3 under the same conditions [55]. The pharmacokinetic profile of these liposomes (200 μL of 200 nm-MFL, 20 mM total lipids, 34 mM Fe(III), 14 μg iron per g of mouse) indicates a biphasic elimination of the MFL from blood that consisted in a rapid elimination stage of MFL within the first two hours followed by a much slower elimination stage. Tissue distribution of SPION entrapped in MFL highlights preferential and progressive accumulation within liver and spleen [56]. As assessed by *in vivo* 7-T MRI and *ex vivo* electron spin resonance, four hours exposure to a magnetic field gradient (155-T/m) efficiently concentrates MFL into human U87 glioblastoma implanted in the striatum of mice while avoiding healthy brain tissues [57]. Loaded with a lipophilic anti-estrogen (RU 58668) into their bilayer, such liposomes gave promising results for the treatment of hormone-dependent breast cancer [58]. Experiments on mice bearing MCF-7 xenografts have clearly shown that the accumulation of RU loaded-MFL at the tumor site is increased in the presence of magnetic field gradient and tumor growth can be significantly reduced compared to the non-targeted tumors (Figure 1.1B).

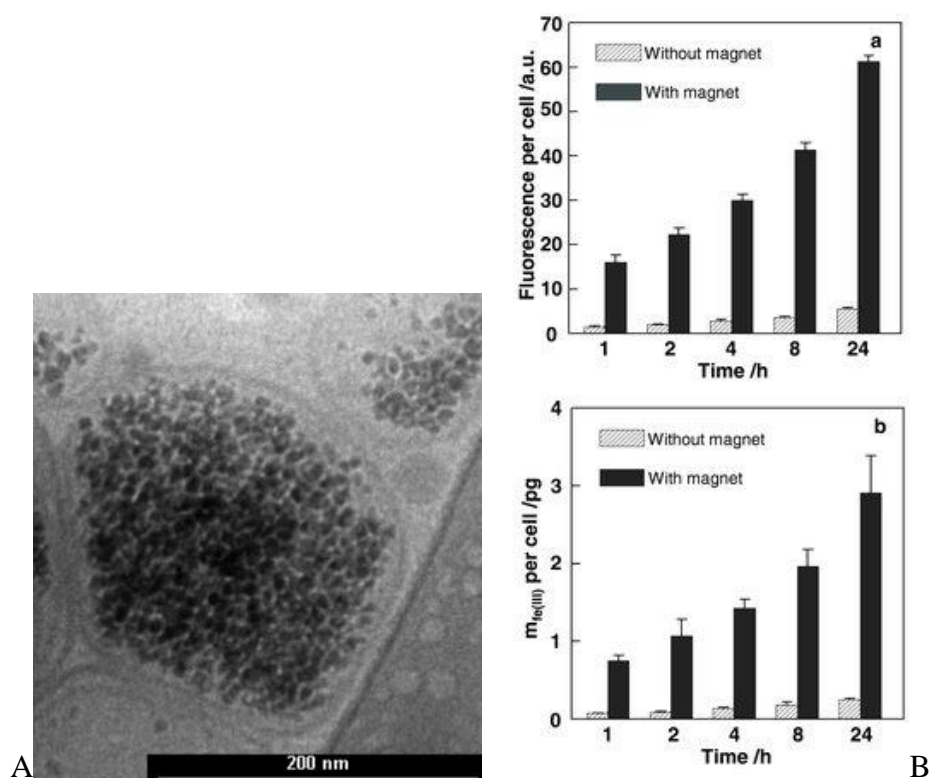


Figure 1.1. A : Cryo-TEM micrographs of EPC:DSPE-PEG2000 (95:5 mol %) MFL with 1.8 mol of ferrofluid loaded per mol of lipids. Total lipid concentration is equal to 1 mM [55]. B : Total association of RU-MFLs with MCF-7 cells at 37 °C (400 nmol of total lipids and 600 nmol of Fe(III) per 106 cells; [lipids] = $0.4 \times 10^{-3}M$; [Fe(III)] = $0.6 \times 10^{-3}M$) as a function of incubation period of time and in the presence or absence of a 0.44 T magnet; lipids (a) and iron mass mFe(III) (b) uptakes from rhodamine-fluorescence counting [58]. With permissions.

Fixed-dose combination (FDC) products that consider the co-administration into a single vehicle of two or more drugs with synergistic activities, have aroused growing interest in the field of drug delivery. First step towards combined chemotherapies have been undertaken by Ye *et al.* in 2016 by developing gemcitabine and oxaliplatin-containing magnetoliposomes for breast cancer treatment. In the optimal formulation, the lipid molar ratio was PC/cholesterol/dimyristoyl phosphatidyl glycerol : 6:4:1. The mean hydrodynamic diameter of gemcitabine-containing magnetoliposomes (GML) and oxaliplatin-containing magnetoliposomes (OML) was 228 and 169 nm, the polydispersity index (PdI) of GML and OML was close to 0.133 and 0.060, and their drug-encapsulation efficiency was 73% and 78% respectively. The field-responsive behavior of magnetoliposome particles was demonstrated : the complete magnetic attraction of core/shell particles toward a 400 mT permanent magnet

occurred in less than 2 min. Such magnetic responsiveness would provide a useful nanotool in accumulating the 5-fluorouracil (5-FU) dose into the tumor mass [59].

3.1.1.2. Hyperthermia

Pioneer works coupling hyperthermia and drug release, here 5-FU, were made twenty years ago in the Horikoshi's group [60]. More recently, Yoshida *et al.* studied the effectiveness of chemohyperthermia with docetaxel-embedded cationic magnetoliposomes (DML) and an applied alternating current magnetic field. DML have an average hydrodynamic diameter about 100 nm and the mean magnetite concentration is 187 ± 22 mg/mL. In the mice that were injected with DML at a docetaxel concentration of 57 μ g/mL and exposed to the alternative current magnetic field of 1 kW, tumor size was significantly decreased after treatment. The tumor disappeared in 3 mice in the DML group exposed to the magnetic field, 2 mice survived over 6 months after treatment, whereas all mice of the other groups died after 15 weeks. Histological investigation demonstrated that DML diffuse homogeneously and DML-mediated hyperthermia damage tumor cells [61]. Moreover, docetaxel and tumor necrosis factor- α concentrations, the cell cycle, and cell death rates in the tumor were examined. Three days after injection, the docetaxel concentrations were significantly higher in the DML injected groups compared to free drug injection. The rate of tumor cell death increased in the DML-injected group, whether with hyperthermia or not, and the tumor necrosis factor- α concentration in the tumor treated with DML with heating remained at a high level on the 7th day after treatment, while it decreased after one day in other groups [62].

Other therapeutic modalities of magnetoliposome have been experienced such as the combination of hyperthermia and photodynamic effect on melanoma by preparing stearylamine containing magnetoliposome loaded with cucurbit-7-uril zinc phthalocyanine complex (CB:ZnPc) and citrate-coated SPION. The authors made a lipid film of soya phosphatidylcholine, cholesterol, stearylamine and the CB:ZnPc. Hyperthermia has been investigated in combination with photodynamic therapy on melanoma cells (B16-F10) and the *in vitro* results showed that magnetohyperthermia can act synergistically along with photodynamic effect [63]. For instance, B16-F10 cells treated with the highest light dose (2.0 J cm^{-2}) and subsequent AC magnetic field activation (1 MHz and 40 Oe amplitude, during 3 min) had viability reduced to about 13%. The same combined therapy was investigated with DPPC/DSPC/DSPE-PEG2000 liposomes loaded with Foscan, a photosensitizer, and citrated SPION [64]. The comparison between *in vitro* (Human adenocarcinoma SKOV-3 cells) and *in*

in vivo (epidermoid carcinoma A431 cells in NMRI nude mice) results is very interesting here as photodynamic therapy was more effective *in vitro* and magnetic therapy *in vivo*. Still, the combination of the two therapies brought the best results both *in vitro* and *in vivo*.

Interestingly, the release of the drug can be controlled by the liposomal carrier and/or by the hyperthermia effect. Ferreira *et al.* reported the preparation and characterization of thermosensitive ML containing gemcitabine for combined hyperthermia and chemotherapy. These unilamellar liposomes have a hydrodynamic diameter of 145 nm, a PDI of 0.10 and a zeta potential of -9 mV. The encapsulation efficiencies of the gemcitabine and SPION in ML were 54% and 36%, respectively. For hyperthermia applications, the temperature of tumor tissue must reach 42 °C–45 °C for effective therapy. Here, when the samples were exposed to an alternative magnetic field (AMF) of 356 kHz for 5 min, the temperature ranged from 32 °C to approximately 56 °C which is appropriate for effective hyperthermia treatments. AMF-triggered local heating induces fluidification of the DPPC/cholesterol bilayer which becomes more permeable. Therefore, a 70% drug release was observed after 5 min of exposure against only around 10% after 72 hours at 37°C [65]. Kulshrestha *et al.* obtained the same type of results with paclitaxel loaded DPPC/DOPG-based ML [66]. In that case, only 1.2% of the drug was released after 30 min at 37°C while under AMF (10 kA/m; 423 kHz), the temperature raised to 43°C and the release to 55.6%.

A more controlled release has been obtained with multilamellar ML, having a mean hydrodynamic size of 65 ± 20 nm, and loaded with 5-FU, against colon cancer. Under exposure to a high frequency magnetic field gradient, the oscillation of the magnetic moment of ML transformed them into heaters, reaching the minimum hyperthermia temperature (41°C) in 22 min and a maximum temperature (45°C) was achieved after 27 min. The release of 5-FU entrapped within the ML showed first order kinetics as the release rate decreases with time. When the release medium was coupled to a high frequency alternating electromagnetic field (250 kHz, 4 kA/m), 5-FU release was significantly accelerated but remained prolonged (Figure 1.2) [67].

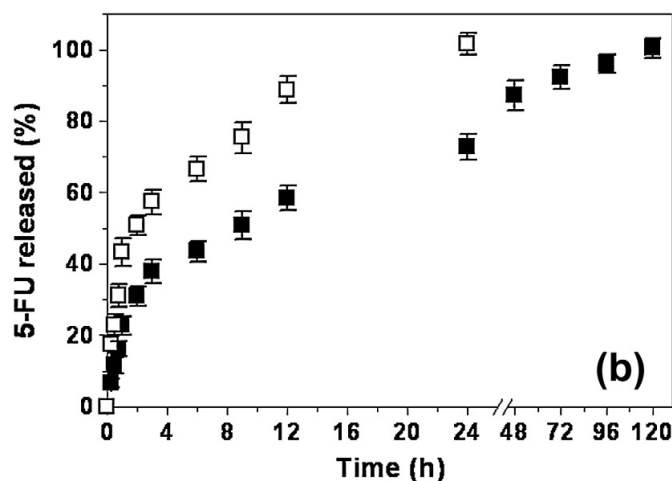


Figure 1.2. Release of 5-FU entrapped from magnetoliposomes as a function of the incubation time in PBS ($pH = 7.4 \pm 0.1$) in the absence (\blacksquare , $37.0 \pm 0.5^\circ\text{C}$), or under the influence (\square , $45.0 \pm 1.0^\circ\text{C}$) of a high frequency alternating electromagnetic field gradient [67]. With permission.

Chen *et al.* developed PEG-stabilized ML containing SPION in their bilayer shell and the anticancer drug doxorubicin (DOX) as stimuli-responsive DDS for low-dose chemotherapy [68]. This system referred to as dMLs was prepared by a reverse phase evaporation method from a chloroformic solution of the constituting lipids (DPPC/ DSPE-PEG₇₅₀ at 95:5 mol%) and commercially OA-SPION mixed with a DOX aqueous solution in phosphate buffer (PBS). Liposome calibration was carried out by extrusion and final dMLs were characterized by a mean hydrodynamic diameter of ~ 120 nm. Low-dose chemotherapy of Huh-7 cells was achieved by radio frequencies triggered release of DOX from dMLs by increasing the fluidity of the phospholipid bilayer which is sensitive to the temperature, where cellular uptake was governed by dML diffusion within the culture media consistent with a non-targeted delivery vehicle [68].

To improve the treatment selectivity, it is possible to graft onto the surface of drug-loaded ML specific ligands capable of biochemical targeting. Folate-targeted cationic magnetoliposomes (FTML) composed of 1,2-dioleoyl-sn-glycero-3-phosphocholine (DOPC), 1,2-dipalmitoyl-3-trimethylammonium propane (DPTAP), 1,2-dipalmitoyl-sn-glycero-3-phosphoethanolamine-N-(7-nitro-2-1,3-benzoxadiazol-4-yl) (NBD-DMPE), 1,2-dimyristoyl-sn-glycero-3-phosphoethanolamine-N-[methoxy(polyethylene glycol)-750] (PEG750-DMPE), and 1,2-distearoyl-sn-glycero-3-phosphoethanolamine-N-[folate (polyethylene glycol)-2000] (Fol-DSPE-PEG₂₀₀₀) and co-encapsulating DOX have been prepared [69]. FTML were prepared at 10 mM total lipid by thin film hydration followed by extrusion and centrifugation was used in

order to remove unencapsulated SPION. The final ML were characterized by an average static diameter of 174 ± 53 nm by cryoTEM and SPION encapsulation efficiency of 89% from inductively coupled plasma mass spectrometry. Cell uptake experiments were carried out on HeLa (cervical cancer cells) and ZR-75 (human breast carcinoma) cell lines to assess targeting efficiency. The uptake of FTML or MFL (devoid of folate receptor targeting lipid) by HeLa cells was observed indifferently up to 120 min but was greater with FTML at 180 min. In comparison, no FTML or MFL uptake was observed in ZR-75-1 cells. This result is consistent with FOLR1 expression results, where HeLa cells showed 42.5-fold greater expression than ZR-75-1 [69]. With radio frequencies heating similar to that used for tumor ablation, a threefold increase in DOX release was observed.

3.1.2. Natural vesicles : microvesicles and exosomes

Microvesicles and exosomes are vesicles produced endogenously by mammal cells [70]. Microvesicles have size range between 100 to 1000 nm while exosomes are smaller, between 30 to 100 nm. These extracellular vesicles carry lipids, proteins, receptors and effectors molecules and participate to the distant intercellular communications. Regarding briefly their formation mechanism, microvesicles originate from the budding of the plasma membrane while exosome is derived from endosome formed from plasma membrane [71]. Interestingly, after isolation by differential centrifugation or magnetic sorting with magnetic antibodies, these natural vesicles show excellent *in-vivo* stability, are less cytotoxic than synthetic vesicles [72] and can be loaded with SPION [73–75]. Silva et al. produced microvesicles loaded with SPION and four different drugs, a clinical photosensitizer drug (Foscan), disulfonated tetraphenylchlorin (TPCS2a), DOX and tissue-plasminogen activator (t-PA) from the less to the more hydrophilic [76]. Microvesicles having size ~670 nm and PDI ~0.3 were obtained after 2h-incubation of THP-1 macrophages with SPION and drug of interest, serum depletion to induce cell stress and isolation. Magnetophoresis experiments confirmed the co-encapsulation of SPION and fluorescent drugs. At last, spatial targeting with magnet and therapeutic effect have been proven *in vitro* on SKOV-3 human ovarian cancer cells and PC-3 human prostate cancer cells with the system incorporating the photosensitizer drug. Qi *et al.* developed recently a dual-functional exosome-based superparamagnetic nanoparticle cluster for tumor-targeting drug delivery. Briefly, fresh serum is collected from healthy Kunming mice and predialyzed against PBS. The conjugation of holo-transferrins to carboxyl-group-functionalized Fe₃O₄ nanoparticles leads to the formation of iron-loaded transferrins (M-Tfs). Incubation of M-Tfs

with predialyzed serum allowed multiple M-Tfs to bind to each reticulocytes-derived exosome through a Tf–Tf receptor interaction to form reticulocytes-exosome-based superparamagnetic nanoparticle cluster (SMNC-EXOs) with a concentration of 0.40-0.45 μg iron/ μg exosome. These clusters are then purified *via* magnetic separation and redispersed into PBS. SMNC-EXOs was incubated in the presence of DOX in order to form drug-loaded SMNC-EXOs (D-SMNC-EXOs) with hydrodynamic diameters in the 40-110 nm range. The quantitative analysis of UV-visible absorption indicated a DOX loading capacity of 10%. After being injected intravenously into homologous mice bearing hepatoma 22 subcutaneous cancer cells, D-SMNC-EXOs accumulated in the tumor region and released DOX to suppress tumor growth when an external magnetic field was applied (Figure 1.3) [77]. Very recently, Piffoux and al. compared different methods to produce exosomes containing SPION and Foscan [78]. The impact of the production and purification protocols on SPION and photosensitizer loadings, yield and purity was investigated.

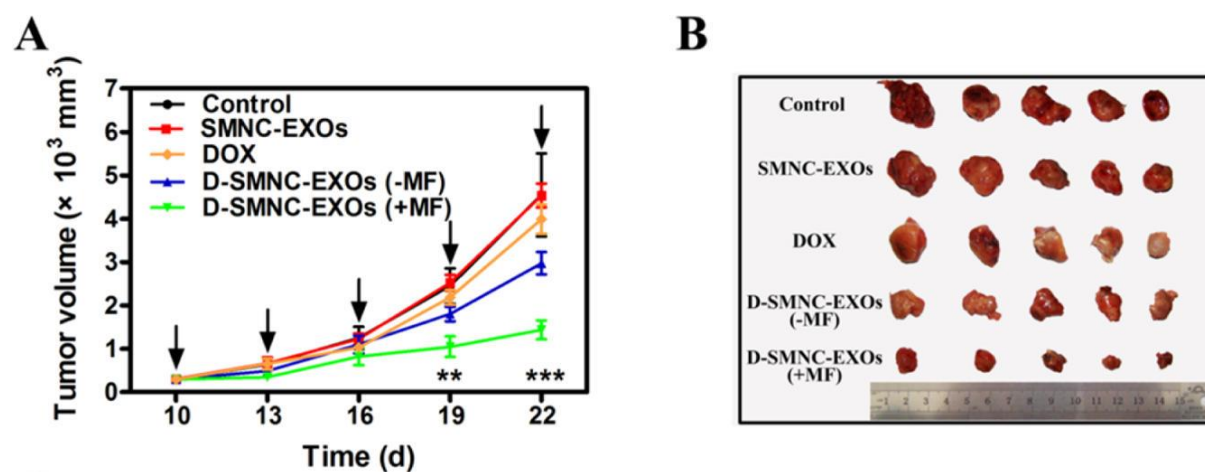


Figure 1.3. (A) Growth evaluation of hepatoma 22 subcutaneous cancer in Kunming mice after sample administration. Tumor volume was examined every 3 days for 12 consecutive days ; (B) Hepatoma 22 tumor tissues obtained from euthanized mice 12 days after sample administration [77].

3.1.3. Compartmented nanoparticles

Bicontinuous cubic lipid phases consist of a single lipid bilayer membrane that adapts an infinite periodic minimal surface dividing the space into two non-intersecting networks of water channels. This particular liquid crystalline state forms spontaneously at proper conditions upon mixing with water some lyotropic lipids with various polar head groups, the most often used

ones being monoglycerides [79,80]. In excess water, application of high-energy dispersion, i.e., sonication or homogenization, can lead to nanoscale particles or ISAsomes (Internally self-assembled “somes”) , typically ranging from 10 to 500 nm in size and of well-established biocompatibility [81,82]. Depending on their internal organization, mainly bicontinuous cubic or reverse hexagonal phases, two types of particles have been described, cubosomes and hexosomes. They can be stabilized by using surfactants, e.g., poloxamer 407, or hydrophilic polymers, e.g. PVA, in proportions generally not exceeding from 2.5% to 10% w/w with respect to the total weight of the dispersion. Due to their small pore size (5-10 nm) and their ability to solubilize hydrophobic, hydrophilic and amphiphilic molecules, cubosomes find many potential applications in the field of oral, topical and intravenous DDS [83].

Acharya *et al.* described the preparation of hybrid superparamagnetic mesophase nanoparticles (HMNs). In this system, OA-SPION were dispersed in the cubic phase forming the glycolipidic (phytantriol) matrix of the nanoparticles. These cubosomes have a hydrodynamic diameter of 180 nm and the SPION concentration used (0.3 wt% Fe in phytantriol) has not compromised the internal structure of the bicontinuous cubic phase (Figure 1.4). Transverse relaxivity (r_2) measurements show that enhancement of the transverse relaxivity r_2 of the magnetic cubosomes is proportional to the loading of OA-SPION in the mesophase nanoparticles [84].

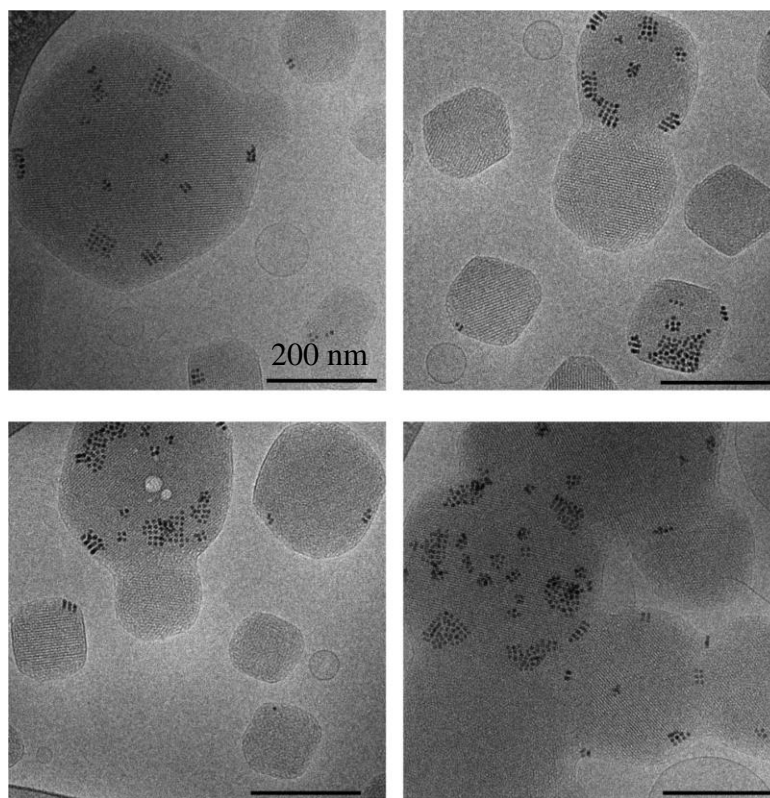
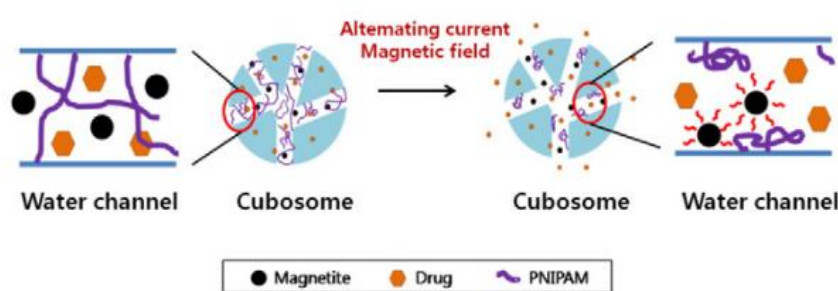


Figure 1.4. Cryo-TEM images of mesophase nanoparticles loaded with 8-nm spherical OA-SPION at 0.3 wt% Fe concentration in phytantriol. SPION ordering within the inner bicontinuous cubic structure of the nanoparticles can be seen [84]. With permission.

More recently, Montis *et al.* developed a new nanostructured drug delivery by including OA-SPION in the bilayer membrane of bicontinuous cubic lipid nanoparticles of glyceryl monooleate (monoolein). The first results showed that magnetocubosomes are able to host both model hydrophilic and hydrophobic therapeutics, rhodamine 110 and octadecyl rhodamine B respectively, in separated compartments, and to release the payload in a space and time controlled manner, upon application of a low frequency AMF of 6 kHz. Magnetic-field-induced structural destabilization of the bilayer of the cubosomes with the formation of pores allowed the escape of drugs from the aqueous channels, acting as a release trigger [85].

Hong *et al.* prepared iron oxide nanoparticles within monoolein cubic phase. The cubic phase was obtained by hydrating molten monoolein with a $\text{Fe}^{2+}/\text{Fe}^{3+}$ salt aqueous solution that was allowed to co-precipitate with an alkali solution into SPION inside the aqueous channels delimited by the monoolein bilayer. Micronizing these cubic phases finally led to the formation of superparamagnetic cubosomes, responsive to a magnet, and the magnetic interaction degree, measured by the percent of decrease in monoolein concentration after magnetic fields were

applied to cubosome suspensions, is proportional to the amount of SPION formed within the cubic phases [86]. These authors also tried to do the same using a mixture of monoolein and oleic acid (OA) which was included in the cubosomes in order to electrostatically adsorb $\text{Fe}^{2+}/\text{Fe}^{3+}$ at the lipid - water interface. In order to control and trigger the drug release, a thermosensitive polymer, poly(*N*-isopropylacrylamide), has been dissolved in the water phase in order to increase its viscosity. Under an alternating magnetic field, magnetite in the cubosome will produce heat and increase the temperature of the medium. Consequently, poly(*N*-isopropylacrylamide) immobilized in the water channel undergoes a phase transition, reducing the viscosity and controlling the drug release from the cubosomes (Figure 1.5) [87].



*Figure 1.5. Magnetite and poly(*N*-isopropylacrylamide) were incorporated in monoolein and oleic acid cubosomes. Magnetite generates heat under an alternative current magnetic field, *Hm*PNIPAM in the water channel of the cubosome becomes water-insoluble and assumes a contracted form when the temperature increases above the phase transition temperature. Accordingly, the thermo-sensitive polymer will act as a thermal valve in the water channels of the cubosomes [87].*

3.2. Systems based on non-polar lipids

3.2.1. Nanoemulsions

Nanoemulsions (NE), defined as liquid-liquid biphasic dispersions at the nanometer scale, have growing interest as colloidal drug carriers, notably for intravenous administration, from parenteral nutrition to drug transportation [88,89], or for oral administration of poorly water-soluble drugs since they have been shown to increase drug bioavailability through the enhancement of the intestinal absorption [90]. Besides, the specific advantages of NE over other nanotechnologies used for drug delivery, are their high loading capacity for lipophilic drug, formulation stability, ease of manufacture and their relatively low complexity [91]. NE-based systems for the prevention and treatment of cancer, inflammatory diseases and adjuvant

delivery in immunotherapy have been investigated and marketed [92–95]. NE can be prepared by two major techniques, *i.e.*, high-energy and low-energy emulsifications. High-energy emulsification methods include high-shear stirring, high-pressure homogenization and ultrasound generators. Low-energy emulsification methods are emulsification methods making use of the chemical energy stored in the components and are receiving increased attention. In these methods, NE are obtained as a result of phase transitions produced during the emulsification process [96].

Pharmaceutically used and approved NE are mostly composed of an oil phase dispersed in a continuous aqueous phase as droplets with submicronic size, preferentially with maximum radius below 200 nm [60]. Regarding SPION-loaded NE, the iron oxide nanoparticles have been made stable in the oil phase by coating them with hydrocarbon chains through binding of OA via its carboxylic head group (OA-SPION) [97–99], phosphoesters via their phosphonates head group [100–103] or silanes derivatives [104–107].

Jarzyna *et al.* developed a bimodal-platform by co-incorporating in NE droplets the near-infrared fluorescent lipid dye Cy5.5-PEG-DSPE and commercially available OA-SPION based on magnetite. These were composed of a hydrophobic oil core made of soybean oil, distearoyl phosphatidylcholine (DSPC) and DSPE-PEG₂₀₀₀, dispersed in water phase by injection of a chloroformic solution at 100°C before solvent removing followed by sonication in order to form calibrated droplets with mean hydrodynamic diameters of 30, 60, or 95 nm, respectively (Figure 1.6), depending on the relative proportions of the different lipid components. Inductively coupled plasma mass spectrometry (ICPMS) analysis revealed nearly a 100% encapsulation efficacy of magnetite, then similar SPION number to droplet volume ratios, leading to r_1 values of $2.5 \pm 0.4 \text{ mM}^{-1}\text{s}^{-1}$, to $2.7 \pm 0.3 \text{ mM}^{-1}\text{s}^{-1}$, to $2.9 \pm 0.3 \text{ mM}^{-1}\text{s}^{-1}$ at 1.41 T for the 30, 60, and 95 nm emulsions, respectively and high r_2 values of $76 \pm 1 \text{ mM}^{-1}\text{s}^{-1}$, $136 \pm 9 \text{ mM}^{-1}\text{s}^{-1}$ or $184 \pm 7 \text{ mM}^{-1}\text{s}^{-1}$ at the same field for NE of 30 nm, 60 nm or 95 nm in droplet diameter, respectively. The conjugation of a near infrared fluorophore allowing optical imaging, demonstrated the accumulation of this nanocomposite in subcutaneous human tumors in nude mice confirmed with MRI imaging *in vivo* [108].

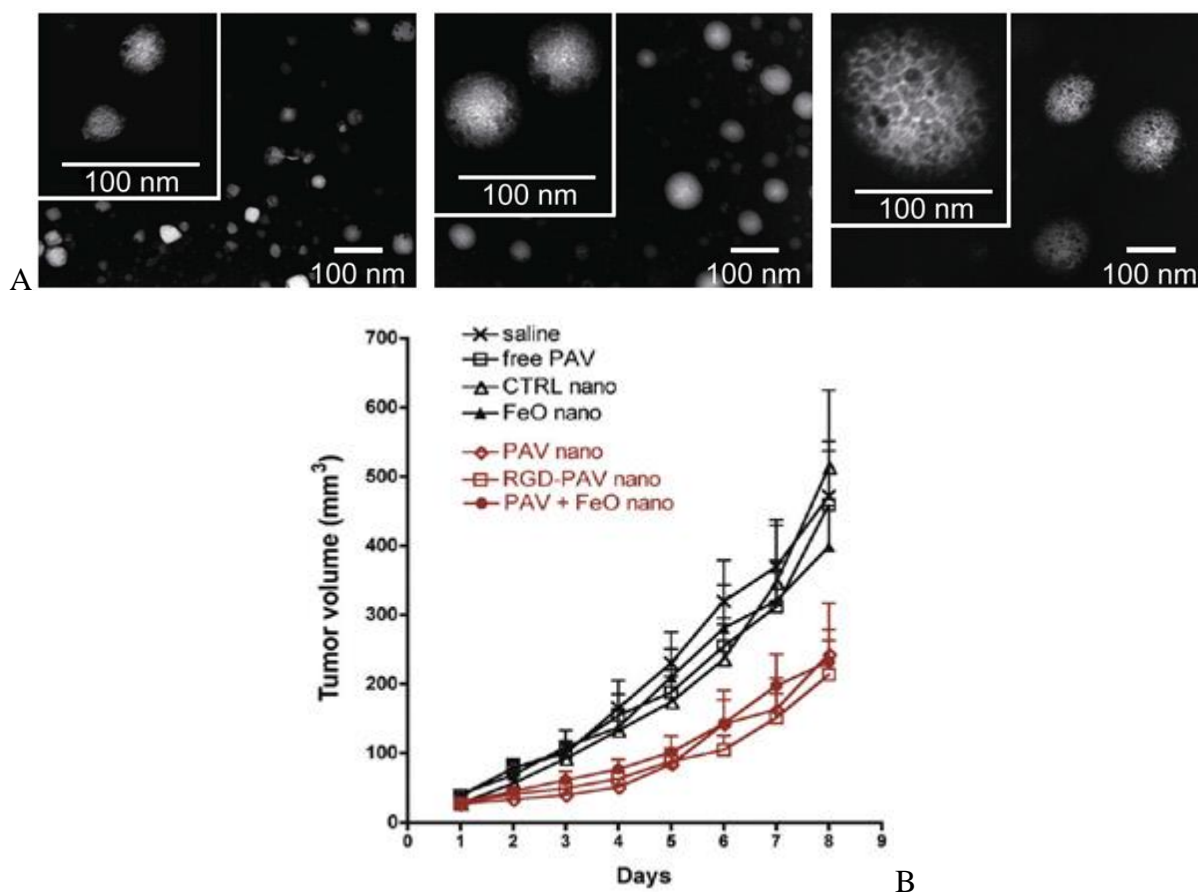


Figure 1.6. A : Negative stain transmission electron microscopy (TEM) images of the different nanoemulsion formulations [108]. B : Starting at day 6, tumor growth profiles of the PAV nanoemulsion treated groups compared to saline, control nanoemulsions, FeO nanoemulsions, and free PAV injected groups [109]. With permissions

To go further, the same team has functionalized the NE with $\alpha_v\beta_3$ -specific RGD peptides to enable specific molecular MRI and optical imaging of tumor angiogenesis. The cyclic peptide RGD was conjugated to the NE droplets coated by DSPE-PEG-maleimide units via the sulfhydrylmaleimide coupling method resulting in a NE (RGD-NE) with a mean droplet diameter of 90 ± 10 nm. MR images at 3T after IV injection of RGD-NE showed a lowering of signal intensity in the tumor periphery where angiogenesis activity is the highest. RGD-NE fluorescence was found co-localized with endothelial cell staining, as observed in tumor sections [110]. The latest advance for this system was to incorporate a hydrophobic drug, prednisolone valerate acetate (PAV), for theranostic applications. In this case, PAV was included in the lipophilic phase during the fabrication process which led to NE with droplet mean diameter of 53 nm. This system has proven its efficiency in tumor growth inhibition in mice after intravenous injection compared to drug-free NE, SPION-loaded NE and free PAV ethanolic solution at a dose of 10 mg PAV/kg (Figure 1.6) [109].

3.2.2. Solid lipid nanoparticles

Unlike NE which are only constituted by lipids in their liquid state, solid lipid nanoparticles (SLN) and nanostructured lipid carriers (NLC) result from the dispersion in an aqueous phase of lipids which are totally (SLN) or partly (NLC) in their solid state. SLN are usually composed of non-polar lipids long-chain glycerids, waxes or fatty-acids [111–117] crystallized at room temperature while NLC are produced by mixing solid and liquid (oil) lipids at the same temperature [116]. Both systems result from the dispersion of the lipids into a liquid state, by melting or dissolution into adequate solvent, and then the solidification of the droplets by cooling or solvent evaporation. The small size of the particles is obtained thanks to the use of high-energy dispersers (as NE) or solvent diffusion – evaporation phenomenon. SPION are analogous to those incorporated into NE.

The first reported SLN system encapsulating magnetite was described in 1996 by Muller *et al.* It was composed of trilaurin and Poloxamer 188 as stabilizer and obtained by high-pressure homogenization [118]. Grillone *et al.* present the development of Sorafenib-loaded magnetic SLN using cetyl palmitate as lipid matrix. To obtain this system, the lipid, commercially lipophilic SPION and Sorafenib are dissolved into solvents and then added in an hydrophilic phase containing Tween 80 in water at 75°C. This oil-in-water emulsion is homogenized using sonication at high temperature to evaporate the solvents. The final dispersion was maintained at 4 °C to allow the crystallization of the lipids and the formation of the SLN with an average hydrodynamic diameter of 248 ± 113 nm. A SPION loading of about 3 wt% could be estimated by thermogravimetric analysis (TGA) whereas the encapsulation efficiency of Sorafenib is about 90%, assessed by UV–Visible absorption. The resulting magnetic SLN do not alter significantly the viability of HepG2 cells and those loaded with Sorafenib are able to inhibit cancer cell proliferation through the drug cytotoxic action, and to enhance/localize this effect in a desired area thanks to a magnetically driven accumulation of the drug with a 1.32 T permanent neodymium magnet. The quantitative determination of cell mortality, evaluated as percentage of cells positive for ethidium homodimer-1, resulted to be about 95% in the channel close to the magnet, and 5% in the control compartment [119].

Zhao *et al.* developed the preparation and the characterization of cisplatin-loaded magnetic SLN by film scattering ultrasonic technique. The results are very promising in terms of drug and OA-SPION loads and in vivo response to an external magnetic field [120]. However, the high encapsulation efficiency ($69 \pm 4\%$) of the drug, which is hydrophilic, by these hydrophobic

particles should be investigated more carefully. Less classically, SLN could also be formed with nucleolipids in order to produce promising neutral or charged nanoparticles that have been loaded with SPION and α -tocopherol or Prostacyclin for image-guided therapy of atherosclerosis [121].

The release kinetics of drugs carried by magnetic SLN has been investigated. Two modalities have been experienced according to either a prolonged release process or a triggered release one. The first approach aimed at showing the stability of drug incorporation in the magnetic lipid particles while the second one focused on the possibility to control the drug release by submitting the co-encapsulated SPION to an alternative magnetic field. Pang *et al.* prepared by ultrasonic dispersion SLN composed of stearic acid and loaded with OA-SPION as well as with ibuprofen. The resulting ibuprofen-loaded magnetic SLN (IBMSLN) were characterized by an average hydrodynamic diameter of 127 ± 17 nm and drug encapsulation efficiency close to 80%. Superconducting quantum interference device (SQUID) measurements indicated that IBMSLN exhibit superparamagnetic behavior with a blocking temperature of 86 K. The cumulative drug passive release from IBMSLN is increased from 2 % to 27 % over the period of 1 to 8 hours and to 78 % after 40 hours (Figure 1.7). The ibuprofen release results show that the drug release by diffusion can be controlled in the magnetic nanoparticles and make this system a potential useful tool in drug delivery [122]. Similar passively-controlled releases have been described by Ying *et al.* with magnetic monostearin-based SLN carrying DOX [123].

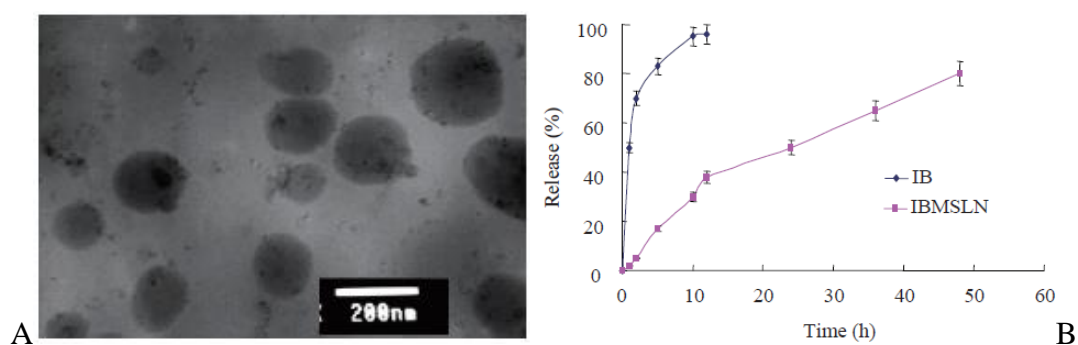


Figure 1.7. A : TEM image of non purified IBMSLN; B : cumulative release curve of ibuprofen (IB) from IBMSLN [122]. With permission.

To obtain a triggered release, Hsu *et al.* describe another SLN system in which γ -Fe₂O₃ nanoparticles were surface-grafted with octadecyltrimethoxysilane groups. These lipophilic SPION-were then dispersed and stirred in a melted lipid matrix composed of trilaurin and

containing a lipophilic drug (tetracaine) before being emulsified in an aqueous solution made of deionized water and a surfactant (Poloxamer 188). Afterward, the lipid-in-water emulsion was refined using a high-pressure homogenizer to decrease the droplets size. At the end, the lipid-in-water emulsion was cooled down to form magnetic SLN with average hydrodynamic diameters between 100 and 180 nm. When exposed to an AMF of 60 kA/m at 25 kHz, magnetic SLN showed a significant increase in temperature up to 8°C. Meanwhile, the dissipated heat melted the lipids surrounding the iron oxide grains resulting in an accelerated release of the encapsulated drug. The authors measured that after a heating period of 20 minutes, 35% of the initially encapsulated tetracaine was released from the lipid nanoparticles while without heating, the tetracaine release throughout a 30-day period at room-temperature storage was found to be less than a 5-min exposure to magnetic heating [124].

Similarly to liposomes, biochemical targeting investigations have been done with SPION-loaded SLN. In this respect, Albuquerque *et al.* combined high shear homogenization and ultrasonication to develop a new theranostic tool for early detection by MRI imaging and treatment of rheumatoid arthritis through intravenous administration that consisted in methotrexate (MTX)-loaded SLN incorporating OA-SPION using an organic solvent-free method. These SLN are functionalized with a monoclonal antibody against the macrophage specific cell surface receptor, CD64, overexpressed in rheumatoid arthritis. Solid lipids (cetyl palmitate, stearic acid and Tween 60) are heat at 70 °C and then mixed with MTX, OA-SPION and water. The resulting emulsion was immediately homogenized by sonication and cooled to produce the SLN. The SLN are further functionalized with the anti-CD64 antibody. Monodisperse nanoparticles with a hydrodynamic diameter of 206 ± 3 nm were yielded and 98% MTX encapsulation rate. Transmission electron microscopy images indicated that the SPION are encapsulated inside the lipid matrix. MTT assays on THP-1 macrophages indicated that the antibody-conjugated formulations had no significant difference in viability compared to non-conjugated ones, except in the highest concentrations. These results show that the conjugation of SLN with the anti-CD64 does not alter their biocompatibility and confirm their potential and promise for biomedical applications, notably in the field of rheumatoid arthritis [125].

4. Conclusion

All the lipid-based nanoscale assemblies reported here were specially designed to allow double incorporation of superparamagnetic nanomaterial (SPION) and a drug. The expected benefit provided by SPION concerns a priori three applications due to their exploitable

superparamagnetic behaviour: (i) the possibility to monitor or control the distribution in the body of the nanocarrier and then theoretically that of the drug by applying a suitable magnetic force, (ii) the triggering of the drug release or (iii) the implementation of a synergistic hyperthermia treatment to conventional chemotherapeutics, the two last applications being practicable on the basis heating effect due to on up-and-down magnetization process under alternative magnetic field. It appears that most of the studies rarely focused on all the three pathways, i.e., on targeted theranostic tools, leaving open the need of further works on this issue.

5. Expert opinion : a focus on co-encapsulation

Different modes of organization of the final hybrid systems were investigated depending on the nature of the lipids and their related hydration behaviour. The crucial building steps of the systems are firstly to adapt the surface-stabilization of the iron oxide nanocrystals to the inner reservoir volume used for their loading and that can be hydrophilic or lipophilic and, secondly, to implement a reliable method of incorporation that should optimize loading rates. The logical consequence concerns the influence of SPION encapsulation on that of the drug and the effectiveness to obtain a constant drug to SPION ratio within the same nano-object. In this respect, let us consider in depth some of the reported observations. The work on folate-coated liposomes by Bothun *et al.* clearly reveals an heterogeneous distribution of the encapsulated hydrophilic SPION among the produced ML, some of them contain no SPION, others contain individual grains or even are filled with SPION clusters [69]. This agrees with independent findings on MFL for which a given vesicle population unequally entraps iron oxide particles [7]. These behaviors mean that the evaluated encapsulation efficiencies reflect an average in iron oxide loading and therefore the presence in each preparation of nano-objects with different responsiveness to magnetic solicitations. To reduce this heterogeneity, magnetic sorting was performed to remove empty or low-loading-rate vesicles from MFL preparations [57], however this procedure has not been used routinely. Regarding other compartmented nanosystems such as cubosomes, the SPION-containing areas are also non-uniformly spread in the inner structure of these assemblies and SPION-free areas are noticed, leading to coexisting magnetic and non-magnetic objects as shown in Figure 3. As a matter of fact, the heterogeneities of the SPION distribution observed in most of the compartmented nanoscale systems likely arises because the incorporation of the iron oxide nanocrystals usually involves a two-step protocol : (i) the introduction of SPION during the mixing of the constituting lipids, optionally beforehand

solubilized in an organic solvent, and the aqueous phase in which they will be allowed to self-organize, (ii) homogenization of the mixture and nanoscale fragmentation. Mainly depending on the slow kinetics of both lipid hydration and solvent diffusivity as well as the limited diffusion rate of colloidal iron oxide due to their size and the viscosity of the medium, the first step presents the intrinsic risk of non-uniform distribution all the more so as the preparations are performed in bulk. Then, since the second step consists in dispersing the system in separate subunits, it necessarily generates a population of nano-objects with different SPION amounts. Beside the simple reflect of non-homogenous distribution of SPION in the initial bulk mixture, it is not excluded that, considering the dimension of the incorporated SPION, the probability to find them in a given nano-object tightly depends on the host compartment volume available in this object, the smaller this volume the lower the trapping probability. This is notably the case of liposome-based systems since extrusion or sonication or even high-pressure shear homogenization lead to small calibrated vesicle structures through successive lipid bilayer breaks and closures. With respect to non-lamellar assemblies such as those issued from bicontinuous cubic phases, it is worth noting that these organizations yield unclosed structures so that the increase in the cumulative interface with the surrounding continuous aqueous phase caused by the fragmentation process, can favour partial SPION release, especially when the iron oxide nanocrystals are coated with hydrophilic stabilizers. On the other side, such repartition would probably induced distribution troubles of the drug even it is not so easy to check than with iron nanoparticles on cryo-TEM pictures. From highly SPION loaded vesicles would result low encapsulation of hydrophilic drug as the available water volume will be reduced. Caricaturally, the most magnetic vesicles won't be efficient to carry drug and vice versa, reducing the interest of the co-encapsulation. It would have sense to explore more carefully the possible competitions between co-encapsulate entities.

In the case of monocompartment systems such as NE or SLN, SPION localization and spreading among the lipid droplets/particles constituting a given preparation have not been precisely examined so far. Nevertheless, it could be anticipated that co-encapsulation is primarily limited in these nanosystems by the own solubility of drug into the lipids in their liquid or solid state, especially when the lipids crystallize in stable polymorphic forms [117,118]. To a certain extend, SPION encapsulation in lipophilic medium could be similarly limited. Except specific defavorable interactions between drug and SPION and below their respective solubility limits in the host lipid phase, it can be reasonably expected a random distribution of inner levels of drug and SPION among the nanoscale droplets or (semi)solid

particles which are produced by mechanical dispersion. Nevertheless, at this stage of conclusions, it will be fully informative to accurately characterize the systems to assess the actual co-encapsulation distribution profile of drug-SPION-loaded NE or SLN.

Although eloquent results have been obviously acquired in the utilization of superparamagnetic lipid-based nanosystems in the field of pharmaceutical or biomedical applications, especially with liposomes (Table 3), some pioneer works have been dedicated to innovative strategies that could optimize the drug-SPION combination. The first group of studies intends to securely link the drug to the iron oxide nanocrystals, by a covalent bond or not. Du *et al.* proposed an original theranostic tool for multi-mechanism therapy of malignant tumors that was based on a tight but non-covalent association of the drug and SPION before their joint encapsulation into liposomes. In this system, the external surface of a C₆₀-fullerene molecule was decorated with magnetite nanoparticles and PEGylated in order to ensure its hydrophilicity and biocompatibility. The anticancer drug docetaxel was then adsorbed onto the nanoparticles referred to as C₆₀-Fe₃O₄-PEG₂₀₀₀ particles and the resulting suspension was loaded into the aqueous core of DPPC-Cholesterol vesicles. The final multi-functional liposomes showed a mean hydrodynamic diameter ~190 nm, a zeta potential of -33.6 ± 2.1 mV as well as a transverse relaxivity value (r_2) = 117 mg.mL⁻¹.s⁻¹ at 3 T. The cytotoxicity and apoptosis study of docetaxel formulations confirmed that radiofrequency could make the multi-functional liposomes remarkably improve the cellular internalization of DDS, release more therapeutic agents into the cytoplasm and achieve a stronger MCF-7 cell apoptosis effect *in vitro*. *In vivo*, the higher drug delivery efficiency to tumors for the multifunctional liposomes/magnet was striking and directly responsible for the higher tumor suppression efficacy in radiofrequency thermal therapy. An obvious darkening effect in the tumor was observed in T₂-weighted MR images of Female C57 mice bearing B16-F10 tumors injected with the multi-functional liposomes with a magnet glued onto the tumor [126]. De Cuypers and his group developed « liposomes » in which individual or aggregated magnetic nanoparticles are stabilized in an aqueous medium by their entrapment in phospholipid bilayers [127]. Hodenius *et al.* reported the binding of 10-hydroxycamptothecin (HCPT) in the coating of such ML. HCPT is a chemotherapeutic anti-cancer agent, mimicking the behavior of a hydrophobic drug molecule. The mean hydrodynamic diameter of these ML was found to be around 91 nm and their ζ -potential is around -32.8 mV. The ML-DPPC/DPPG 1/3 demonstrates the highest HCPT uptake. These ML are extremely suited to carry lipophilic drugs which otherwise are practically insoluble and highly susceptible to fast deterioration in aqueous media [128]. In the same line,

Benyettou *et al.* proposed original ML in which the drug, alendronate, is grafted onto the surface of maghemite ($\gamma\text{-Fe}_2\text{O}_3$) SPION [129]. The obtained DOPC-Cholesterol liposomes have a mean hydrodynamic diameter of 139 ± 15 nm, a ζ potential of -5 ± 3 mV. Final alendronate concentration was 400 μM and iron oxide content was 7.2 mM. Concerning cytotoxicity on three different cell lines (Breast, brain and skin tumors), in the condition used, 100% of alendronate toxicity was obtained only when the drug was grafted on a $\gamma\text{-Fe}_2\text{O}_3$ nanoparticle, itself included in a liposome and with a magnetic field driving force [130]. The co-localization of the SPION and the drug is guaranteed here by the covalent linkage between them.

The second strategy for the improvement of concomitant drug and SPION loading in a single lipid-based nano-object is to encapsulate drug and SPION into separate compartment areas to favor independent optimizations of their respective encapsulation rates. By nature, lipid vesicles and other internally self-assembled lipid particles (ISAsomes) such as cubosomes, are delineated by lipid-based organizations, molecular monolayers or bilayers which entrap a more or less complex network of aqueous domains. It can be then envisaged to incorporate the drug or the iron oxide nanocrystals separately in two distinct inner compartments. However, a limitation of nano-carriers based on mesophases formed by lyotropic lipids is that their supramolecular self-assembly can be modulated by the incorporation of exogenous entities into the supramolecular organization. These would lead to unstable bilayers or curvature troubles into cubosomes [85] that could be aggravated by the particulate state of the SPION. Thus, the association of hydrophobic SPION into liposome bilayers could generate distorsion of the membrane, aggregation or leakage depending on the stabilizer used [131,132]. Interestingly, the incorporation of hydrophilic SPION may cause slight alterations in bilayer fluidity levels even if it does not induce rupture or dramatic damage. Santhosh and al. underlines that this not only the concentration of SPION that affect the structural and thermodynamical properties of the membrane but the sum of factors including the number of SPION interacting with the liposomes, their size, shape or surface charge [133]. Szlezak et al. doped monoolein cubic phase with 0.2 to 2% (w/w) of hydrophilic (citrate) or hydrophobic (OA) SPION [134]. While no significant modification of the phase behavior was observed by adding hydrophobic nanoparticles, substantial changes in the cubic phase parameters and transition temperatures have been observed with hydrophilic SPION. Otherwise, this effect is more pronounced when a drug like DOX is co-incorporated in the formulation. Notably, the lattice parameter increases, resulting in a reduced curvature of the bilayer. At last, release studies from cubic phase gels (similar experiments with cubosomes are not available) clearly show significantly different

DOX release profiles when the hydrophilic SPION is co-incorporate or not into the cubic phase. Furthermore, because of the imbrication of both compartments, the destabilization of one of them would destabilize the other one.

To our opinion, the next step in this field of lipid-based systems co-encapsulating SPION and drug is to imagine carriers in which (1)- the encapsulation of one compound do not alter the encapsulation of the other one and (2)- the interconnexion between the two compartments is as low as possible to minimize the risk of destabilization of the nanoobject when acting on them. Anisotropic structures with one compartment devoted to the incorporation of the SPION and another one for the drug would fill this description [135–137].

Financial and competing interests disclosure

The authors report no conflict of interest.

References

- [1] Massart R. Preparation of aqueous magnetic liquids in alkaline and acidic media. *IEEE Trans. Magn.* 1981;17:1247–1248.
- [2] Gupta AK, Gupta M. Synthesis and surface engineering of iron oxide nanoparticles for biomedical applications. *Biomaterials.* 2005;26:3995–4021.
- [3] Kostopoulou A, Lappas A. Colloidal magnetic nanocrystal clusters: variable length-scale interaction mechanisms, synergetic functionalities and technological advantages. *Nanotechnol. Rev.* 2015;4.
- [4] Belin T, Guigue-Millot N, Caillot T, et al. Influence of Grain Size, Oxygen Stoichiometry, and Synthesis Conditions on the γ -Fe₂O₃ Vacancies Ordering and Lattice Parameters. *J. Solid State Chem.* 2002;163:459–465.
- [5] Gossuin Y, Gillis P, Hocq A, et al. Magnetic resonance relaxation properties of superparamagnetic particles. *Wiley Interdiscip. Rev. Nanomed. Nanobiotechnol.* 2009;1:299–310.
- [6] Shtykova EV, Huang X, Remmes N, et al. Structure and Properties of Iron Oxide Nanoparticles Encapsulated by Phospholipids with Poly(ethylene glycol) Tails. *J. Phys. Chem. C.* 2007;111:18078–18086.
- [7] Marie H, Plassat V, Lesieur S. Magnetic-fluid-loaded liposomes for MR imaging and therapy of cancer. *J. Drug Deliv. Sci. Technol.* 2013;23:25–37.
- [8] Bourrinet P, Bengéle HH, Bonnemain B, et al. Preclinical safety and pharmacokinetic profile of ferumoxtran-10, an ultrasmall superparamagnetic iron oxide magnetic resonance contrast agent. *Invest. Radiol.* 2006;41:313–324.
- [9] W L. Ferumoxtran-10 Advanced Magnetics. *IDrugs Investig. Drugs J.* 2003;6:987–993.
- [10] Bonnemain B. Superparamagnetic Agents in Magnetic Resonance Imaging: Physicochemical Characteristics and Clinical Applications A Review. *J. Drug Target.* 1998;6:167–174.

- [11] Reddy LH, Arias JL, Nicolas J, et al. Magnetic Nanoparticles: Design and Characterization, Toxicity and Biocompatibility, Pharmaceutical and Biomedical Applications. *Chem. Rev.* 2012;112:5818–5878.
- [12] Choi HS, Liu W, Misra P, et al. Renal Clearance of Nanoparticles. *Nat. Biotechnol.* 2007;25:1165–1170.
- [13] Veisheh O, Gunn JW, Zhang M. Design and fabrication of magnetic nanoparticles for targeted drug delivery and imaging. *Adv. Drug Deliv. Rev.* 2010;62:284–304.
- [14] Tanimoto A, Kuribayashi S. Application of superparamagnetic iron oxide to imaging of hepatocellular carcinoma. *Eur. J. Radiol.* 2006;58:200–216.
- [15] Moghimi SM. Mechanisms of splenic clearance of blood cells and particles: towards development of new splenotropic agents. *Adv. Drug Deliv. Rev.* 1995;17:103–115.
- [16] Roberts WG, Palade GE. Neovasculature Induced by Vascular Endothelial Growth Factor Is Fenestrated. *Cancer Res.* 1997;57:765–772.
- [17] Matsumura Y, Maeda H. A New Concept for Macromolecular Therapeutics in Cancer Chemotherapy: Mechanism of Tumor-tropic Accumulation of Proteins and the Antitumor Agent Smancs. *Cancer Res.* 1986;46:6387–6392.
- [18] Passirani C, Barratt G, Devissaguet J-P, et al. Long-Circulating Nanoparticles Bearing Heparin or Dextran Covalently Bound to Poly(Methyl Methacrylate). *Pharm. Res.* 1998;15:1046–1050.
- [19] Anzai Y, Piccoli CW, Outwater EK, et al. Evaluation of Neck and Body Metastases to Nodes with Ferumoxtran 10-enhanced MR Imaging: Phase III Safety and Efficacy Study. *Radiology.* 2003;228:777–788.
- [20] Chambon C, Clement O, Le Blanche A, et al. Superparamagnetic iron oxides as positive MR contrast agents: in vitro and in vivo evidence. *Magn. Reson. Imaging.* 1993;11:509–519.

- [21] Canet E, Revel D, Forrat R, et al. Superparamagnetic iron oxide particles and positive enhancement for myocardial perfusion studies assessed by subsecond T1-weighted MRI. *Magn. Reson. Imaging*. 1993;11:1139–1145.
- [22] Laurent S, Dutz S, Häfeli UO, et al. Magnetic fluid hyperthermia: Focus on superparamagnetic iron oxide nanoparticles. *Adv. Colloid Interface Sci*. 2011;166:8–23.
- [23] Qin J, Laurent S, Jo YS, et al. A High-Performance Magnetic Resonance Imaging T2 Contrast Agent. *Adv. Mater*. 2007;19:1874–1878.
- [24] Rohrer M, Bauer H, Mintorovitch J, et al. Comparison of magnetic properties of MRI contrast media solutions at different magnetic field strengths. *Invest. Radiol*. 2005;40:715–724.
- [25] Xiao L, Li J, Brougham DF, et al. Water-Soluble Superparamagnetic Magnetite Nanoparticles with Biocompatible Coating for Enhanced Magnetic Resonance Imaging. *ACS Nano*. 2011;5:6315–6324.
- [26] Zhang K, Liang Q, Ma S, et al. On-chip manipulation of continuous picoliter-volume superparamagnetic droplets using a magnetic force. *Lab. Chip*. 2009;9:2992.
- [27] Bacri J-C, Perzynski R, Salin D, et al. Magnetic colloidal properties of ionic ferrofluids. *J. Magn. Magn. Mater*. 1986;62:36–46.
- [28] Tan MC. Nanostructured materials for biomedical applications. Kerala: Transworld research network; 2009.
- [29] Voit W, Kim DK, Zapka W, et al. Magnetic behavior of coated superparamagnetic iron oxide nanoparticles in ferrofluids. *MRS Online Proc. Libr. Arch*. 2001;676.
- [30] Yang J, Lee H, Hyung W, et al. Magnetic PECA nanoparticles as drug carriers for targeted delivery: Synthesis and release characteristics. *J. Microencapsul*. 2006;23:203–212.
- [31] Huang Y, Mao K, Zhang B, et al. Superparamagnetic iron oxide nanoparticles conjugated with folic acid for dual target-specific drug delivery and MRI in cancer theranostics. *Mater. Sci. Eng. C*. 2017;70, Part 1:763–771.

- [32] Kim D-H, Lee S-H, Kim K-N, et al. Temperature change of various ferrite particles with alternating magnetic field for hyperthermic application. *J. Magn. Magn. Mater.* 2005;293:320–327.
- [33] Wang X, Gu H, Yang Z. The heating effect of magnetic fluids in an alternating magnetic field. *J. Magn. Magn. Mater.* 2005;293:334–340.
- [34] Shellman YG, Howe WR, Miller LA, et al. Hyperthermia Induces Endoplasmic Reticulum-Mediated Apoptosis in Melanoma and Non-Melanoma Skin Cancer Cells. *J. Invest. Dermatol.* 2008;128:949–956.
- [35] Hildebrandt B, Wust P, Ahlers O, et al. The cellular and molecular basis of hyperthermia. *Crit. Rev. Oncol. Hematol.* 2002;43:33–56.
- [36] Wust P, Hildebrandt B, Sreenivasa G, et al. Hyperthermia in combined treatment of cancer. *Lancet Oncol.* 2002;3:487–497.
- [37] Brusentsov NA, Brusentsova TN, Sergeev AV, et al. Ferrimagnetic fluids and ferro-and ferrimagnetic suspensions for the RF-induction hyperthermia of tumors. *Pharm. Chem. J.* 2000;34:201–207.
- [38] Matsuoka F, Shinkai M, Honda H, et al. Hyperthermia using magnetite cationic liposomes for hamster osteosarcoma. *Biomagn. Res. Technol.* 2004;2:1.
- [39] Kikumori T, Kobayashi T, Sawaki M, et al. Anti-cancer effect of hyperthermia on breast cancer by magnetite nanoparticle-loaded anti-HER2 immunoliposomes. *Breast Cancer Res. Treat.* 2009;113:435.
- [40] Same S, Aghanejad A, Akbari Nakhjavani S, et al. Radiolabeled theranostics: magnetic and gold nanoparticles. *Bioimpacts.* 2016;6:169–181.
- [41] Kievit FM, Zhang M. Surface Engineering of Iron Oxide Nanoparticles for Targeted Cancer Therapy. *Acc. Chem. Res.* 2011;44:853–862.
- [42] Thomas R, Park I-K, Jeong Y. Magnetic Iron Oxide Nanoparticles for Multimodal Imaging and Therapy of Cancer. *Int. J. Mol. Sci.* 2013;14:15910–15930.

- [43] Laurent S, Saei AA, Behzadi S, et al. Superparamagnetic iron oxide nanoparticles for delivery of therapeutic agents: opportunities and challenges. *Expert Opin. Drug Deliv.* 2014;11:1449–1470.
- [44] Bangham AD, Standish MM, Watkins JC. Diffusion of univalent ions across the lamellae of swollen phospholipids. *J. Mol. Biol.* 1965;13:238-IN27.
- [45] Li G, Zhou Z, Li Y, et al. Surface functionalization of chitosan-coated magnetic nanoparticles for covalent immobilization of yeast alcohol dehydrogenase from *Saccharomyces cerevisiae*. *J. Magn. Mater.* 2010;322:3862–3868.
- [46] Zhang Y, Liu J-Y, Ma S, et al. Synthesis of PVP-coated ultra-small Fe₃O₄ nanoparticles as a MRI contrast agent. *J. Mater. Sci. Mater. Med.* 2010;21:1205–1210.
- [47] Harisinghani M, Ross RW, Guimaraes AR, et al. Utility of a New Bolus-injectable Nanoparticle for Clinical Cancer Staging. *Neoplasia.* 2007;9:1160–1165.
- [48] Mahmoudi M, Simchi A, Imani M, et al. Optimal Design and Characterization of Superparamagnetic Iron Oxide Nanoparticles Coated with Polyvinyl Alcohol for Targeted Delivery and Imaging †. *J. Phys. Chem. B.* 2008;112:14470–14481.
- [49] Carvalho A, Martins MBF, Corvo ML, et al. Enhanced contrast efficiency in MRI by PEGylated magnetoliposomes loaded with PEGylated SPION: Effect of SPION coating and micro-environment. *Mater. Sci. Eng. C.* 2014;43:521–526.
- [50] Ma H, Qi X, Maitani Y, et al. Preparation and characterization of superparamagnetic iron oxide nanoparticles stabilized by alginate. *Int. J. Pharm.* 2007;333:177–186.
- [51] Fattahi H, Laurent S, Liu F, et al. Magnetoliposomes as multimodal contrast agents for molecular imaging and cancer nanotheragnostics. *Nanomed.* 2011;6:529–544.
- [52] Monnier CA, Burnand D, Rothen-Rutishauser B, et al. Magnetoliposomes: opportunities and challenges. *Eur. J. Nanomedicine.* 2014;6.
- [53] Soenen SJ, Velde GV, Ketkar-Atre A, et al. Magnetoliposomes as magnetic resonance imaging contrast agents. *Wiley Interdiscip. Rev. Nanomed. Nanobiotechnol.* 2011;3:197–211.

- [54] Ji B, Wang M, Gao D, et al. Combining nanoscale magnetic nimodipine liposomes with magnetic resonance image for Parkinson's disease targeting therapy. *Nanomed.* 2017;12:237–253.
- [55] Martina M-S, Fortin J-P, Ménager C, et al. Generation of Superparamagnetic Liposomes Revealed as Highly Efficient MRI Contrast Agents for in Vivo Imaging. *J. Am. Chem. Soc.* 2005;127:10676–10685.
- [56] Plassat V, Martina MS, Barratt G, et al. Sterically stabilized superparamagnetic liposomes for MR imaging and cancer therapy: Pharmacokinetics and biodistribution. *Int. J. Pharm.* 2007;344:118–127.
- [57] Marie H, Lemaire L, Franconi F, et al. Superparamagnetic Liposomes for MRI Monitoring and External Magnetic Field-Induced Selective Targeting of Malignant Brain Tumors. *Adv. Funct. Mater.* 2015;25:1258–1269.
- [58] Plassat V, Wilhelm C, Marsaud V, et al. Anti-Estrogen-Loaded Superparamagnetic Liposomes for Intracellular Magnetic Targeting and Treatment of Breast Cancer Tumors. *Adv. Funct. Mater.* 2011;21:83–92.
- [59] Ye H, Tong J, Liu J, et al. Gemcitabine Oxaliplatin. *Oncotarget.* 2016;7:43762–43778.
- [60] Viroonchatapan E, Sato H, Ueno M, et al. Release of 5-fluorouracil from thermosensitive magnetoliposomes induced by an electromagnetic field. *J. Controlled Release.* 1997;46:263–271.
- [61] Yoshida M, Watanabe Y, Sato M, et al. Feasibility of chemohyperthermia with docetaxel-embedded magnetoliposomes as minimally invasive local treatment for cancer. *Int. J. Cancer.* 2010;126:1955–1965.
- [62] Yoshida M, Sato M, Yamamoto Y, et al. *J. Gastroenterol. Hepatol.* 2012;27:406–411.
- [63] Bolfarini GC, Siqueira-Moura MP, Demets GJF, et al. In vitro evaluation of combined hyperthermia and photodynamic effects using magnetoliposomes loaded with cucurbit[7]uril zinc phthalocyanine complex on melanoma. *J. Photochem. Photobiol. B.* 2012;115:1–4.

- [64] Di Corato R, Béalle G, Kolosnjaj-Tabi J, et al. Combining Magnetic Hyperthermia and Photodynamic Therapy for Tumor Ablation with Photoresponsive Magnetic Liposomes. *ACS Nano*. 2015;9:2904–2916.
- [65] Ferreira RV, Martins TM da M, Goes AM, et al. Thermosensitive gemcitabine-magnetoliposomes for combined hyperthermia and chemotherapy. *Nanotechnology*. 2016;27:085105.
- [66] Kulshrestha P, Gogoi M, Bahadur D, et al. In vitro application of paclitaxel loaded magnetoliposomes for combined chemotherapy and hyperthermia. *Colloids Surf. B Biointerfaces*. 2012;96:1–7.
- [67] Clares B, Biedma-Ortiz RA, Sáez-Fernández E, et al. Nano-engineering of 5-fluorouracil-loaded magnetoliposomes for combined hyperthermia and chemotherapy against colon cancer. *Eur. J. Pharm. Biopharm*. 2013;85:329–338.
- [68] Chen Y, Chen Y, Xiao D, et al. Low-dose chemotherapy of hepatocellular carcinoma through triggered-release from bilayer-decorated magnetoliposomes. *Colloids Surf. B Biointerfaces*. 2014;116:452–458.
- [69] Bothun GD, Lelis A, Chen Y, et al. Multicomponent folate-targeted magnetoliposomes: design, characterization, and cellular uptake. *Nanomedicine Nanotechnol. Biol. Med*. 2011;7:797–805.
- [70] Sharma S, Rasool HI, Palanisamy V, et al. Structural-Mechanical Characterization of Nanoparticle Exosomes in Human Saliva, Using Correlative AFM, FESEM, and Force Spectroscopy. *ACS Nano*. 2010;4:1921–1926.
- [71] Ha D, Yang N, Nadithe V. Exosomes as therapeutic drug carriers and delivery vehicles across biological membranes: current perspectives and future challenges. *Acta Pharm. Sin. B*. 2016;6:287–296.
- [72] Sun D, Zhuang X, Zhang S, et al. Exosomes are endogenous nanoparticles that can deliver biological information between cells. *Adv. Drug Deliv. Rev*. 2013;65:342–347.
- [73] Hood JL, Scott MJ, Wickline SA. Maximizing exosome colloidal stability following electroporation. *Anal. Biochem*. 2014;448:41–49.

- [74] Hu L, Wickline SA, Hood JL. Magnetic resonance imaging of melanoma exosomes in lymph nodes. *Magn. Reson. Med.* 2015;74:266–271.
- [75] Chung T-H, Hsiao J-K, Yao M, et al. Ferucarbotran, a carboxydextran-coated superparamagnetic iron oxide nanoparticle, induces endosomal recycling, contributing to cellular and exosomal EGFR overexpression for cancer therapy. *RSC Adv.* 2015;5:89932–89939.
- [76] Silva AKA, Luciani N, Gazeau F, et al. Combining magnetic nanoparticles with cell derived microvesicles for drug loading and targeting. *Nanomedicine Nanotechnol. Biol. Med.* 2015;11:645–655.
- [77] Qi H, Liu C, Long L, et al. Blood Exosomes Endowed with Magnetic and Targeting Properties for Cancer Therapy. *ACS Nano.* 2016;10:3323–3333.
- [78] Piffoux M, Silva AKA, Lugagne J-B, et al. Extracellular Vesicle Production Loaded with Nanoparticles and Drugs in a Trade-off between Loading, Yield and Purity: Towards a Personalized Drug Delivery System. *Adv. Biosyst.* 2017;1:1700044.
- [79] Stroem P, Anderson DM. The cubic phase region in the system didodecyldimethylammonium bromide-water-styrene. *Langmuir.* 1992;8:691–709.
- [80] Lynch ML, Kochvar KA, Burns JL, et al. Aqueous-Phase Behavior and Cubic Phase-Containing Emulsions in the C₁₂E₂-Water System. *Langmuir.* 2000;16:3537–3542.
- [81] Nanjwade BK, Hundekar YR, Kamble MS, et al. Development of Cuboidal Nanomedicine by Nanotechnology. *Austin J Nanomed Nanotechnol.* 2014;2:1023.
- [82] Garg G, Saraf S, Saraf S. Cubosomes: an overview. *Biol. Pharm. Bull.* 2007;30:350–353.
- [83] Drummond CJ, Fong C. Surfactant self-assembly objects as novel drug delivery vehicles. *Curr. Opin. Colloid Interface Sci.* 1999;4:449–456.
- [84] Acharya DP, Moffat BA, Polyzos A, et al. Cubic mesophase nanoparticles doped with superparamagnetic iron oxide nanoparticles: a new class of MRI contrast agent. *RSC Adv.* 2012;2:6655–6662.

- [85] Montis C, Castroflorio B, Mendoza M, et al. Magnetocubosomes for the delivery and controlled release of therapeutics. *J. Colloid Interface Sci.* 2015;449:317–326.
- [86] Hong SK, Ma JY, Kim J-C. Preparation of iron oxide nanoparticles within monoolein cubic phase. *J. Ind. Eng. Chem.* 2012;18:1977–1982.
- [87] Wang MH, Kim J-C. Magnetic field-responsive cubosomes containing magnetite and poly(N-isopropylacrylamide). *J. Controlled Release.* 2013;172:e139.
- [88] Gupta A, Eral HB, Hatton TA, et al. Nanoemulsions: formation, properties and applications. *Soft Matter.* 2016;12:2826–2841.
- [89] Singh Y, Meher JG, Raval K, et al. Nanoemulsion: Concepts, development and applications in drug delivery. *J. Controlled Release.* 2017;252:28–49.
- [90] Bates TR, Carrigan PJ. Apparent absorption kinetics of micronized griseofulvin after its oral administration on single- and multiple-dose regimens to rats as a corn oil-in-water emulsion and aqueous suspension. *J. Pharm. Sci.* 1975;64:1475–1481.
- [91] Sainsbury F, Zeng B, Middelberg AP. Towards designer nanoemulsions for precision delivery of therapeutics. *Curr. Opin. Chem. Eng.* 2014;4:11–17.
- [92] Ganta S, Amiji M. Coadministration of Paclitaxel and Curcumin in Nanoemulsion Formulations To Overcome Multidrug Resistance in Tumor Cells. *Mol. Pharm.* 2009;6:928–939.
- [93] Kretzer IF, Maria DA, Maranhão RC. Drug-targeting in combined cancer chemotherapy: tumor growth inhibition in mice by association of paclitaxel and etoposide with a cholesterol-rich nanoemulsion. *Cell. Oncol.* 2012;35:451–460.
- [94] Chuan YP, Zeng BY, O’Sullivan B, et al. Co-delivery of antigen and a lipophilic anti-inflammatory drug to cells via a tailorable nanocarrier emulsion. *J. Colloid Interface Sci.* 2012;368:616–624.
- [95] Song Y-C, Cheng H-Y, Leng C-H, et al. A novel emulsion-type adjuvant containing CpG oligodeoxynucleotides enhances CD8⁺ T-cell-mediated anti-tumor immunity. *J. Controlled Release.* 2014;173:158–165.

- [96] Sadurní N, Solans C, Azemar N, et al. Studies on the formation of O/W nano-emulsions, by low-energy emulsification methods, suitable for pharmaceutical applications. *Eur. J. Pharm. Sci.* 2005;26:438–445.
- [97] Lan Q, Liu C, Yang F, et al. Synthesis of bilayer oleic acid-coated Fe₃O₄ nanoparticles and their application in pH-responsive Pickering emulsions. *J. Colloid Interface Sci.* 2007;310:260–269.
- [98] Bloemen M, Brullot W, Luong TT, et al. Improved functionalization of oleic acid-coated iron oxide nanoparticles for biomedical applications. *J. Nanoparticle Res.* 2012;14:1–10.
- [99] Zhang L, He R, Gu H-C. Oleic acid coating on the monodisperse magnetite nanoparticles. *Appl. Surf. Sci.* 2006;253:2611–2617.
- [100] Ramella D, Polito L, Mazzini S, et al. A Strategy for Multivalent Presentation of Carba Analogues from *N. meningitidis* A Capsular Polysaccharide. *Eur. J. Org. Chem.* 2014;2014:5915–5924.
- [101] Lartigue L, Oumzil K, Guari Y, et al. Water-Soluble Rhamnose-Coated Fe₃O₄ Nanoparticles. *Org. Lett.* 2009;11:2992–2995.
- [102] Lu C, Bhatt LR, Jun HY, et al. Carboxyl–polyethylene glycol–phosphoric acid: a ligand for highly stabilized iron oxide nanoparticles. *J. Mater. Chem.* 2012;22:19806.
- [103] White MA, Johnson JA, Koberstein JT, et al. Toward the Syntheses of Universal Ligands for Metal Oxide Surfaces: Controlling Surface Functionality through Click Chemistry. *J. Am. Chem. Soc.* 2006;128:11356–11357.
- [104] Liang S, Wang Y, Yu J, et al. Surface modified superparamagnetic iron oxide nanoparticles: as a new carrier for bio-magnetically targeted therapy. *J. Mater. Sci. Mater. Med.* 2007;18:2297–2302.
- [105] Koh I, Wang X, Varughese B, et al. Magnetic Iron Oxide Nanoparticles for Biorecognition: Evaluation of Surface Coverage and Activity. *J. Phys. Chem. B.* 2006;110:1553–1558.

- [106] Zhang C, Wängler B, Morgenstern B, et al. Silica- and Alkoxysilane-Coated Ultrasmall Superparamagnetic Iron Oxide Particles: A Promising Tool To Label Cells for Magnetic Resonance Imaging. *Langmuir*. 2007;23:1427–1434.
- [107] Alwi R, Telenkov S, Mandelis A, et al. Silica-coated super paramagnetic iron oxide nanoparticles (SPION) as biocompatible contrast agent in biomedical photoacoustics. *Biomed. Opt. Express*. 2012;3:2500–2509.
- [108] Jarzyna PA, Skajaa T, Gianella A, et al. Iron oxide core oil-in-water emulsions as a multifunctional nanoparticle platform for tumor targeting and imaging. *Biomaterials*. 2009;30:6947–6954.
- [109] Gianella A, Jarzyna PA, Mani V, et al. Multifunctional Nanoemulsion Platform for Imaging Guided Therapy Evaluated in Experimental Cancer. *ACS Nano*. 2011;5:4422–4433.
- [110] Deddens LH, Jarzyna PA, Griffioen AW, et al. RGD-Functionalized Superparamagnetic Nanoemulsions for Target-Specific Imaging of Tumor Angiogenesis. *Proc Intl Soc Mag Reson Med*. 2010;18:3749.
- [111] Manjunath K, Venkateswarlu V. Pharmacokinetics, tissue distribution and bioavailability of clozapine solid lipid nanoparticles after intravenous and intraduodenal administration. *J. Controlled Release*. 2005;107:215–228.
- [112] Varshosaz J, Tabbakhian M, Mohammadi MY. Formulation and optimization of solid lipid nanoparticles of buspirone HCl for enhancement of its oral bioavailability. *J. Liposome Res*. 2010;20:286–296.
- [113] Sarmiento B, Martins S, Ferreira D, et al. Oral insulin delivery by means of solid lipid nanoparticles. *Int. J. Nanomedicine*. 2007;2:743.
- [114] Yang R, Gao R, Li F, et al. The influence of lipid characteristics on the formation, in vitro release, and in vivo absorption of protein-loaded SLN prepared by the double emulsion process. *Drug Dev. Ind. Pharm*. 2011;37:139–148.
- [115] Luo Y, Chen D, Ren L, et al. Solid lipid nanoparticles for enhancing vinpocetine's oral bioavailability. *J. Controlled Release*. 2006;114:53–59.

- [116] Chen C-C, Tsai T-H, Huang Z-R, et al. Effects of lipophilic emulsifiers on the oral administration of lovastatin from nanostructured lipid carriers: Physicochemical characterization and pharmacokinetics. *Eur. J. Pharm. Biopharm.* 2010;74:474–482.
- [117] Müller RH, Runge SA, Ravelli V, et al. Cyclosporine-loaded solid lipid nanoparticles (SLN®): Drug–lipid physicochemical interactions and characterization of drug incorporation. *Eur. J. Pharm. Biopharm.* 2008;68:535–544.
- [118] Müller RH, Maaßen S, Weyhers H, et al. Cytotoxicity of magnetite-loaded polylactide, polylactide/glycolide particles and solid lipid nanoparticles. *Int. J. Pharm.* 1996;138:85–94.
- [119] Grillone A, Riva ER, Mondini A, et al. Active Targeting of Sorafenib: Preparation, Characterization, and In Vitro Testing of Drug-Loaded Magnetic Solid Lipid Nanoparticles. *Adv. Healthc. Mater.* 2015;4:1681–1690.
- [120] Zhao S, Zhang Y, Han Y, et al. Preparation and Characterization of Cisplatin Magnetic Solid Lipid Nanoparticles (MSLNs): Effects of Loading Procedures of Fe₃O₄ Nanoparticles. *Pharm. Res.* 2014;32:482–491.
- [121] Oumzil K, Ramin MA, Lorenzato C, et al. Solid Lipid Nanoparticles for Image-Guided Therapy of Atherosclerosis. *Bioconjug. Chem.* 2016;27:569–575.
- [122] Pang X, Cui F, Tian J, et al. Preparation and characterization of magnetic solid lipid nanoparticles loaded with ibuprofen. *Asian J Pharm Sci.* 2009;4:132–137.
- [123] Ying X-Y, Du Y-Z, Hong L-H, et al. Magnetic lipid nanoparticles loading doxorubicin for intracellular delivery: Preparation and characteristics. *J. Magn. Magn. Mater.* 2011;323:1088–1093.
- [124] Hsu M-H, Su Y-C. Iron-oxide embedded solid lipid nanoparticles for magnetically controlled heating and drug delivery. *Biomed. Microdevices.* 2008;10:785–793.
- [125] Albuquerque J, Moura C, Sarmiento B, et al. Solid Lipid Nanoparticles: A Potential Multifunctional Approach towards Rheumatoid Arthritis Theranostics. *Molecules.* 2015;20:11103–11118.

- [126] Du B, Han S, Li H, et al. Multi-functional liposomes showing radiofrequency-triggered release and magnetic resonance imaging for tumor multi-mechanism therapy. *Nanoscale*. 2015;7:5411–5426.
- [127] De Cuyper M, Joniau M. Magnetoliposomes. *Eur. Biophys. J.* 1988;15:311–319.
- [128] Hodenius MAJ, Schmitz-Rode T, Baumann M, et al. Absorption of 10-hydroxycamptothecin into the coat of magnetoliposomes. *Colloids Surf. Physicochem. Eng. Asp.* 2009;343:20–23.
- [129] Benyettou F, Guenin E, Lalatonne Y, et al. Microwave assisted nanoparticle surface functionalization. *Nanotechnology*. 2011;22:055102.
- [130] Benyettou F, Chebbi I, Motte L, et al. Magnetoliposome for alendronate delivery. *J. Mater. Chem.* 2011;21:4813–4820.
- [131] Amstad E, Kohlbrecher J, Müller E, et al. Triggered Release from Liposomes through Magnetic Actuation of Iron Oxide Nanoparticle Containing Membranes. *Nano Lett.* 2011;11:1664–1670.
- [132] Chen Y, Bose A, Bothun GD. Controlled Release from Bilayer-Decorated Magnetoliposomes via Electromagnetic Heating. *ACS Nano*. 2010;4:3215–3221.
- [133] Budime Santhosh P, Drasler B, Drobne D, et al. Effect of superparamagnetic iron oxide nanoparticles on fluidity and phase transition of phosphatidylcholine liposomal membranes. *Int. J. Nanomedicine*. 2015;6089.
- [134] Szlezak M, Nieciecka D, Joniec A, et al. Monoolein Cubic Phase Gels and Cubosomes Doped with Magnetic Nanoparticles–Hybrid Materials for Controlled Drug Release. *ACS Appl. Mater. Interfaces*. 2017;9:2796–2805.
- [135] Tran L-T-C, Lesieur S, Faivre V. Janus nanoparticles: materials, preparation and recent advances in drug delivery. *Expert Opin. Drug Deliv.* 2014;11:1061–1074.
- [136] Bonnaud C, Monnier CA, Demurtas D, et al. Insertion of Nanoparticle Clusters into Vesicle Bilayers. *ACS Nano*. 2014;8:3451–3460.

[137] Walther A, Müller AHE. Janus Particles: Synthesis, Self-Assembly, Physical Properties, and Applications. *Chem. Rev.* 2013;113:5194–5261.

Highlights box

- Superparamagnetic iron oxide nanoparticles (SPION) can be utilized for magnetic resonance imaging, physical targeting, hyperthermia and/or temperature-triggered drug release.
- Depending on their physico-chemical properties, lipid-based excipients are able to generate monophasic or compartmented nanoscale assemblies that allow double incorporation of superparamagnetic nanomaterials and drugs.
- This review highlights the potential applications of magnetic-fluid-loaded lipid nanocarriers as multifunctional systems.
- Discussion has been focused on the co-encapsulation limits and the strategies to guarantee the drug-to-SPION ratio.

EXPERIMENTAL PART

Chapter 1 : SCALABLE PROCESS TO PRODUCE LIPID-BASED INNOVATIVE COMPARTMENTED JANUS NANOPARTICLES WITH PHARMACEUTICALLY APPROVED EXCIPIENTS	79
Chapter 2 : INCORPORATION OF HYDROPHILIC FERRO-FLUIDS INTO LIPID-BASED JANUS NANOPARTICLES.....	100
Chapter 3 : INCORPORATION OF HYDROPHOBIC FERRO-FLUIDS INTO LIPID-BASED JANUS NANOPARTICLES	131

SCALABLE PROCESS TO PRODUCE LIPID-BASED INNOVATIVE COMPARTMENTED JANUS NANOPARTICLES WITH PHARMACEUTICALLY APPROVED EXCIPIENTS

Tri TRUONG-CONG ^{1a}, Elodie MILLART ^{1a}, Chau Tran Le TUYET ¹,
Heinz AMENITSCH ², Ghislaine FREBOURG ³, Sylviane LESIEUR ¹, Vincent FAIVRE ^{1*}

¹ Institut Galien Paris-Sud, Université Paris-Saclay, Univ. Paris-Sud, Labex LERMIT,
5 rue Jean-Baptiste Clément, Châtenay-Malabry 92296, France.

² Institute of Inorganic Chemistry, Graz University of Technology,
Stremayergasse 9/IV, 8010 Graz.

³ Institut de Biologie Paris-Seine (IBPS) FR 3631 Université Pierre et Marie Curie-CNRS,
9 quai St Bernard 75252 Paris cedex 05, France

^a equivalent contributions

* Corresponding author

Tel.: +33 146835465; Fax: +33 146835312.

E-mail address: vincent.favre@u-psud.fr (Vincent FAIVRE).

Submitted to *Nanoletters* on September 28th, 2017

Abstract

In the field of nanotechnologies, theranostic approaches and FDC products require the development of innovative carriers able to co-encapsulate several entities of interest. This letter describes the preparation and characterization of lipid-based *Janus* compartmented nanoparticles. They were successfully prepared using a scalable process with pharmaceutically approved excipients. Analysis of microscopic structure and supramolecular organization demonstrated the formation of two physico-chemical different compartments enabling to co-administrate at once both, liposoluble and hydrosoluble active pharmaceutical ingredients.

Keywords : Compartmented lipid nanoparticles, *Janus* lipid nanoparticles, high pressure homogenization, cryo-transmission electron microscopy, small-angle x-ray diffraction. stearyl macroglycerides, soybean lecithin, linoleoyl polyoxylglycerides, oleoyl polyoxylglycerides

1. Introduction

“Let me quote still another new animal: the *Janus* grains” During its Nobel prize lecture, de Gennes¹ mentioned original particles which have attracted attention because of their fascinating properties and promising applications in solar cells, electronic devices, security labeling, medical diagnostics and therapeutics, etc. Whereas the terminology « *Janus* particles » was coined in the early 1990s, the fundamental research is still being conducted to improve the understanding of these fascinating particles on their properties, geometry, synthetic approach, and applications. In the field of drug delivery, mainly four types of application have been addressed with *Janus* nanoparticles: encapsulation of active pharmaceutical ingredients (API) which have widely disparate solubility or charge, dual-phase release kinetics, drug targeting, and theranostic².

The name “*Janus*” comes from an ancient Roman God, who is depicted with a double-faced head which peers to the past and the future, to forward and back, to creation and destruction. The term *Janus* particles was used to describe particles which are the combination of two distinct sides. At a macroscopic level, mainly two kinds of *Janus* particles can be described : patchy and compartmented *Janus* particles. Patchy particles are defined as particles with precisely controlled patches of varying surface while compartmented particles are defined as structures which are composed of multiple phase-separated domains in the core. Strictly speaking, *Janus* particles have a 50:50 distinct coverage in shape, composition, chemistry, polarity or other property of interest³.

Nowadays, many techniques have been developed to fabricate *Janus* particles. In general, they can be divided into three main methods: masking, bottom-up assemblies and controlled phase separation. They can be made from polymers, lipids, organic to inorganic and metallic materials; depending on the synthesis strategies. Walther and Müller⁴ gave an impressive overview of these different materials.

Bottom-up assemblies and phase separation methods are the best approaches to produce compartmented *Janus* particles with sufficiently high yield. However, the interfacial and bulk properties generally result from the synthesis of specific di- or tri-block copolymers or dendrimers, which are often not recognized as safe (GRAS status) by the FDA and are not approved by useful Pharmacopoeia (US, Eur., Jap.). Recent progresses in polymer click chemistry allow the synthesis of very complex and amazing macromolecules, but their

validation by pharmaceutical authorities is difficult to implement and their high throughput production and purification are complicated.

The aim of the present work was to investigate the possibility to produce *Janus* nanoparticles only with marketed and pharmaceutically approved lipid-based excipients and with a scalable process. Several lipid phases have been combined into the formulations. The nanoparticles have been characterized from their long-term physical stability such as size, zeta potential, microscopic structure and supramolecular organization. A formation mechanism has been proposed too.

2. Materials and Methods

2.1. Materials

Labrafac[®] CC (caprylic-capric triglycerides), Gelucire[®] 50/13 (stearoyl macroglycerides; mixture of monoesters, diesters and triesters of glycerol (~20 wt%) and monoesters and diesters of polyethylene glycols (~80 wt%) with mean molecular mass of 1500; mainly contains esters of stearic acid), Labrafil[®] M 2125 CS (linoleoyl polyoxyglycerides; mixture of monoesters, diesters and triesters of glycerol (>60 wt%) and monoesters and diesters of polyethylene glycols (<40 wt%) with mean molecular mass of 300; mainly contains esters of linoleic acid), and Labrafil[®] M1944 CS (oleoyl polyoxyglycerides; mixture of monoesters, diesters and triesters of glycerol (>60 wt%) and monoesters and diesters of polyethylene glycols (<40 wt%) with mean molecular mass of 300; mainly contains esters of OA) were given by Gattefosse S.A.S. (Saint-Priest, France). Phospholipon[®] 90G (soybean lecithin at 94 – 102% of phosphatidylcholine) was provided by Phospholipid GmbH, Lipoid Group (Köln, Germany). Water was purified through a Milli-Q water system (Millipore, France).

2.2. Methods

2.2.1. Preparation of nanodispersions by high-pressure homogenization process

Formulation studies on 10g of total dispersion

7.7 ml of pre-heated (60°C) aqueous phase containing 2% (w/w) of stearoyl macroglycerides (Gelucire[®] 50/13) and 1% (w/w) of soybean lecithin (Phospholipon[®] 90G) as surfactant was formed by using ultra-turrax (IKA[®] T10 basic, Germany) at 8500 rpm for 5 min. Thereafter, 2g of lipid phase (Labrafil[®] M 2125 CS) was added to the water phase at the same temperature and formed a pre-dispersion at 20,000 rpm for 5 min. The resulting dispersion was homogenized

at the same temperature by using a one stage high pressure homogenizer (Stansted Fluid Power Ltd, UK) during 4 passes at 1000 bars. The formulation was stored in glass vials and cooled down slowly to room temperature (RT).

Process studies from 50g to 1kg

50 g sample

38.5 ml of pre-heated aqueous phase containing 2% (w/w) of stearyl macroglycerides (Gelucire® 50/13) and 1% (w/w) of soybean lecithin (Phospholipon® 90G) as surfactant was formed by using ultra-turrax (IKA® T18, Germany) at 11,000 rpm for 5 min. Thereafter, 10g of lipid phase (Labrafil® M 2125 CS or Labrafil® M1944 CS) was added to the water phase and formed a pre-dispersion at 20,000 rpm for 5 min. The resulting dispersion was homogenized by using a two stage high pressure homogenizer (APV2000, Denmark) during 5 min. The pressure was constantly kept at 600 and 200 bars, in the first and second stages respectively during the whole process. The formulation was stored in glass vials and cooled down slowly to room temperature (RT).

1 kg sample

A procedure similar to the previous one has been used with some adjustments. 770 ml of pre-heated aqueous phase containing 2% (w/w) of stearyl macroglycerides (Gelucire® 50/13) and 1% (w/w) of soybean lecithin (Phospholipon® 90G) and 200g of lipid phase (Labrafil® M 2125 CS or Labrafil® M1944 CS) were used. The ultra-turrax mixing time and homogenization time were 15 min. Mechanic stirring was maintained into the homogenization funnel with a Rayneri mixer. The formulation was dispatched into 40ml-glass vials and cooled down slowly to room temperature (RT).

2.2.2. Particle size and zeta potential measurements

The particle size and zeta potential of nanodispersions were measured using a Nano-ZS90 apparatus (Malvern Instruments, Orsay, France). The average hydrodynamic diameter and PdI were determined by *quasi*-elastic light scattering (QELS). The zeta potential determinations were performed using electrophoretic laser Doppler velocimetry. The samples were diluted to 1/300 in Milli-Q water for size analysis and in 1 mM NaCl solution for zeta potential measurements.

2.2.3. X-ray diffraction (XRD)

X-ray scattering experiments were performed on the 5.2L beamline at ELETTRA Synchrotron Light Laboratory (Trieste, Italy). The energy and wavelength of the incident X-ray beam were 8 KeV and 1.54 Å respectively. The samples were thermostated in the laboratory made sample holder, Microcalix, allowing both sample temperature control and simultaneous differential scanning calorimetry analysis. Small-angle (SAXS) and wide-angle (WAXS) X-ray scattering patterns were recorded simultaneously using a 2D single photon counting detector (Pilatus 100K) based on hybrid pixel technology (Dectris, Swiss) and a position-sensitive linear gas detectors filled with an argon-ethane mixture respectively. After 2D-image treatment in the SAXS experiments, the scattered intensity was reported as a function of the scattering vector $q = 4\pi\sin\theta/\lambda = 2\pi/d$, where 2θ is the scattering angle, λ is the wavelength and d is the repeat distance between two reticular plans. The calibration of the WAXS and SAXS detectors were achieved using pure tristearine ($2L\beta$ form), characterized by short spacings of 4.59, 3.85 and 3.70 Å \pm 0.01 Å and silver behenate characterized by a long spacing of 58.380 Å \pm 0.001 Å respectively. The samples were loaded into quartz capillaries (Quarzkapillaren, Germany) with external diameter of 1.4 \pm 0.1 mm and a wall thickness of 0.01 mm. All data were analyzed with the IGOR Pro software (WaveMetrics, Inc. USA).

2.2.4. Cryogenic transmission electron microscopy (Cryo-TEM)

The morphology of nanodispersions was observed using a cryo-TEM system (JEM 2100, JEOL, Japan). All nanodispersions were diluted to 1/40 (v/v) in Milli-Q water. 10 μ l of samples were placed on a copper grid, and the solution excess was carefully removed by a filter paper. The vitrification of the film was achieved by rapidly plunging the grid into liquid ethane. The vitrified sample was then transferred to the microscope. The temperature was kept about -180°C during both the transfer and the viewing procedures in order to prevent sample perturbation and the formation of ice crystals.

2.2.5. Optical microscopy

Sample preparations were examined by microscopy in white light optical using a Nikon E600 Eclipse microscope (Champigny/Marne, France) equipped with a long focus objective (LWD 20 x 0.55; 0-2 mm). The images were recorded with a Mightex BCE 030-U camera at a resolution of 1024 x 768 pixels. The samples were prepared at 60°C, placed between two

circular glass slides (26 mm thick) at the same temperature, observed in the 60-20°C range and monitored by a hotplate at heating or cooling rates of 5°C/min.

3. Results and Discussions

Two fundamental parameters have been changed during the formulation studies, the nature of the lipophilic phase (caprylic-capric triglycerides, linoleoyl polyoxylglycerides and oleoyl polyoxylglycerides) and the mixture of stabilizers, i.e. stearyl macrogolglycerides to soybean lecithin ratio. These stabilizers have been chosen because they have already brought interesting stability properties to other lipid-based nanodispersions developed in the laboratory (unpublished data). The parameters concerning the preparation process (temperature, mixing and homogenization times, applied pressures...) remained constant. Figure 2.1 summarized the results obtained during this part of the work and expressed for each formulation the success of the preparation. In the present case, first step successful criteria have been defined as a formulation with mean diameter comprised between 100 and 200 nm at the end of the preparation process and size distributions stable during at least three months at room temperature. The interests of this target size range have been extensively discussed in the literature depending on the pharmaceutical applications⁵. To overview the main ideas, this size range allows a passive targeting of the drug-loaded nanocarriers by an accumulation into some organs (liver) or tissues such as tumor areas due to leaky vasculatures and the EPR effect. In the case of administration routes implying mucous layers, these sizes allow passive diffusion of the carriers into these layers⁶⁻⁸. Furthermore, particle endocytosis is possible with these particle sizes⁹⁻¹⁰. The results showed that the composition of the lipid phase did not significantly affect the size distribution and stability of the lipid nanoparticles, while a threshold amount of surface active agents was required, especially concerning stearyl macrogolglycerides. This limit could be fixed around 2 wt% when the amount of total lipid was 20 wt%. At the concentrations used (max. 3 wt%), pure phospholipid mixture was not sufficient to efficiently stabilize the nanoparticles.

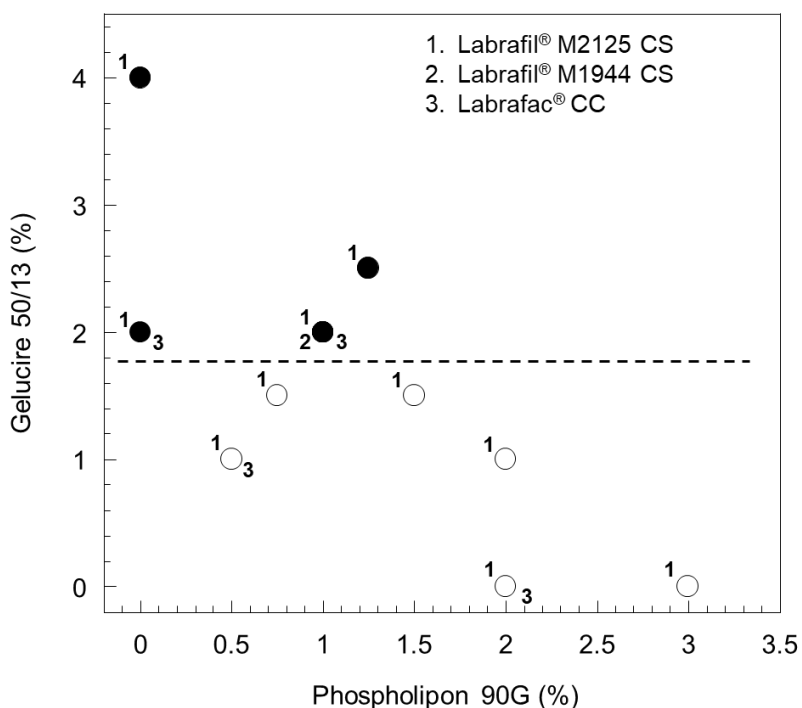


Figure 2.1. Summary of the formulation studies depending on the proportion of stabilizers and the lipid phase composition. Filled symbol: successful formulations; open symbol: unsuccessful formulations. Successful attributes have been defined as mean diameter comprised between 100 and 200 nm and stable during at least three months. The concentration of the lipid phase was 20% of the total suspension (w/w).

Cryo-TEM after plunge freezing allows direct investigation of colloids very close to their native state due to sample vitrification. Thus, the particle structures of caprylic-capric triglycerides, linoleoyl polyoxylglycerides or oleoyl polyoxylglycerides stabilized by the stearyl macroglycerides – soybean lecithin (2:1) mixture and stearyl macroglycerides alone have been compared (Figure 2.2). In Cryo-TEM micrographs, the nanodispersions stabilized only by stearyl macroglycerides or the nanodispersions containing caprylic-capric triglycerides as lipid phase appeared as classical NE, i.e. as more or less circular structures with an even distribution of contrast. Because of the low contrast of polyethylene glycol, the dense (dark) structures corresponded to the lipophilic core of the NE.

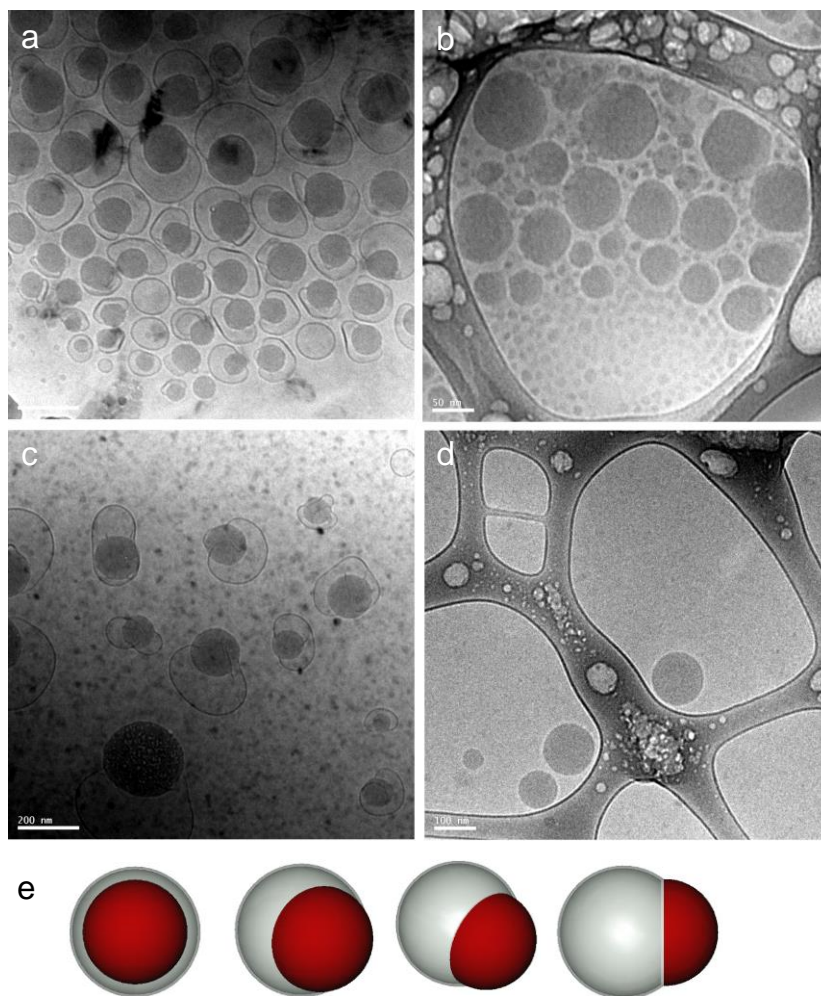


Figure 2.2. Cryo-TEM view of nanodispersions containing (a) linoleoyl polyoxylglycerides / stearoyl macroglycerides / soybean lecithin, (b) caprylic-capric triglycerides / stearoyl macroglycerides / soybean lecithin, (c) oleoyl polyoxylglycerides / stearoyl macroglycerides / soybean lecithin and (d) linoleoyl polyoxylglycerides / stearoyl macroglycerides. (e) schematic views of Janus nanoparticles depending on their orientation.

With Labrafils[®] (oleyl or linoleyl polyoxylglycerides), the incorporation of 1% of phospholipids into the formulation led to totally different nanodispersions in which the lipophilic dark core was partially surrounded by a non-dense compartment delimited by a dense layer. As expected with formulation stabilized by phospholipids, some typical images of liposomes were present on Figure 2.1. However, taking into account the observation of tens views from several batches, the most representative objects of the preparation were compartmented nanoparticles (Figure 2.1). From the cryo-TEM images, some structural assumptions could be proposed. The ring-shaped structure strongly suggested the presence of phospholipid-based bilayers around the non-dense hydrophilic compartment. Furthermore, the dense layer thickness could be estimated between 4

to 5 nm which was totally compatible with the thickness of the hydrophobic part of lipid bilayers. Cryo-TEM also suggested the absence of supramolecular organization, i.e. cubic or hexagonal phases, into the lipophilic dark domain. Linoleoyl polyoxylglycerides, synthesized by a partial alcoholysis / esterification reaction using corn oil (main fatty acid is linoleic acid ~60%) and PEG 300, is clearly more polar than caprylic-capric triglycerides which contains pure short chain glycerides. However, even with Synchrotron high-flux beam, and important nanoparticle concentrations (20 wt%), it was not possible to detect liquid-crystalline mesophase organization of linoleoyl polyoxylglycerides, as observed with some polar glycerides¹¹⁻¹⁴. Hence, the small-angles x-ray scattering pattern demonstrates the lack of supramolecular structure into these particles confirming the cryo-TEM observations (Figure 2.3).

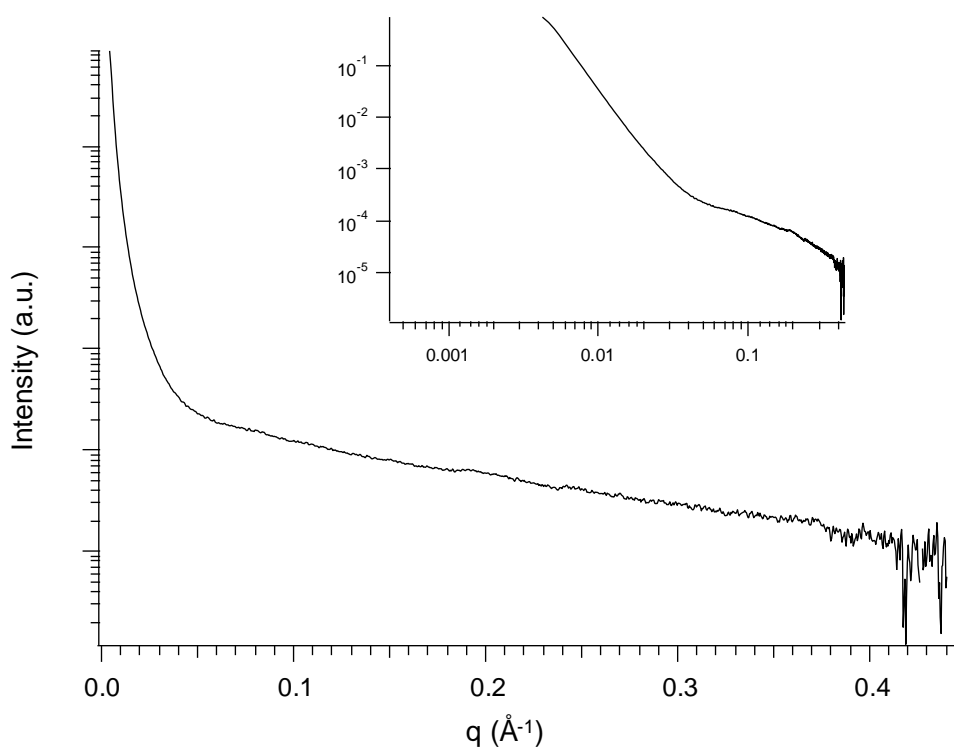


Figure 2.3. SAXS profile at 20 °C of the nanodispersions containing linoleoyl polyoxylglycerides. Inset: log-log representation. Results acquired after 8 days of storage at 20 °C.

A particular focus has been done on the linoleoyl polyoxylglycerides containing *Janus* nanoparticles, and the long-term stability of these formulations was described in Figure 2.4. Surprisingly, stored in aqueous medium at room temperature, i.e. without any further treatment such as lyophilization, the nanoparticles remained stable both from mean size and polydispersity indexes point of views. As defined as critical attribute, the size of the particle was comprised in

the range 100 to 200 nm and remained in this range during at least 20 months at room temperature. During the same time lapse, polydispersity indexes were around 0.1 suggesting narrow size distributions. Determined in a 1 mM NaCl solution, the zeta potential of these nanoparticles was quite low, around -5 mV.

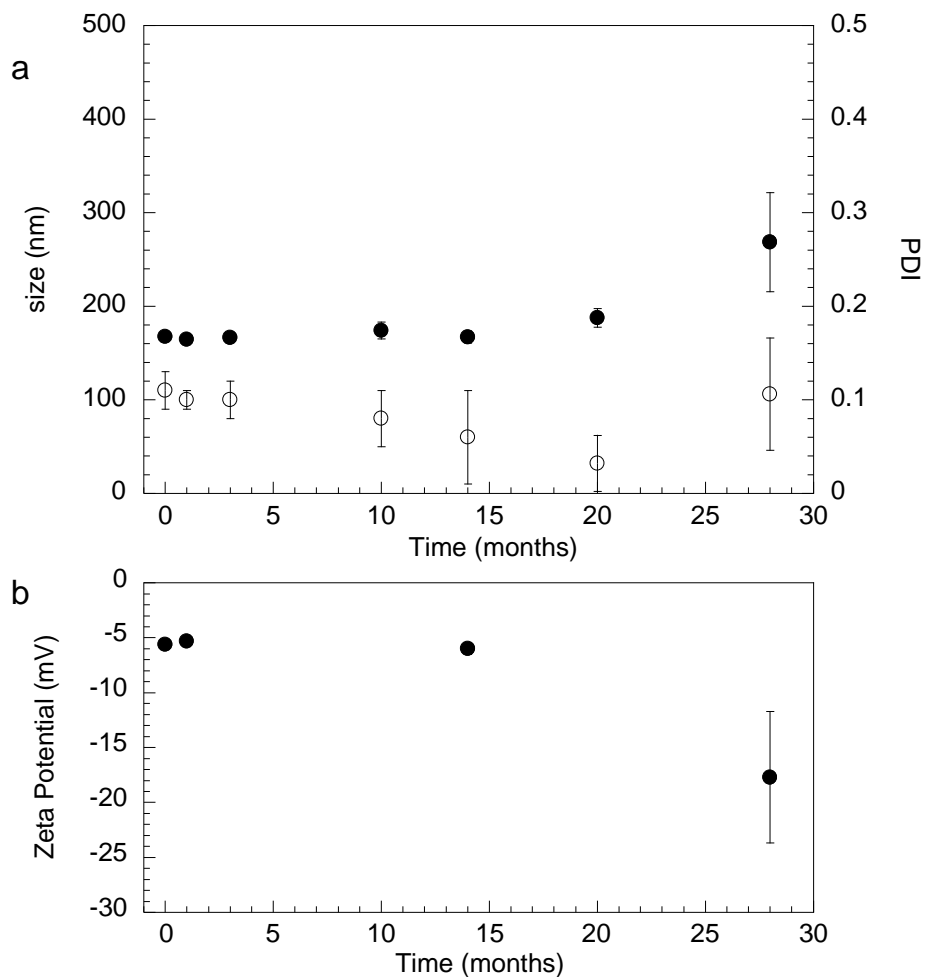


Figure 2.4. Long-time size stability of the nanoparticles prepared with 3% of the stearyl macroglycerides – soybean lecithin (2:1) mixture. (a) mean size \pm SD (nm) and PDI \pm SD; (b) zeta potential \pm SD; $n = 3$ (three different batches).

Because of the low zeta potential values, electrostatic stabilization should be reduced, confirming the crucial role of the steric repulsion, due to PEG layer, on long-time physical stability. By attentively looking at cryo-TEM image where the nanoparticles were concentrated, it was possible to notice regions where the bilayers were flat or deformed because of the close contact between two particles (Figure 2.5). The minimal distance among these bilayers was in the range 8 to 10 nm and would certainly result from the presence of polyethylene glycol chains at the

nanodispersion surfaces.

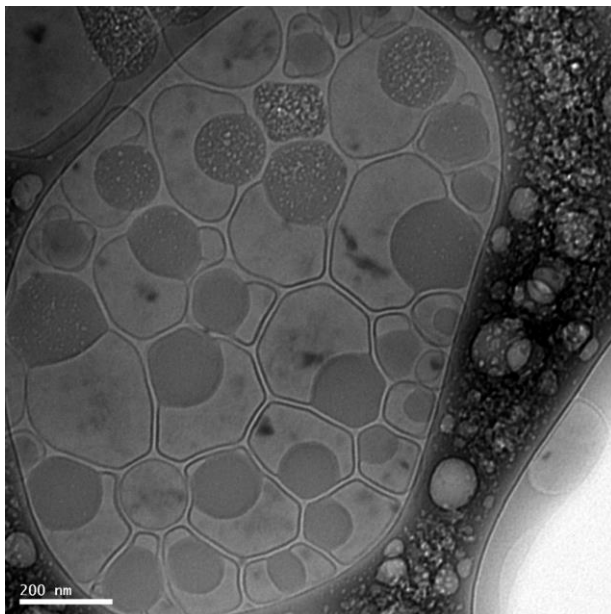


Figure 2.5. Janus nanoparticles deformations on concentrated cryo-TEM grid.

At 24 months, the zeta potential of this colloidal suspension decreases to -18 mV while the size significantly increases (Figure 2.4). These zeta potential values gave us some information on chemical and physical stability of the system. Indeed, it is known that phospholipids and glycerides could be hydrolyzed with time, resulting in the release of fatty acids which could destabilize the dispersion¹⁵ and decrease their zeta potential (more negative values)¹⁶.

Because of their special architecture, the synthesis of nano-sized *Janus* particles is very difficult. Most of the technologies currently used to produce such particles do not allow mass productions, so *Janus* particles synthesis still remains a challenge to control the size, shape, the various structural/ physical/ chemical properties, and the ability to scale-up production². Our preparation process is based on high-pressure homogenization. This operation is widely used in food or cosmetic industries but also in the pharmaceutical field to produce injectable lipid emulsions for parenteral nutrition or drug delivery purposes. Then, three different batch sizes of *Janus* nanoparticles have been produced in the laboratory, 10 g, 50 g and 1000 g, with two different homogenizers. As described in Figure 2.6, it is also possible to produce *Janus* nanoparticles with the larger batch. Compared to the small batches, this preliminary scale-up to 1 kg highlighted the importance to maintain a low-speed agitation into the homogenizer tank as destabilization of the pre-dispersion has been observed with unstirred tank. Fortunately, mixing vessels are currently available into hundreds- or thousands of liters industrial homogenizers.

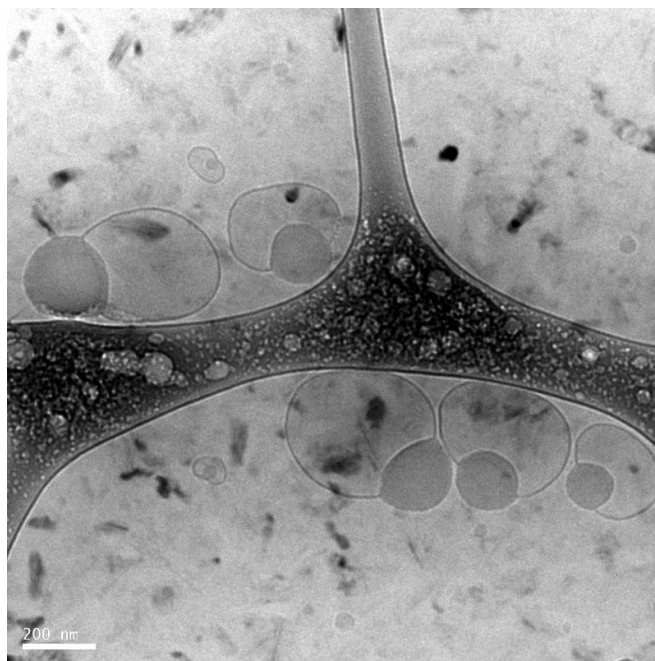


Figure 2.6. Cryo-TEM view of 1 kg batch of Janus nanoparticles produced by high-pressure homogenization.

With both Labrafil[®], nanoparticles developed here have a very particular structure which could be discussed as the combination of NE and liposomes. To make a stable NE, a lot of factors must be taken into account as order of incorporation, shear intensities or appropriate composition. It is generally admitted that a significant excess of surfactant is required in the continuous phase in order to rapidly covered new surface area created during coarse emulsion size reduction (homogenization)¹⁷. Depending on its concentration and molecule critical packing parameter, this excess is self-organized into supramolecular objects, such as micelles, in equilibrium with nanodroplets. When phospholipids are used as stabilizers, the process generates liposomes which are often simultaneously observed with nanoparticles or nanodroplets on cryo-TEM pictures¹⁸. Here, NE droplets (dark core) and phospholipid bilayers (ring-shape layer) seemed solidarized as the proportion of free liposomes was certainly lower than 2-3% (from cryo-TEM observations). Several works already deal with synthetic nanosystems containing both phospholipid bilayers and lipid core. Teixeira et al. hypothesized that a partial phase separation of the surfactant mixture may be responsible for the formation of anisotropic “handbag”-like structures with membrane extrusions. This was originally obtained with the addition of positively charged stearylamine to lecithin for the stabilization of triglyceride-based emulsions¹⁹. Further studies characterized the mechanism of formation of these objects but also stated on the difficulty to control their preparation and to increase their

concentration, less than 20%, compared to other structures such as liposomes and lipid droplets²⁰. Emulsomes have been also described as isotropic systems corresponding to emulsion droplets stabilized with phospholipid bilayers²¹. The proposed preparation process corresponds to the rehydration of phospholipid films with aqueous suspension of lipid nanodispersions (liquid or solid). However, to our knowledge, no evidences on the object structure, as cryo-TEM for example, have been furnished.

The formulation studies indicated that soybean lecithin and stearyl macroglycerides were important for the stability of the *Janus* nanoparticles but were not sufficient to explain their formation mechanism. Indeed, in presence of these surface active agents caprylic-capric triglycerides based systems were not compartmented while oleyl or linoleoyl polyoxyglycerides based systems were. This observation prompted us to seek the driving force of the formation mechanism into the polyoxyglycerides physical-chemistry. Due to their synthetic routes, such type of excipients are complex mixtures containing more than 60 wt% of glycerides and less than 40 wt% of mono- and diesters between fatty acids (oleic or linoleic acids) and PEG₃₀₀ (supplier data). Nonionic surfactants having short PEG chains are known to have a phase inversion temperature. Due to the dehydration of the hydrophilic PEG headgroup, these compounds are less water soluble above this phase inversion temperature and their hydrophilic-to-lipophilic balances decrease with temperature²². Thus polyoxyethylene monoalkyl derivatives containing 18 carbons in their lipophilic chain and 6 oxyethylene units would have cloud points, defining their water solubility limits, in the range of 35-40°C depending on their concentration in water solution²³. Figure 2.7a describes the behaviour of a water - linoleoyl polyoxyglyceride mixture with temperature from 60°C to 20°C to 60°C at 5°C/min. A clear temperature-dependant phase separation could be observed into the water droplets when the temperature decreased from 60°C to 20°C. More precisely, the first step of this phase separation appeared as typical myelin figures which were visible at the water – lipid interface at ~40°C (Figure 2.7b). These figures are non equilibrium cylindrical structures made of concentric bilayers that can form during the dissolution and swelling of surfactant lamellar phases²⁴. These clearly indicated the interpenetration of polyoxyethylene derivatives and water fluxes and then the growth of bilayers from the polyoxyglyceride excipient phase to the aqueous phase under a certain temperature. This flux of materials has been confirmed by considering the diameter of single droplets, as expresses on Figure 2.7c, which increased when the temperature decreased. Interestingly, phase separation and diameter modification were reversible as observed when the temperature was increased from 25°C to 60°C.

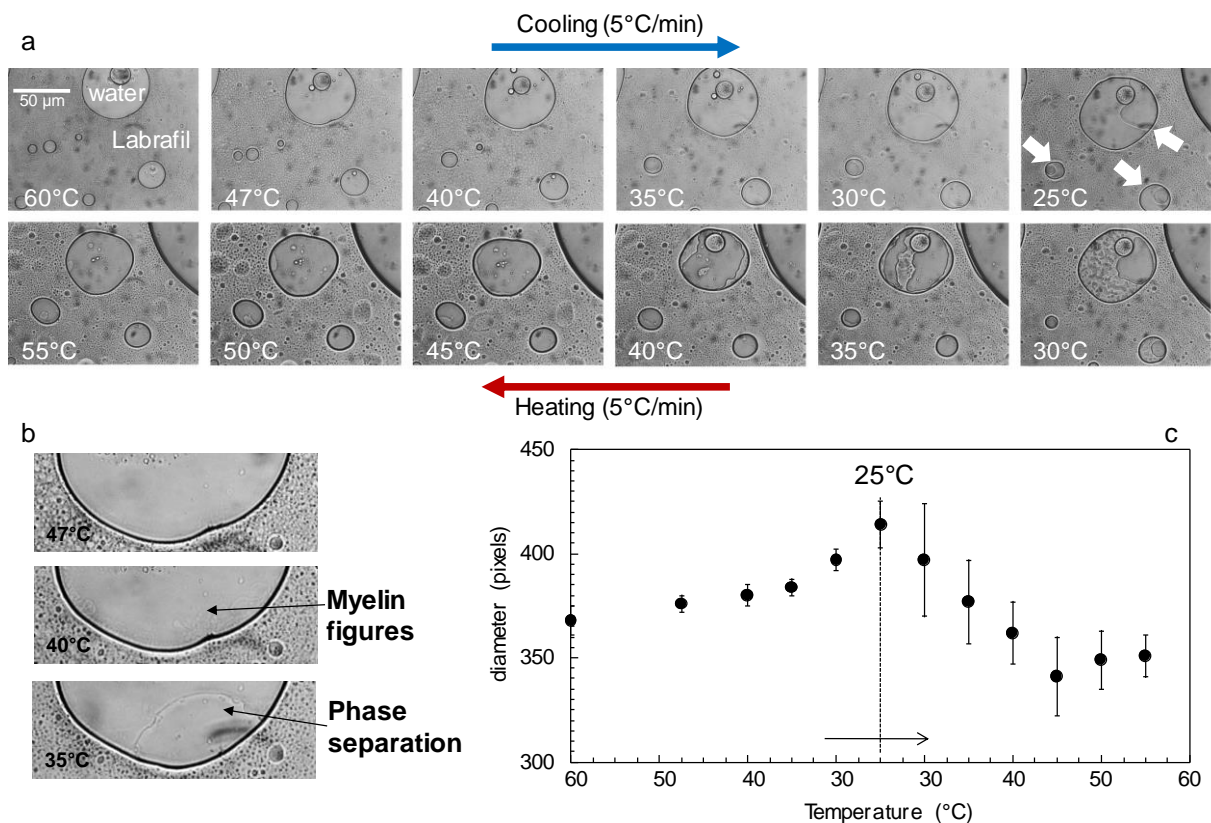


Figure 2.7. Follow-up of a linoleoyl polyoxylglycerides / water (1:1) mixture during its cooling from 60°C to 25°C and its heating to 60°C. (a) Optical microscopy pictures showing water droplets into linoleoyl polyoxylglycerides. At 25°C, arrows point out phase separation. (b) Focus on myelin figures and phase separation at 3 temperatures (47°C, 40°C and 35°C). (c) Mean diameter of a water droplet during its cooling and heating.

To confirm these macroscopic observations at the molecular scale, x-ray diffraction experiments have been done on linoleoyl polyoxylglycerides containing or not water (Figure 2.8). With pure linoleoyl polyoxylglycerides, no diffraction peaks were visible both at 20°C and 60°C. The SAXS pattern only suggested the presence of diffusing objects into this complex excipient, certainly inverse micelles of the polyoxyethylene alkyl derivatives into the glycerides. The addition of small amounts of water into linoleoyl polyoxylglycerides excipient, here 10 wt%, led to the growth of two diffraction peaks characterizing a lamellar organization with a period of 87 Å at 20°C. This organization, sensitive to the temperature, totally disappeared above ~36°C. This lamellar organization is totally consistent with previous work from Kunieda and co-workers who investigated the phase behaviour of poly(oxyethylene) unsaturated-C18 ether in water at room temperature. Surfactants having mean chains of 6 EO (PEG₃₀₀) generates lamellar phases on a large extend of hydration, from less than 10 wt% of

water to fully hydrated phases with excess water²⁵. Still Figure 2.8, at higher temperature, a diffusion signal was maintained suggesting the incorporation of water droplets into the linoleoyl polyoxyglycerides. The presence of this water-in-oil dispersion seems consistent with an increase of the packing parameter of the polyoxyethylene alkyl derivatives with temperature thanks to the dehydration of the polar head allowing the transition from a lamellar organization to an inverted structure.

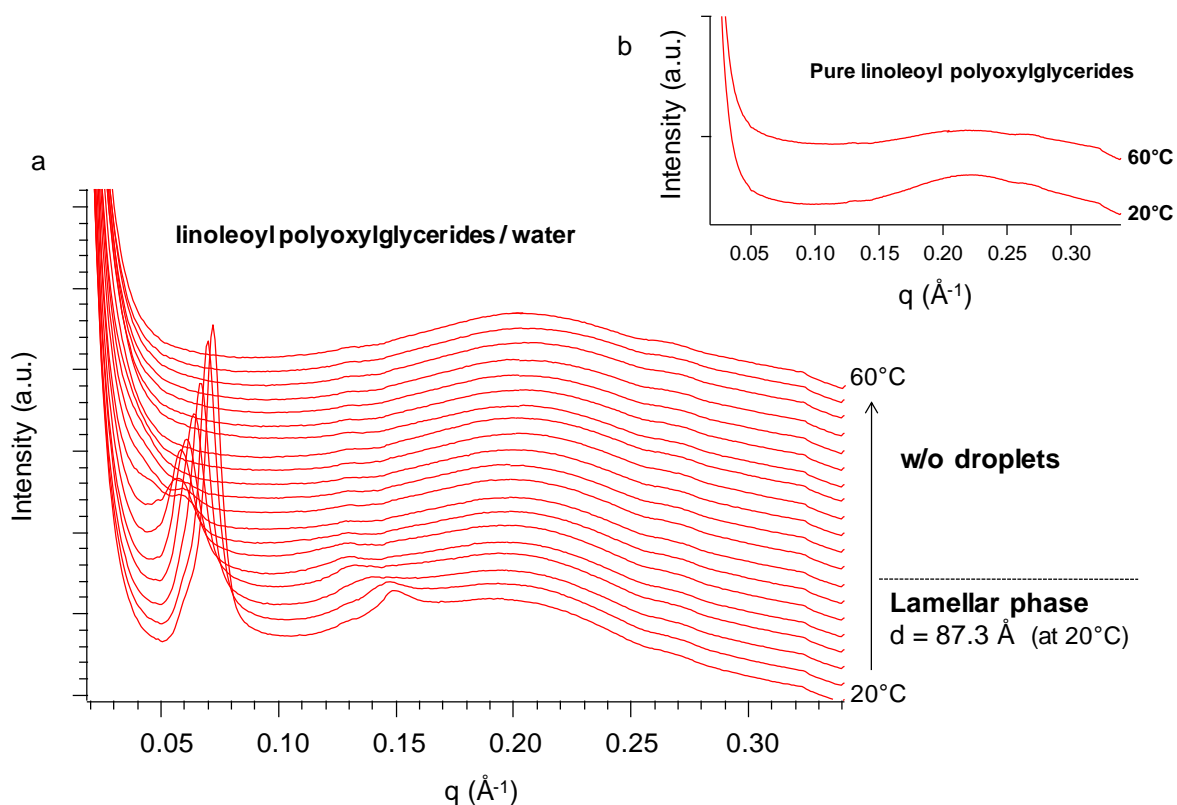


Figure 2.8. SAXS patterns with temperature of (a) linoleoyl polyoxyglycerides / water (9:1) between 20°C to 60°C (heating rate: 2°C/min) and (b) pure linoleoyl polyoxyglycerides at 20°C and 60°C.

From macroscopic to microscopic observations, temperature changes induced phase separation into polyoxyglycerides – water mixtures. Transposed to the preparation of the *Janus* nanoparticles, it was reasonable to assume that 1) after dispersion and homogenization at high temperature, a multiple emulsion is formed with internal aqueous globules stabilized with alkyl-short PEG derivatives and intermediate oil globules stabilized by lecithin and stearyl macroglycerides 2) a phase separation occurs into the nanodroplets when the hydrophilicity of the PEG₃₀₀ esters increases during cooling and 3) these esters contribute to the bilayer that

surround the aqueous compartment.

4. Conclusion

Because of their original structure, their long-time stability and the scalable process they require, the lipid *Janus* nanoparticles developed here seem very powerful. The presence of compartments allows one to envisage the incorporation of lipophilic and hydrophilic API in the same particle. This would be very interesting for theranostic applications or development of FDC products. Defined by the combination of therapeutic and diagnostic agents on a single platform, theranostic nanoparticles can simultaneously detect, image, and treat disease²⁶. To reach this goal, innovative multifunctional carriers have to be developed. FDC describes products that have two or more active ingredients into a single dosage presentation. The overriding principle is whether the product contains two or more actives that provide a defined additive or synergistic therapeutic benefit in a dosage form. The pharmaceutical industry pays increasing attention to these FDC products as suggests by the growth of their approval by the FDA, from 1 or 2/year in the early nineties to 4 to 12/year last years²⁷. On the last 131 FDA-approved FDC products, 98 are oral dosage forms and 19 of them reach a billion dollars in annual sales. In the field of the nanotechnologies and targeted therapies, several authors underlines that combinations are very promising but that this area of delivering multiple drugs with a single vehicle remains largely unexplored^{28,29}. This is all the more true if the APIs have opposite solubility properties. This is one of the reasons explaining why only 4% of the approved FDC products and 14% of products in phase of development deal with parenteral routes. Having concentric lipophilic and hydrophilic domains, liposomes, emulsomes and ISAsomes (cubosomes, hexosomes) should be able to co-encapsulate liposoluble and hydrosoluble molecules. However, because of the full imbrication of the lipophilic and hydrophilic compartments, the incorporation of an API into one of them, i.e. the phospholipid bilayer of the liposomes, could destabilize it³⁰⁻³² and may lead to leakage from the second compartment. With their more or less independent compartments, anisotropic *Janus* morphologies show a promising capability for the independent release of two different API from the same nanoparticles^{33,34}. In the field of self-assembled lipid-based systems, Tran and al recently developed interesting internally ordered *Janus* lipid nanoparticles containing mixes of cubic and hexagonal phases³⁵.

Further studies should be done to deeply investigate the pharmaceutical properties of these *Janus* nanoparticles, notably their encapsulation potencies for API or diagnostic agents and

their ability to protect unstable molecules. It could be also informative to study the interaction between these nanoparticles and serum proteins as the presence of complex mixtures as macroglycerides which contain di-blocks (monoesters) and tri-blocks (diesters) surfactants³⁶⁻³⁸ would create a complex interface between the particles and the dispersion medium. The present nanodispersions should be stabilized by a two-layer PEG₁₅₀₀ coating in which the most external layer corresponds to the end of extended chains (monoesters) and a basal layer composed of PEG₁₅₀₀ anchored by both extremities (diesters). At last, their *in vivo* stability and biodistribution could be checked.

Author contributions

T.T.C. did the formulation and stability studies. E.M. investigated the formation mechanism. C.T.L.T. performed the process scale-up. H.A. contributed to the SAXS experiments. G.F. performed cryo-TEM experiments. S.L. provided scientific discussions. V.F. designed experiments and analyzed the data. All the authors wrote or commented the manuscript.

References

1. De Gennes, P.G. ; *Angew Chem. Int. Ed. Engl.* **1992**, *31*, 842-845.
2. Tran, L.T.C. ; Lesieur, S. ; Faivre, V. *Exp. Opin. Drug. Del.*, **2014**, *11(7)*, 1061-1074.
3. Du, J.; O'Reilly, R.K. *Chem. Soc. Rev.*, **2011**, *40*, 2402–2416.
4. Walther, A.; Müller, A.H.E.; *Chem. Rev.*, **2013**, *113 (7)*, 5194–5261.
5. Puri, A., Loomis, K.; Smith, B.; Lee, J-H.; Yavlovich, A.; Heldman, E.; Blumenthal, R.; *Crit. Rev. Ther. Drug. Carr. Syst.*, **2009**, *26(6)*, 523–580.
6. Ponchel, G.; Montisci, M.J.; Dembri, A.; Durrer, C.; Duchêne, D.; *Eur. J. Pharm. Biopharm.*, **1997**, *44*, 25–31.
7. Dawson, M.; Krauland, E.; Wirtz, D.; Hanes, J.; *Biotechnol. Progr.*, **2004**, *20(3)*, 851–857.
8. Li, X. ; Chen, D., Le, C. ; Zhu, C., Gan, Y., Hovgaard, L., Yang, M. ; *Int. J. Nanomed.*, **2011**, *6*, 3151–3162.
9. Iversen, T.G.; Skotland, T.; Sandvig, K., *Nano Today*, **2011**, *6(2)*, 176–185.
10. Zhao, F.; Zhao, Y.; Liu, Y., Chang, X.; Chen, C.; Zhao, Y.; *Small*, **2011**, *7(10)*, 1322–1337.
11. Svensson, A.; Neves, C.; Cabane, B.; *Int. J. Pharm.*, **2004**, *281(1-2)*, 107–118.
12. Morán, M.C.; Pinazo, A.; Clapés, P.; Rosa Infante, M.; Pons, R.; *J. Phys. Chem. B.*, **2005**, *109(48)*, 22899–22908.
13. Guo, C.; Wang, J.; Cao, F.; Lee, R.J.; Zhai, G.; *Drug Discov. Today*, **2010**, *15(23-24)*, 1032–1040.
14. Angelov, B.; Angelova, A.; Mutafchieva, R.; Lesieur, S.; Vainio, U.; Garamus, V.M.; Jensen, G.V.; Pedersen, J.S.; *PCCP*, **2011**, *13(8)*, 3073–3081.
15. Ickenstein, L.M.; Sandström, M.C.; Mayer, L.D.; Edwards, K.; *BBA*, **2006**, *1758(2)*, 171–180.
16. Werling, J.; Graham, S.; Owen, H.; Nair, L.; Gonyon, T.; Carter, P.W.; *Eur. J. Pharm. Biopharm.*, **2008**, *69(3)*, 1104–1113.
17. Mason, T.G.; Wilking, J.N.; Meleson, K.; Chang, C.B.; Graves, S.M.; *J. Phys.: Condens. Matter*, **2006**, *18(41)*, 635–666.
18. Klang, V.; Matsko, N.B.; Valenta, C.; Hofer, F.; *Micron*, **2012**, *43(2-3)*, 85–103

19. Teixeira, H.; Dubernet, C.; Rosilio, V.; Benita, S.; Lepault, J.; Erk, I.; Couvreur, P.; *Pharm. Res.*, **2000**, *17(10)*, 1329–1332.
20. Raffournier, C. ; Dubernet, C. ; Couvreur, P. ; Ollivon, M. ; *Prog. Coll. Polym. Sci.*, **2004**, *128*, 139–142.
21. Paliwal, R.; Paliwal, S.R.; Mishra, N.; Mehta, A.; Vyas, S.P.; *Int. J. Pharm.*, **2009**, *380(1-2)*, 181–188.
22. Schick, M.J. ; *Nonionic Surfactants : Physical Chemistry*, **1987**, CRC Press, 1158p.
23. Einaga, Y.; *Polym. J.*, **2009**, *41*, 157-173.
24. Reissig, L.; Fairhurst, D.J.; Leng, J.; Cates, M.E.; Mount, A.R.; Egelhaaf, S.U.; *Langmuir*, **2010**, *26(19)*, 15192-15199.
25. Kunieda, H.; Shigeta, K.; Ozawa, K.; *J. Phys. Chem. B*; **1997**, *101(40)*, 7952-7957.
26. Janib, S.M. ; Moses, A.S. ; MacKay, J.A. ; *Adv. Drug. Deliv. Rev.*, **2010**, *62(11)*, 1052-1063.
27. Karali, T.; Sedo, K.; Bossart, J.; *Drug Dev. Del.*, **2014**.
28. Lee, J.H.; Nan, A.; *J. Drug Deliv.*, **2012**, 1-17.
29. Ma, L.; Kohli, M.; Smith, A.; *ACS Nano*, **2013**, *7(11)*, 9518-9525.
30. Gregoriadis, G. ; *Liposome Technology: Entrapment of drugs and Other Materials into Liposomes*, **2007**, CRC Press, 398p.
31. Magalhaes T.; Proietti Viotti, A.; Teperino Gomes, R. ; Viana de Freitas, T. ; *Biotech. Appl. Biochem.*, **2001**, *33*, 61-64
32. Noble, C.O.; Guo, Z.; Hayes, M.E.; Marks, J.D.; Park, J.W.; Benz, C.C.; Kirpotin, D.B.; Drummond, D.C.; *Cancer Chemother. Pharmacol.*, **2009**, *64*, 741-751.
33. Xie, H.; She, Z.G.; Wang, S.; Sharma, G.; Smith, J.W.; *Langmuir*, **2012**, *28(9)*, 4459-4463.
34. Hwang, S.; Lahann, J.; *Macromol. Rapid. Commun.*, **2012**, *33(14)*, 1178-1183.
35. Tran, N.; Mulet, X.; Hawley, A.M.; Conn, C.E.; Zhai, J.; Waddington, L.J.; Drummond, C.J.; *Nano Letters*, **2015**, *15(6)*, 4229-4233.
36. Brubach, J.B.; Ollivon, M.; Jannin, V.; Mahler, B.; Bourgaux, C.; Lesieur, P.; Roy, P. ; *J. Phys. Chem. B.*, **2004**, *108(46)*, 17721-17729.
37. El Hadri, M. ; Achahbar, A.; El Khamkhami, J.; Khelifa, B.; Tuyet, T.L.C. ; Faivre, V.; Abbas, O.; El Marssi, M. ; Bougrioua, F. ; Bresson, S.; *J. Mol. Struct.*, **2015**, *1083*, 441-

449.

38. El Hadri, M. ; Achahbar, A.; El Khamkhami, J.; Khelifa, B.; Faivre, V.; Abbas, O.; Bresson, S.; *Chem. Phys. Lip.*, **2016**, *200*, 11-23.

INCORPORATION OF HYDROPHILIC FERRO-FLUIDS INTO LIPID-BASED JANUS NANOPARTICLES

Elodie MILLART¹, Aude MICHEL², Gilles BOEMARE³, Nicolas GUIBLIN³, Jean-Blaise BRUBACH⁴, Christine MENAGER², Sylviane LESIEUR¹, Vincent FAIVRE^{1*}

¹ Institut Galien Paris-Sud, Université Paris-Saclay, Univ. Paris-Sud, Labex LERMIT,
5 rue Jean-Baptiste Clément, 92296 Châtenay-Malabry, France.

² Laboratoire PHENIX, Sorbonne Universités, UPMC, Université Paris 06, UMR CNRS 8234,
4 place Jussieu 75005 Paris, France

³ Structures, Propriétés et Modélisation des Solides (SPMS), CentraleSupélec,
Grande voie des vignes, 92296 Châtenay-Malabry

⁴ Ligne AILES, Synchrotron SOLEIL,
L'Orme des Merisiers Saint-Aubin, 91192 Gif-sur-Yvette Cedex

* Corresponding author

Tel. : +33 146835465 ; Fax : +33 146835312.

E-mail address : vincent.favre@u-psud.fr (Vincent FAIVRE)

ABSTRACT

Over the past decade, the development of agents derived from nanotechnology has been applied to overcome the problems of traditional techniques for advanced diagnosis and therapy. In particular, improvements in nanoparticle design have created new models for theranostics, which is defined as the combination of therapeutic and diagnostic agents within a single platform. This paper reports the preparation and characterization of hydrophilic ferrofluids for further encapsulation in the aqueous part of lipid-based *Janus* nanoparticles. Physico-chemical analysis indicated that the integrity of the maghemite is preserved after coating but its entrapment was not demonstrated.

KEYWORDS

Compartmented lipid nanoparticles, cryo-transmission electron microscopy, ferrofluid, Fourier-transform infrared spectroscopy, *Janus* lipid nanoparticles, high pressure homogenization, maghemite, PAA, PAAMA, small-angle x-ray diffraction, SPION, thermogravimetric analysis

1. Introduction

Nanotechnology gives the opportunity to assemble therapeutic and diagnostic agents as a single theranostic platform which is a molecular platform that simultaneously combines diagnosis and therapy [1–4]. The main goal is to diagnose and treat the diseases at their earliest stage. Liposomes are a valid platform for theranostic nanomedicine, because of their size, hydrophobic and hydrophilic character, biocompatibility, biodegradability, low toxicity, and immunogenicity [5–7]. First described in the 60s by Bangham [8], liposomes are core-shell structures defined as closed vesicles delimited by one or several concentric hydrated lipid bilayers that entrap a part of the aqueous phase where they have been formed. Usually, liposomes are mainly composed of phospholipids. The advantage of these structures lies in their double ability to incorporate hydrophilic substances in their inner aqueous core and to encapsulate hydrophobic or amphiphilic compounds in their bilayer shell. Thus, several liposomal formulations have reached the market during the last twenty years (Ambisome®, Doxil®, Myocet®, ...) for therapeutic applications. Such constructs also present great opportunities to engineer theranostic nanoscale delivery systems [7]. The first property has been successfully exploited to load liposomes with a hydrophilic magnetic fluid aqueously stabilized : MFL, also referred to as magnetoliposomes [9]. Once the “diagnostic” agent is included in the magnetoliposome, the next step is to encapsulate the “therapeutic” compound. In this purpose, when the drug is also hydrophilic, a competition with the magnetic fluid can occur and reduce drastically the encapsulation rates. On the contrary, when the drug is hydrophobic, a potential bilayer destabilization can be observed. In order to overcome these drawbacks, bicompartmented lipid-based *Janus* nanoparticles have been developed. They are composed of a lipid compartment and an aqueous compartment delimited by a lipid bilayer made of compounds approved by authorities (pharmacopoeias, EMA, FDA...). The two distinct sides of the *Janus* nanoparticles make them very interesting objects for the co-administration of two API with opposite solubilities. In the present work, we investigated the development of aqueous superparamagnetic iron oxide nanoparticle as diagnostic agent, their encapsulation in the aqueous part of *Janus* nanoparticles and their characterizations.

2. Materials and Methods

2.1. Materials

Citrate coated-maghemite (FF-cit) was already synthesized in the laboratory [9]. Carboxymethyl Dextran (CMD, sodium salt, 15000 g.mol⁻¹, n = 69), poly(acrylic acid) (PAA,

sodium salt, $2100 \text{ g}\cdot\text{mol}^{-1}$, $n = 22$), and poly(acrylic acid-co-maleic acid) (PAAMA, 1:1 mole ratio of (acrylic acid):(maleic acid), solution ($3000 \text{ g}\cdot\text{mol}^{-1}$, 50 wt % in H_2O)) were purchased from Sigma Aldrich and used as received. Gelucire® 50/13 (stearoyl macroglycerides), Labrafil® M 2125 CS (linoleyl polyoxylglycerides), and Labrafil® M 1944 CS (oleyl polyoxylglycerides) were given by Gattefosse S.A.S. (Saint-Priest, France). Phospholipon® 90G (soybean lecithin at 94 – 102% of phosphatidylcholine) was provided by Phospholipid GmbH, Lipoid Group (Köln, Germany). Water was purified through a Milli-Q water system (Millipore, France). All other chemicals were of analytical grade or reagent grade.

2.2. Methods

2.2.1. Maghemite nanoparticles synthesis

Aqueous solutions of maghemite ($\gamma\text{-Fe}_2\text{O}_3$) were synthesized following Massart's coprecipitation method [10]. An acidic solution of ferric (FeCl_3) and ferrous (FeCl_2) chlorides was prepared. Ammonia was then added quickly to this solution in order to coprecipitate the iron cations into Fe_3O_4 (magnetite). After stirring and washing with nitric acid, a solution of ferric nitrate was added to the mixture. It was then boiled for 30 minutes in order to oxidize the magnetite into maghemite ($\gamma\text{-Fe}_2\text{O}_3$). This step is characterized by a change in the color of the particles which turn from black to red-brown. The resulting dispersion was then washed with acetone and ether before being redispersed in water to obtain the acidic FF. The maghemite nanoparticles prepared by the Massart process [10] have a zero charge point at pH 7.4. By acting on the pH, it will be possible to create positive charges at acidic pH by protonation of the surface hydroxyl groups or negative at basic pH by deprotonation of these same groups. In our case, we can obtain an acidic ferrofluid (pH 1.75) by adding nitric acid.

2.2.2. Maghemite nanoparticles coating

Bare nanoparticles are easily destabilized by an increase in ionic strength. To stabilize the particles at pH 7, it is necessary to complex a molecule which will confer a negative charge on the particles to the surface of iron atoms. Among the most effective complexing agents, molecules having carboxylate groups are able to strongly form coordination links with iron atoms. Citrate ions (Figure 3.1) are among the ligands most commonly used to functionalize maghemite nanoparticles in order to stabilize them on complementary pH ranges compared with naked nanoparticles [11,12]. Indeed, the citrate molecules exhibit a negative charge when the pH is sufficiently basic so that the carboxylic acid functional groups of the uncomplexed

citric acid are deprotonated. Thus, the stabilization of the maghemite-based colloid at pH 7 is based on the electrostatic repulsion of the nanocrystals through surface coating with negatively charged citrate anions.

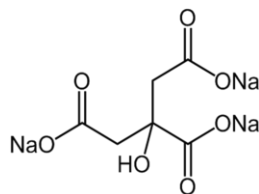


Figure 3.1. Sodium citrate

To prevent aggregation at neutral pH, the CMD, PAA and PAAMA polymers were used to stabilize the SPION. Carboxymethyl-substituted dextran (CMD) (Figure 3.2) is an anionic derivative of dextran commonly used as coating material for biosensors in both research and commercial settings due to its high density of carboxymethyl groups available for chemical conjugations [13]. Furthermore, the carboxymethyl groups allow for covalent fixation of the polymer to the maghemite surface which has a favorable impact on the nanoparticles colloidal stability [14]. Coating nanoparticles with polymers allows for colloidal stabilization through steric repulsion, which is less sensitive to the effects of high ionic strength of the biological medium than the citrated maghemite.

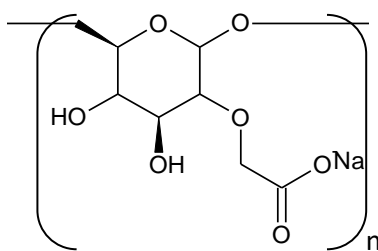


Figure 3.2. Sodium carboxymethyl dextran

CMD-coated maghemite (FF-CMD) was synthesized as follow : $1,25 \cdot 10^{-3}$ mol of CMD is added into an aqueous solution of acidic FF ($25 \cdot 10^{-3}$ mol) and heated at 150°C under magnetic stirring. After completion of the addition, the mixture is cooled to room temperature. pH of the solution is then adjusted to 3 with HCl. After one hour of stirring, pH is then ascended to 9 with tetramethylammonium hydroxide. One hour later, the solution pH is finally neutralized with HCl to obtain FF-CMD.

Polyacrylic acid chains (Figure 3.3) exhibit carboxylic acid functions carrying negative charges when deprotonated. Functionalization was carried out according to a detailed protocol in the literature [15,16]. This consists in adding a solution of naked nanoparticles at acid pH to a solution of polyacrylic acid previously adjusted to the same pH. The flocculate obtained is then redispersed with a basic solution of ammonium hydroxide to obtain the PAA-coated SPION (FF-PAA).

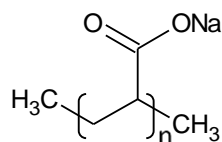


Figure 3.3. Sodium polyacrylate

The use of the poly(acrylic acid-co-maleic acid) copolymer (Figure 3.4) as coating is much less frequently reported in the literature. PAA and PAAMA are two polymers of relatively similar structures since acrylic and maleic acids have the same functional groups, only the distance between two groups differs from one polymer to another. The procedure followed to functionalize the particles with PAAMA (FF-PAAMA) is similar to that used for PAA.

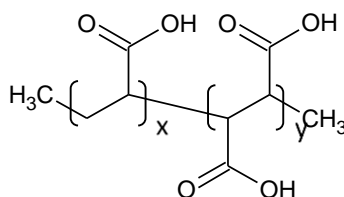


Figure 3.4. Poly(acrylic acid-co-maleic acid)

Both PAA and PAAMA coatings were performed by precipitation–redispersion following the procedure developed for PAA by Seghal [15] which will be described briefly here. First, if necessary, the pH of the polymer solution (1% wt) is adjusted to 2 with HNO_3 . An aqueous solution of acidic FF (1% wt) is then dripped into the polymer solution under stirring. The mixture is magnetically decanted and the supernatant is eliminated. NH_4OH is finally added until complete redispersion of the particles to obtain FF-PAA or FF-PAAMA.

2.2.3. Particle size

The particle size of nanodispersions was measured using a Nano-ZS90 apparatus (Malvern, Instruments, Orsay, France). The average hydrodynamic diameter and PDI were determined by QELS. The samples were diluted to 1/300 in Milli-Q water.

2.2.4. Thermogravimetric (TGA) analysis

Prior to TGA analysis, the FF was purified to remove unbound polymers. 1 mL of ferrofluid (FF) was dialyzed with a Micro DispoDIALYZER, 50 kDa, Sigma-Aldrich against 125 mL of water under stirring until the bulk density measured with a Beer Analyzer 2, Anton Paar densimeter was stable. Then 3 mL of the ferrofluid was freeze-dried with a COSMOS -80, Cryotec freeze-drier in 10 mL glass vial during 24 hours to obtain powder. Thermogravimetric analysis were done by TGA/DTA (SETARAM TG/DSC, Model 92-1750). Thermal analysis was used for the characterization of decomposition behaviour of freeze-dried SPION in order to quantify the iron oxide – coating mass ratio. These analyses have been done on 18-19 mg of freeze-dried SPION in a flowing air, from 40°C to 800°C, with a heating rate of 10 °C/min.

2.2.5. X-ray diffraction (XRD)

The data were collected at room temperature on a Rigaku D/max-B goniometer with a radius of 50 cm, associated with a Rigaku RA HF 18 rotating anode. The power of the X-ray generator was set to 50 kV and 200 mA. The K β ($\lambda = 1.392 \text{ \AA}$) copper radiation wavelength was selected through a monochromator. The powder, after grinding, was glued with vaseline on a home-made sample holder consisting of a silicon wafer. The scans were recorded with the following setting : 2-theta angle (2θ) from 0.5 to 50°, a step size of 0.02°, and a counting time of 2 seconds per step.

First, the Bragg peak positions were determined to identify the crystalline structure of the iron oxide. In a second time, the width of these peaks were measured in order to determine the crystalline size, meaning the diameter of the iron oxide core. Indeed, if they are small enough (<1 μm), the size of the crystallites and the shape of the XRD reflections are correlated by means of the Scherrer formula :

$$d = \frac{K\lambda}{width_{(rad)} \cdot \cos\theta}$$

where d is the crystallite size, λ is the wavelength of the radiation, θ is the angle of the considered Bragg reflection and K is a constant that has been generally fixed at 0.9 in the literature [17–19] (This value were used here).

2.2.6. Small-angles X-ray scaterings (SAXS)

Besides experiments with laboratory equipments, higher fluxes were necessary for some SAXS measurements. Time resolved combined small and wide-angle X-ray scattering experiments were then carried out at the Non Crystalline Diffraction beamline, BL-11 of the Alba synchrotron radiation light facility of Cerdanyola del Vallès (Catalonia, Spain). The energy of the incident photons was 10.0 keV, equivalent to a wavelength, λ , of 1.24 Å and the flux at the sample position was about 1012 photons per second. The SAXS diffraction pattern was collected by means of a CCD detector Quantum ADSC 210r with an active area of 210 × 210 mm² and an effective square pixel size of 103 mm with a depth of 16 bits. The sample-to-detector distance was set to about 2700 mm, resulting in a q range with a maximum value of 0.51 Å⁻¹. Additionally, the WAXS diffraction pattern was collected by means of a CCD detector Rayonix LX255-HS with an active area of 85 × 255 mm² and an effective square pixel size of 44 mm with a depth of 16 bits. In this case, the sample-to-detector distance was set to 139.0 mm, corresponding to a maximum q value of 6.41 Å⁻¹. This detector was tilt with a pitch of 26.7°. The exposure time, common to both detectors, was optimized in order to maximize the signal to noise ratio while avoiding detector saturation. Samples were confined in sealed quartz capillaries with an outside diameter of 1.6 mm and wall thickness of 0.01 mm and then insert in a Linkam HFSX-350-CAP hot stage with a temperature control within ± 0.1°C and connected to a cooling system of liquid nitrogen. Simultaneous SAXS and WAXS patterns were acquired while the samples were kept at fixed temperature or were heated from 20°C to 60°C at a controlled rate of 2°C.min⁻¹ depending on the experiments. In these experiments the scattering from water and that of the containing capillary was subtracted from the total scattering contribution. The data reduction was treated by pyFAI python code that is able to do azimuthal integrations from a previously calibrated file. The calibration files were created from well-known standards, i.e. Silver behenate and Cr₂O₃ for SAXS and WAXS respectively. The data were analyzed by using IgorPro 6 (Wavemetrics) to determine the Bragg reflection positions and AutoRg tool from the ATSAS suite (EMBL, Hambourg). AUTORG, is a command-line program to estimate the radius of gyration (R_g) using the Guinier approximation [20]. The value of R_g is estimated from the best possible linear fit of $\ln[I(s)]$ versus s^2 (Guinier plot) where s is

the scattering vector. This approximation is valid for sufficiently small scattering vectors (in the range up to $sR_g \leq 1.3$). The R_g provides an estimate of the overall size of a particle (the root mean square distance to center-of-mass in a particle) and is complementary to crystalline diameter (Scherrer calculations) and hydrodynamic diameter (DLS measurements).

2.2.7. Infra-red (IR) spectroscopy

The IR spectra of the sample were recorded using a Bruker IFS 125 Fourier transform spectrometer under vacuum, at the AILES beamline of SOLEIL synchrotron ring (Saint Aubin, France). Spectra were recorded at room temperature with a resolution of 4 cm^{-1} with 200 scans per spectrum using the ATR (attenuated total reflectance) technique with a single reflexion diamond crystal. The absorbance ($A = -\log(I/I_0)$) was calculated by taking as a reference I_0 the ATR system without any sample.

2.2.8. Preparation of magnetic nanodispersions by high-pressure homogenization process

7.7 mL of pre-heated (50°C) aqueous phase containing coated maghemite in the range 0,08-1,025M of iron, 2% (w/w) of Gelucire® 50/13 and 1% (w/w) of Phospholipon® 90G as surfactant was formed by using ultra-turrax (IKA® T10 basic, Germany) at 8500 rpm for 5 minutes. Thereafter, 2 g of lipid phase (Labrafil® M 2125 CS) was added to the water phase at the same temperature and formed a pre-dispersion at 20 000 rpm for 5 minutes. The resulting dispersion was homogenized at the same temperature by using a one stage high pressure homogenizer (Stansted Fluid Power Ltd, UK) during 4 passes at 1000 bars. The formulation was stored in glass vials and cooled down slowly to room temperature.

2.2.9. Transmission electron microscopy (TEM)

After synthesis, FF were diluted 2000 times. A droplet was then deposited on a carbon-coated copper grid and dried. FF were characterized with a JEOL 100-CX transmission electron microscope at 60 keV.

2.2.10. Cryogenic transmission electron microscopy (Cryo-TEM)

The morphology of nanodispersions was observed using a cryo-TEM system (JEM 2100, JEOL, Japan). All nanodispersions were diluted to 1/40 (v/v) in Milli-Q water. 10 μL of samples

were placed on a copper grid, and the solution excess was carefully removed by a filter paper. The vitrification of the film was achieved by rapidly plunging the grid into liquid ethane. The vitrified sample was then transferred to the microscope. The temperature was kept around -180°C during both the transfer and the viewing procedures in order to prevent sample perturbation and the formation of ice crystals.

2.2.11. Optical microscopy

Sample preparations were examined by microscopy in white light optical using a Nikon E600 Eclipse microscope (Champigny/Marne, France) equipped with a long focus objective (LWD 20 x 0.55; 0-2 mm). The images were recorded with a Mightex BCE 030-U camera at a resolution of 1024 x 768 pixels. The samples were prepared at 60°C, placed between two circular glass slides (26 mm thick) at the same temperature, observed in the 60-15°C range and monitored by a hotplate at heating or cooling rates of 2°C/min.

3. Results and Discussions

3.1. FF particle size

Table 3.1 describes the size and PDI of acidic ferrofluid, citrate, CMD, PAA and PAAMA-coated maghemite. FF-cit, FF-PAA and FF-PAAMA are very similar in size with a mean hydrodynamic diameter of 23.2, 23.1 and 22.5 nm respectively even if the type of the stabilization is very different.

Indeed, the first stabilization is electrostatic with the citrate ions only adsorb on the surface of the maghemite whereas the second coating is steric with the carboxylic functions of CMD, PAA and PAAMA complexed with the iron atoms of the maghemite. The hydrodynamic diameter of FF-CMD is three time larger than that measured with the other stabilizers probably due to the high molecular weight of the CMD used here (15000 g.mol⁻¹). Comparing the size of the nude maghemite (acidic FF) with that of the FF-PAA and FF-PAAMA, the layer of polymer coating the iron oxide grains can be estimated to be about 10 nm. The same size difference between before and after coating with the citrate ions is also observed even if citrates are small molecules compared to the polymers but this is explained by the presence of a solvation layer around the grains of maghemite. All these particles having size compatible with their incorporation in nanocarriers with size in the range 150-200 nm, they have been included in the FF selection strategy.

Table 3.1. Size and PDI of the FF-cit and the synthesized acidic FF, FF-CMD, FF-PAA and FF-PAAMA.

Ferrofluid	Size (nm)	PdI
Acidic FF	10.6 ± 2.9	0.405 ± 0.088
FF-cit	23.2 ± 8.6	0.116 ± 0.002
FF-CMD	60.2 ± 9.1	0.215 ± 0.034
FF-PAA	23.1 ± 6.9	0.303 ± 0.030
FF-PAAMA	22.5 ± 6.5	0.145 ± 0.010

3.2. FF selection strategy : FF vs. Process compatibility

First step of this work is to evaluate the compatibility between the high pressure homogenization (HPH) process and the use of ferrofluids. To determine it, a simple experiment consisting of subjecting the pure ferrofluid to the HPH process was carried out. Figure 3.5 showing the QELS profiles of the FF-PAA before and after HPH process doesn't indicate any significant difference between the two allowing us to state that the FF used is compatible with the HPH process.

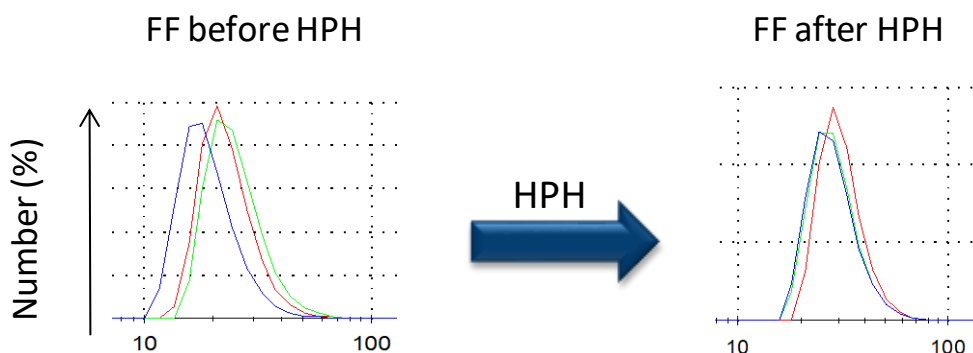


Figure 3.5. QELS profiles of FF-PAA before (left) and after (right) HPH process.

The next step is to appraise the feasibility and/or stability of the nanodispersion formulated with the different ferrofluids. To study this aspect, four different aqueous phases were prepared containing all Gelucire®, Phospholipon® and either FF-cit, FF-CMD, FF-PAA or FF-PAAMA. A lipid phase composed of PEG vegetable oils (Labrafil® M2125 CS) is added into the aqueous phase before being homogenized by HPH process. With the FF-cit and FF-CMD, unstable dispersions with the lipids of our preparation are obtained (Figure 3.6) but in the case of FF-

PAA and FF-PAAMA, macroscopically stable dispersions are obtained. Regarding the feasibility of the nanodispersions, PAA and PAAMA are the best stabilizers for further aqueous *Janus* encapsulation.



Figure 3.6. Nanodispersions obtained after HPH process with FF-cit (left), FF-CMD (middle) and FF-PAA or FF-PAAMA (right).

3.3. Characterization of FF-PAA and FF-PAAMA

3.3.1. Structural organization

Grains constituting these two ferrofluids were observed with transmission electron microscopy (Fig. 3.7). They are correctly dispersed and have similar shape and size distribution, confirming the QELS measurements.

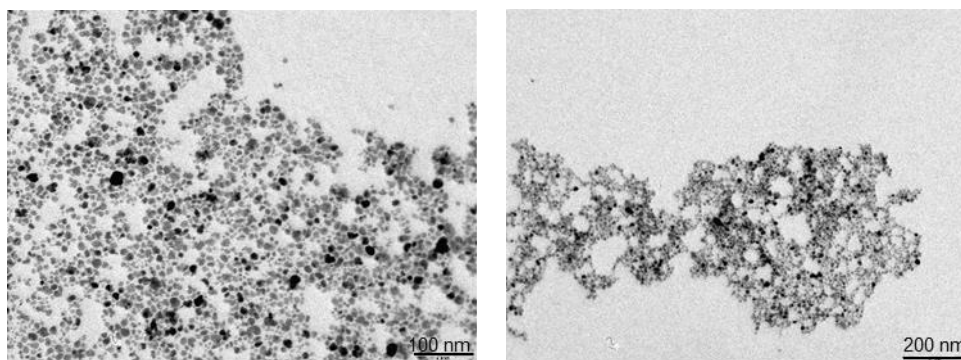


Figure 3.7. TEM views of FF-PAA (left) and FF-PAAMA (right).

Identification and crystal structure investigation of the freeze-dried powder samples FF-PAA and FF-PAAMA are based on the position of characteristic peaks in the diffractogram using the JCPDS data card 39-1346 [21]. An example of diffractogram is depicted on Figure 3.8 where FF-PAAMA presents more or less intense reflection at the following scattering angles (2θ): 16.2° , 27.4° , 32.1° , 38.9° and 48.2° . The Bragg peaks that can be attributed to specific diffraction planes inside the maghemite lattice are (111), (220), (311), (400) and (422).

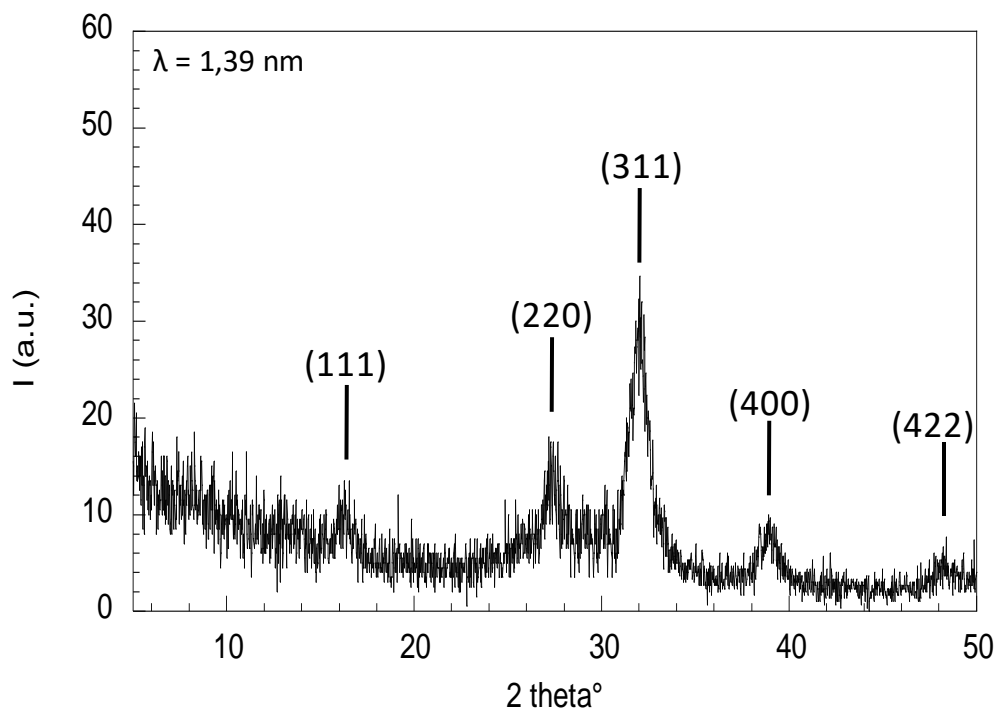


Figure 3.8. XRD pattern of FF-PAAMA.

Table 3.2 summarizes the most intensive reflections of the synthesized FF-PAA and FF-PAAMA in comparison with JCPDS data for maghemite (No. 39-1346) and magnetite (No 75_0033) [22]. As expected, synthesized FF-PAA and FF-PAAMA exhibit same diffraction patterns. The assembly of the diffraction peaks is indicative for a cubic inverse spinel structure [23]. The major oxides of iron, maghemite and magnetite, are structurally very similar (table 2). Theoretically, maghemite contains all the peaks of magnetite, with slight position shifts, and some additional very low intensity peaks corresponding to (110), (210) or (211) reflections at lower angles values. Because of the small size of the crystals and their low diffracted intensities, such additional peaks were not detected here and are probably included in the signal noise. Considering the peak positions, the (111) reflection does not fit perfectly the references. This could be due to its very weak intensity and to the inclined baseline which makes more difficult the fine detection of the position. The other peaks (220), (311), (400) and (422) fit better the Fe_2O_3 than the Fe_3O_4 reference. Even if the differences between the references are very slight in terms of peak positions, this parameter has been used in the literature to discriminate iron oxides [24,25] and strongly suggests here the presence of maghemite core. This is what is expected from the synthesis route.

Table 3.2. Indexation and peak position of the FF-PAAMA and FF-PAA diffractograms. Comparison with Fe_2O_3 and Fe_3O_4 references. The peak intensities are classified as weak (*w*), strong (*s*) and very strong (*vs*). * Unfortunately unexpected noise of the sample had disturbed the determination of this reflection position.

Indexation (hkl)	d (Å) (peak intensity)			
	FF-PAAMA	FF-PAA	Fe_2O_3 reference (JCPDS 39-1346)	Fe_3O_4 reference (JCPDS 75-0033)
(111)	4.93 (w)	4.93 (w)	4.82 (w)	4.84 (w)
(220)	2.94 (s)	2.94 (s)	2.95 (s)	2.96 (s)
(311)	2.52 (vs)	*	2.52 (vs)	2.53 (vs)
(400)	2.09 (s)	2.09 (s)	2.09 (s)	2.10 (s)
(422)	1.70 (w)	1.70 (w)	1.70 (w)	1.71 (w)

Freeze-dried powder diffraction patterns allows also to estimate the crystal size thank to Scherrer model (Table 3.3). Applied to all the reflections of the diffractograms, diameters of 13 ± 2 nm and 12 ± 2 nm could be estimated for FF-PAAMA and FF-PAA respectively. This is coherent with the hydrodynamic diameter of the acidic FF (Table 2.1) and with previous studies on uncoated magnetic nanoparticles prepared by the same protocol [26] which exhibited a TEM-diameter of 11.7 ± 3.7 nm.

Last size determination, the gyration diameter at infinite dilution has been obtained from synchrotron SAXS measurements on dilutions, from 0.03 wt% to 0.6 wt% of both FF. Values of 14.0 ± 0.2 nm and 14.4 ± 0.4 nm were determined for FF-PAAMA and FF-PAA respectively (Table 3.3). Gyration diameter are slightly larger than crystalline diameter but are strongly lower than the hydrodynamic diameter. This seems reasonable due to the density differences between the inorganic core and the organic polymer shell.

Table 3.3. Summary of the different diameters of the FF-PAAMA and FF-PAA grains.

Ferrofluid	Hydrodynamic diameter (nm)	Crystalline diameter (nm)	Gyration diameter (nm)
FF-PAA	23.1 ± 6.9	12 ± 2	14.4 ± 0.4
FF-PAAMA	22.5 ± 6.5	13 ± 2	14.0 ± 0.2

3.3.2. FTIR

Figure 3.9 shows the FTIR spectra of acidic FF, PAAMA polymer and FF-PAAMA freeze-dried powder. The characteristic absorption bands of the Fe-O bond of γ -Fe₂O₃ can be observed at 378 and 548 cm⁻¹ on the curve of FF-PAAMA that we find at 531 cm⁻¹ for the acidic FF (Table 3.3). The bands at 1185-1266 cm⁻¹ are attributed to the aliphatic acid. The most significant change in the PAAMA bands upon complexing is the appearance of two absorption bands at 1399 and 1549 cm⁻¹ respectively assigned to symmetric and asymmetric stretching vibration modes of the carboxylate group, which indicate the bidentate bonding of the carbonyl groups to the surface of iron atoms [27–29]. The two bands around 2900-3600 cm⁻¹ and 1624 cm⁻¹ on the acidic FF curve are ascribed to stretching and bending vibrations of surface hydroxyl groups, respectively [30]. In PAAMA curve characteristic stretching bands of carbonyl groups locates at 1636 and 1705 cm⁻¹ whereas it locates at 1694 cm⁻¹ on the FF-PAAMA curve, but its relative intensity is weaker than that of PAAMA. These results inform of the chemical reaction taking place between PAAMA and γ -Fe₂O₃ particles : PAAMA is directly coordinated with the surface of γ -Fe₂O₃. For the existing characteristic stretching band of carbonyl groups at 1694 cm⁻¹ and its decreasing intensity in FF-PAAMA curve, we can deduce that the carboxylic acid groups of PAAMA are bound to the surface of γ -Fe₂O₃ nanoparticles to form carboxylate groups [31]. The bands at 2937 and 2938 cm⁻¹ in Table 2.3 are attributed to C-H bonds. The last large bands at 3014-3712 and 3000-3636 cm⁻¹ correspond to the O-H stretching bond.

Table 3.3. IR band positions and assignments for acidic FF, PAAMA polymer and FF-PAAMA.

Assignment	Wavenumber (cm ⁻¹)		
	Acidic FF	PAAMA	FF-PAAMA
ν (Fe-O)	531	-	378 ; 548
ν (C-O)	-	1185-1266	1202
ν (COO ⁻) symmetric	-	-	1399
ν (COO ⁻) asymmetric	-	-	1549
ν (OH) bending	1624	-	-
ν (C=O)	-	1636 ; 1705	1694
ν (C-H)	-	2937	2938
ν (OH) stretching	2900-3600	3014-3712	3000-3636

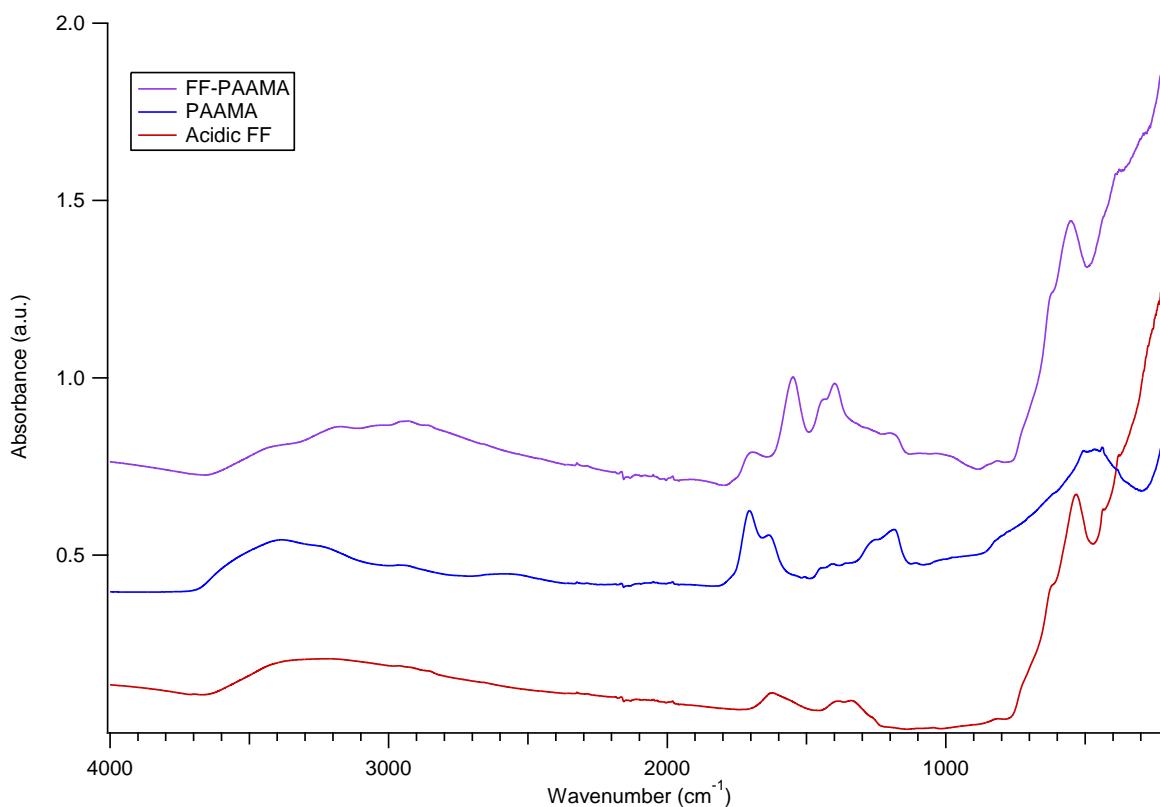


Figure 3.9. FTIR analysis of the acidic FF (red), the PAAMA polymer (blue) and the FF-PAAMA (purple).

Figure 3.10 presents the FTIR spectra of acidic FF, PAA polymer and FF-PAA. The characteristic absorption bands of the Fe-O bond of γ -Fe₂O₃ can be observed at 382 and 548 cm⁻¹ on the curve of FF-PAA that we find at 531 cm⁻¹ for the acidic FF (Table 3.4). The stretching frequency of C-O is found at 1320 cm⁻¹ for PAA and shifted at 1297 cm⁻¹ for FF-PAA. Our PAA sample is made of sodium polyacrylate, this mean that in this form the carboxylate functional groups of the polymer are fully ionized and the symmetric stretching frequency of the carboxylate ion are located at 1402 cm⁻¹ for both PAA and FF-PAA and 1548 cm⁻¹ whereas the antisymmetric stretching frequencies of COO⁻ are situated at 1548 cm⁻¹ and 1540 cm⁻¹ for PAA and FF-PAA respectively. CH₂ stretching bands are detected at 1453 cm⁻¹ and 2938 cm⁻¹ for both PAA and FF-PAA. The two bands around 2900-3600 cm⁻¹ and 1624 cm⁻¹ on the acidic FF curve are ascribed to stretching and bending vibrations of surface hydroxyl groups, respectively [30]. The last large bands at 3217-3389 cm⁻¹ and 3000-3636 cm⁻¹ correspond to the O-H stretching bond. In the literature, spectrum of sodium-free PAA has been described [32]. It is significantly different from our PAA but, interestingly, it owns similarities with our PAAMA which is sodium-free too confirming the analogy between the two polymers.

Table 3.4. IR band positions and assignments for acidic FF, PAA polymer and FF-PAA.

Assignment	Wavenumber (cm ⁻¹)		
	Acidic FF	PAA	FF-PAA
v (Fe-O)	531	-	382 ; 548
v (C-O)	-	1320	1297
v (COO ⁻) symmetric	-	1402	1402
v (CH ₂)	-	1453	1453
v (COO ⁻) asymmetric	-	1548	1540
v (OH) bending	1624	-	-
v (CH ₂)	-	2938	2938
v (OH) stretching	2900-3600	3217-3389	3000-3636

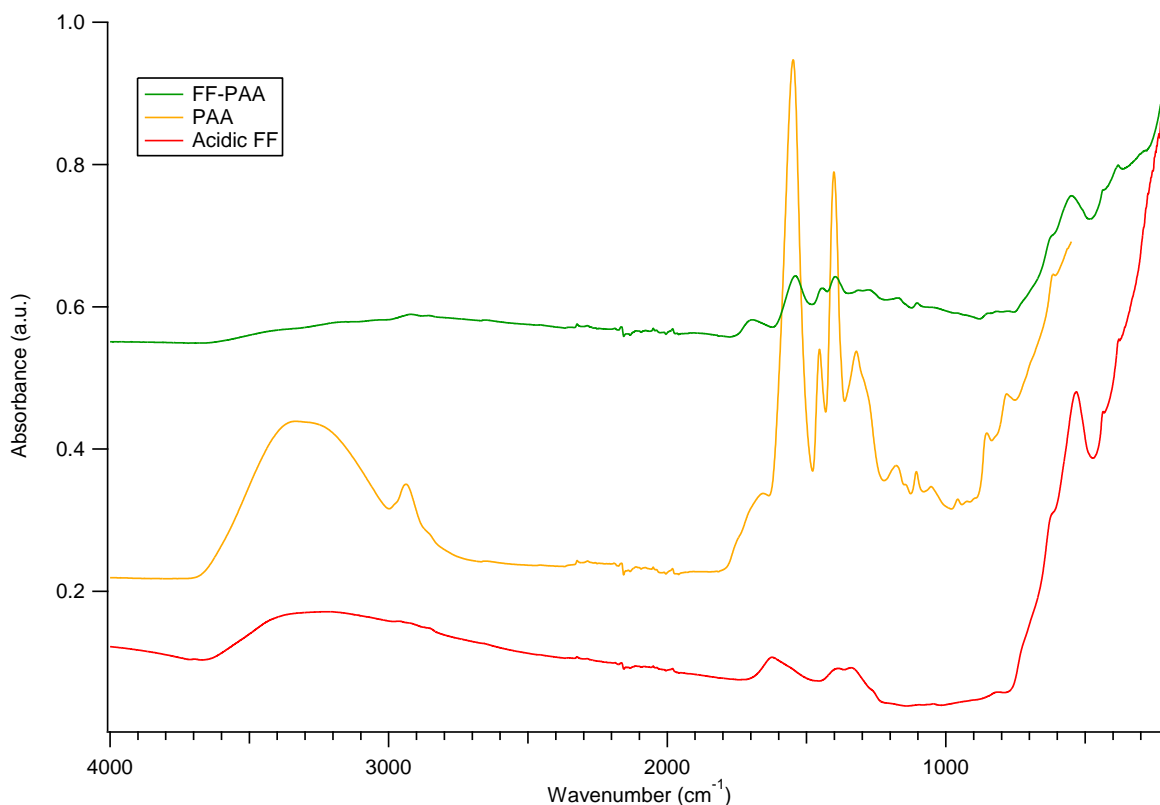


Figure 3.10. FTIR analysis of the acidic FF (red), the PAA polymer (orange) and the FF-PAA (green).

3.3.3. TGA

Figure 3.11 shows the TGA analysis of acidic FF, FF-PAAMA and FF-PAA. The acidic FF presents insignificant weight loss from 50 to 800°C. The TGA curve of FF-PAAMA shows two decomposition stages. The first step occurring near 200°C is due to dehydration caused by the destruction of polyelectrolyte complex between COO⁻ and NH₄⁺ leading to the formation of amide bonds [32]. The second step near 400°C concerns the degradation of PAAMA polymer. It can therefore be approximated that the loss of mass in FF-PAAMA originates from the polymer [32]. After the TGA analysis, 75 weight % of the FF-PAAMA is conserved. This result indicates that the weight ratio between the PAAMA polymer and the iron oxide (75%) is around 1:3. The TGA curve of FF-PAA also exhibits three stages of decomposition. The first-stage decomposition, which occurred near 200°C as for the FF-PAAMA, is also due to dehydration. Then the temperature is increased to 460°C to enable the main degradation of PAA polymer. The last decomposition stage which occurred at 620°C is due to the deoxidization of the γ -Fe₂O₃ particles, consisting in the FF as mentioned above, to form Fe₃O₄. After the TGA

analysis, 45 weight % of the FF-PAA is conserved. The weight ratio between the PAA polymer and the iron oxide (45%) is around 1:1.

The polymer – iron oxide ratios being significantly different between the two FF, these results should be discussed. From the TGA results and size determination, a stabilizer shell thickness can be calculated, using the radius of the nanocrystal core, r_c , (Scherrer calculation), the density ρ_c of $\gamma\text{-Fe}_2\text{O}_3$, the density of the shell, ρ_s , the shell weight, m_s , and the core weight, m_c . ρ_c and ρ_s could be obtained from the literature with respective values of 4.87 g/cm^3 [24,33] and $\sim 1.5 \text{ g/cm}^3$ [34]. The shell thickness, r_s , would be calculated from the following equation [35] :

$$r_s = \sqrt[3]{\frac{m_s \cdot r_c^3 \cdot \rho_c}{m_c} + r_c^3 \cdot \rho_s} - r_c$$

The shell thickness would be $\sim 1.8 \text{ nm}$ for FF-PAAMA and $\sim 3.7 \text{ nm}$ for FF-PAA. These results would lead to whole diameter $\sim 16.6 \text{ nm}$ and $\sim 19.4 \text{ nm}$ for anhydrous FF-PAAMA and FF-PAA respectively. Similar to the hydrodynamic diameter of the FF, the value for FF-PAAMA seems convincing. In the case of FF-PAA, the amount of polymer seems unfortunately too important, probably due to an incomplete purification.

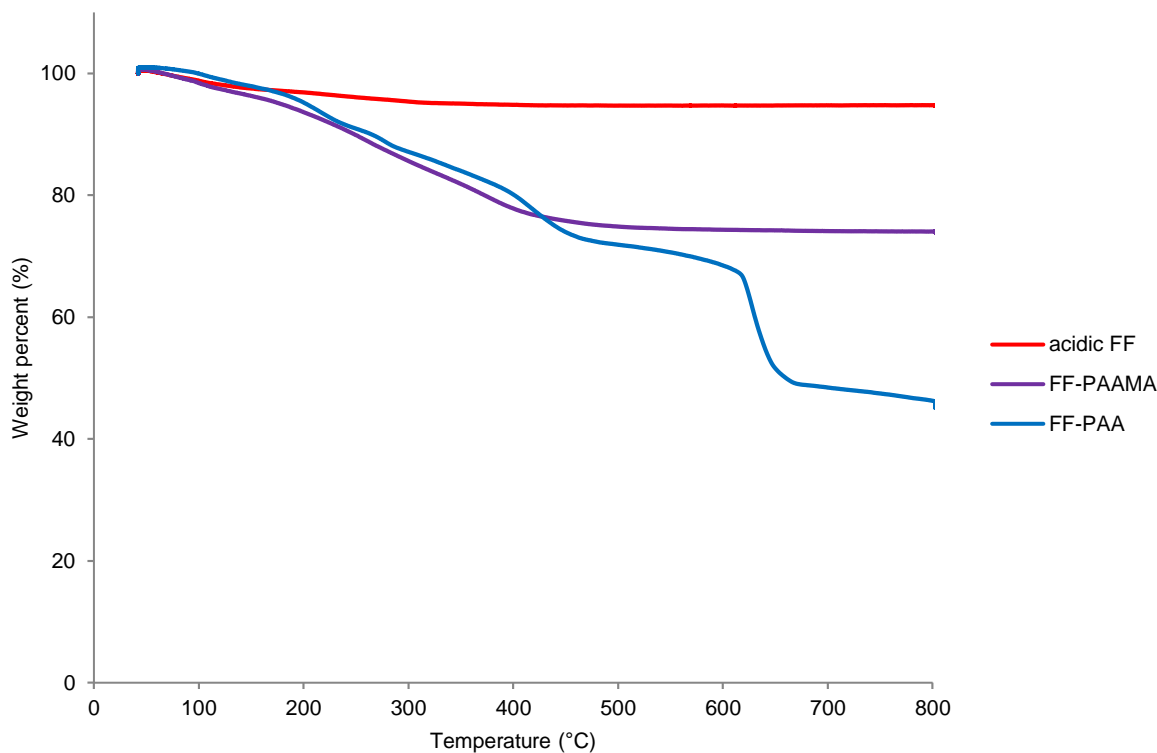


Figure 3.11. TGA analysis of the acidic FF (red), the FF-PAAMA (purple) and the FF-PAA (blue).

3.4. Incorporation trials in *Janus* nanoparticles

The purpose of this work is to encapsulate SPION in the aqueous part of *Janus* nanoparticles. To generate *Janus* nanoparticles, a HPH process is used by adding a lipid phase containing PEG vegetable oils (Labrafil® M2125 CS) into an aqueous phase made of phospholipids (Phospholipon® 90G), non-ionic surfactant (Gelucire® 50/13) and water. The first attempt is just to replace the water in the initial aqueous phase used in the conventional protocol by an aqueous phase containing FF in the range 0,08-1,025M of iron. The second test consists in changing the incorporation order that is to say to add the aqueous phase containing the FF into the lipid phase before homogenization. In the third trial, the aqueous FF is pre-incubated with the lipids and this lipid phase is then added into the classical aqueous phase before homogenization. The last trial was based on thin film hydration commonly used in the preparation of ML [9]. Indeed, a film of phospholipids and surfactants was prepared and then hydrated with an aqueous FF solution. The lipid phase is thereafter added in the previous aqueous phase before homogenization. In all cases, *Janus* nanoparticles can be obtained but as it can be observed on Figure 3.12, FF grains are still outside of the particles.

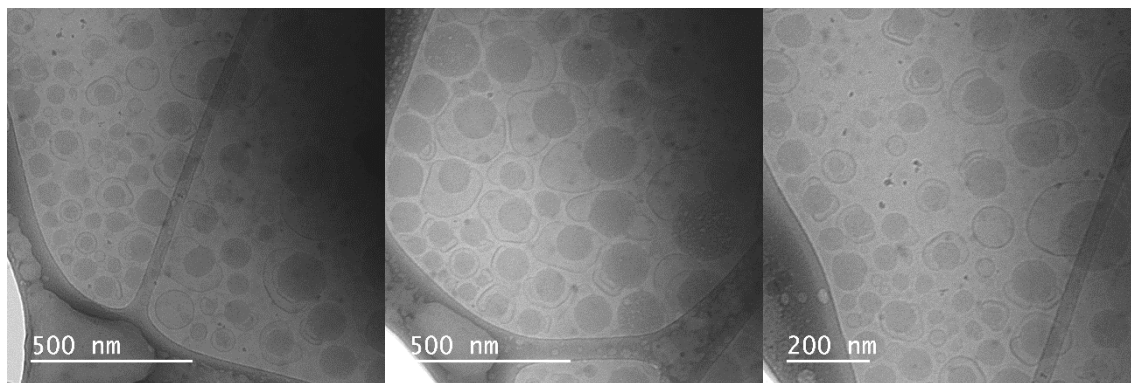


Figure 3.12. Cryo-TEM view of *Janus* nanoparticles.

3.5. Aqueous FF influency on the formation mechanism

3.5.1. SAXS experiments

As shown above, the incorporation of the aqueous FF inside the *Janus* nanoparticles has not been successful, justifying why it should be interesting to look for the influence of the aqueous FF on the phase separation that has been described as the driving-force of the *Janus* formation (Experimental chapter 1). To investigate this aspect, SAXS experiments were carried out on several mixtures containing all Labrafil® M2125 CS and either water, FF-PAAMA suspension or FF-PAA suspension (Figure 3.13). On the water hydrated Labrafil® X-ray diffraction pattern, a diffraction peak is detected into hydrated Labrafil characterizing a lamellar phase with a period of 97 Å at 20°C. This lamellar organization was previously described by Kunieda et al. in 1997 [36] who investigated the phase behaviour of poly(oxyethylene) unsaturated-C18 ether in water at room temperature. In chapter 1, the thickness of the lamellar phase was evaluated at 87 Å at 20°C. The 10 Å difference may originate from the composition of Labrafil® (complex mixture resulting from hemisynthesis of vegetable origin materials with great variability). Thus, the parameters which could influence the average thickness of this lamellar phase are : the saturated/monounsaturated/diunsaturated ratio of the fatty acid chains, the average length of the PEG chains and the monoester/diester ratio. General aspect of the diffractogram is more or less flat in the presence of water but the signal undergoes a strong rise to small q in the presence of FF. This can be explained by the diffusion signal related to the presence of grains in the FF (depending on the FF concentration, results not shown). If the Labrafil® is hydrated with both FF-PAAMA 3% and FF-PAA 3%, the diffraction peak is still present on the diffractogram but its position is shifted to the smallest distances with a period of 72 Å at 20°C.

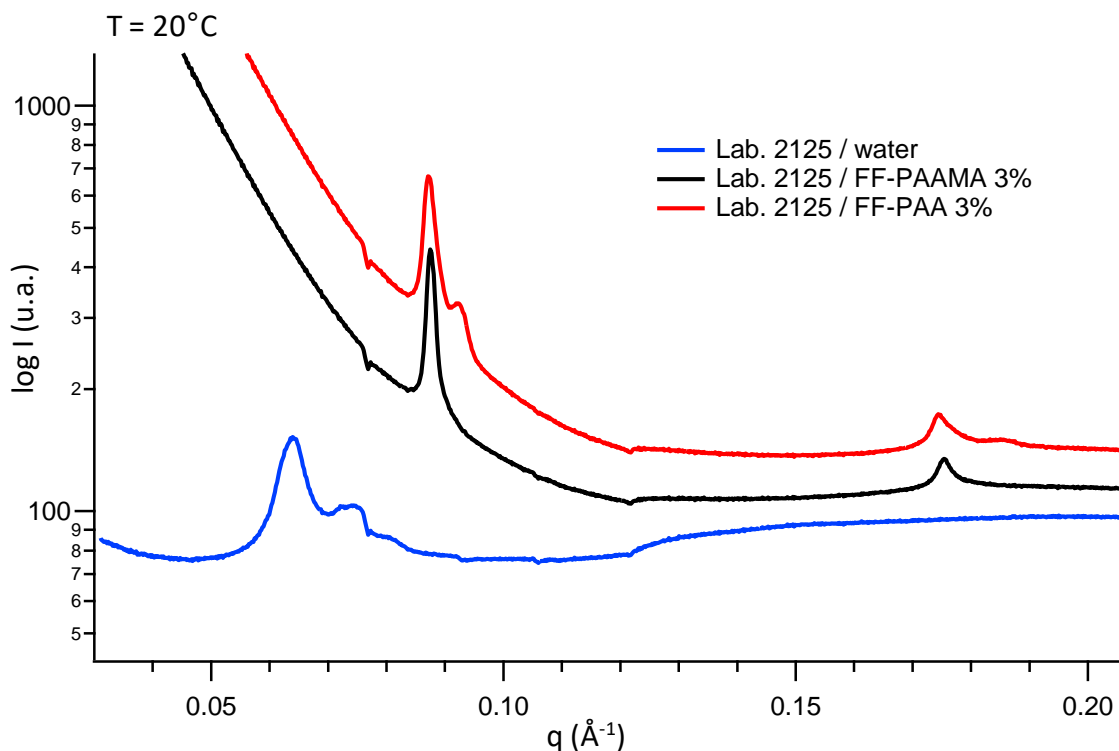


Figure 3.13. SAXS experiments on Labrafil® M2125 CS mixed with water (blue), FF-PAAMA (black) or FF-PAA (red).

By gradually increasing the iron concentration from 0% to 3% of the hydrating phase the thickness of the lamellar phase decreases from 97 Å to 72 Å respectively (Figure 3.14) but the lamellar organization is still conserved indicating that the incorporation of aqueous FF within a hydrated phase of Labrafil® is possible. If we figure out in term of mass ratio of the mixtures, then the more FF, the less water available to moisturize the Labrafil® surfactants involving a smaller thickness of the lamellar phase. Complementary experiments with pure water have shown that by modifying the hydration rate, from 10% to 5%, the lamellar thickness decreased to 81 Å² (data not shown) confirming the correlation between hydration and lamellar thickness. The result on Figure 3.14 also suggests that FF doesn't enter into these layers of hydrated surfactants. Indeed, considering the hydrodynamic diameter of the FF grains, if they were inserted between the bilayers, the thickness should increase very strongly with the concentration of FF. Furthermore, due to the thickness heterogeneities induced by the FF grains, the width of the diffraction peaks should increase and this lamellar phase should even completely destruct ; it's not the case here. The Labrafil® surfactants are on one side, the FF grains on the other side which create a competition between the two on water distribution. If some of the water is bound to the PAA and PAAMA coatings, it will moisturize less the surfactants.

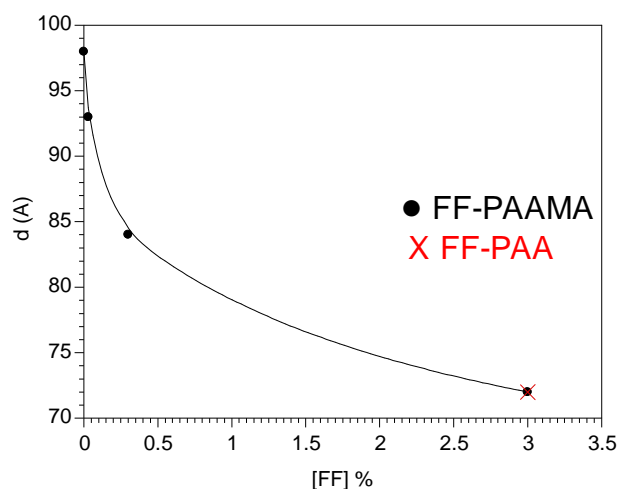


Figure 3.14. Evolution of the lamellar phase thickness as a function of the FF-PAAMA (black) or FF-PAA (red) concentration.

In the first part, it has been shown that with pure Labrafil® hydrated with water this lamellar organization is sensitive to the temperature and disappeared above 36°C that is why we try to determine if the same behaviour occurs when the moisturizing phase contains FF. An experiment was carried out on a mixture of Labrafil® M2125 CS with FF-PAA at 3% in a ratio of 9/1 by gradually increasing the temperature from 20°C to 48°C. The results summarized on Figure 3.15 show a shift of the diffraction peak to longer distances and its intensity decreases with the temperature raise.

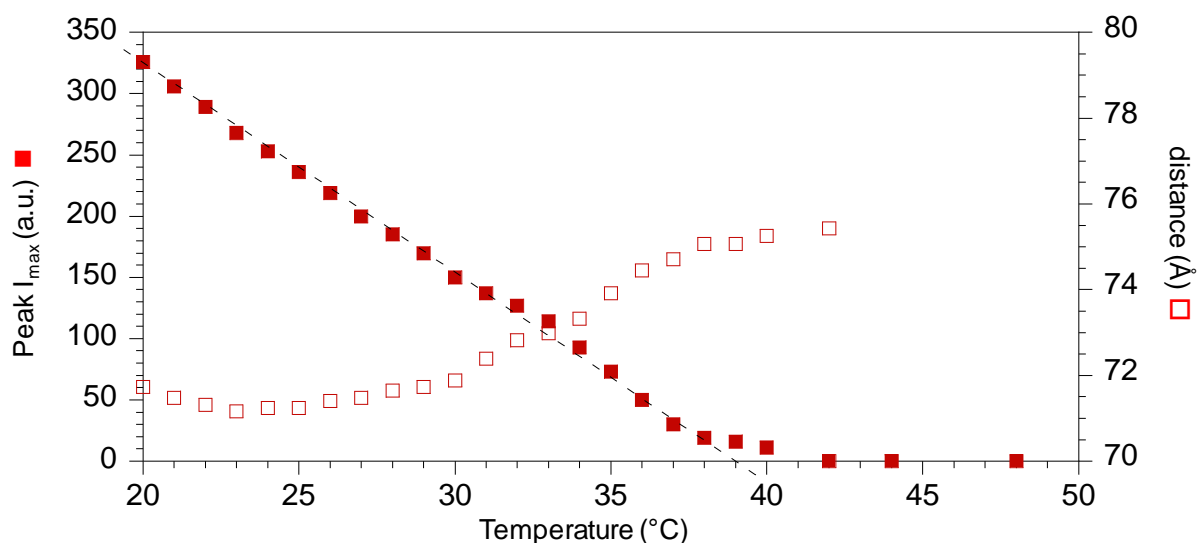


Figure 3.15. SAXS experiments on mixtures of Labrafil® M2125 CS and FF-PAA at 3% in a ratio 9/1 respectively under different temperatures, ■ intensity of the diffraction peak, □ position of the diffraction peak.

The same experiment was performed with several hydrating phases in which the iron concentration is progressively reduced (Table 3.4). The trend seems to indicate that the temperature of disappearance of the diffraction peak reduces with the diminution of the iron concentration and the lamellar organization is preserved at low temperatures (under 39°C). For pure Labrafil® M2125 CS the temperature of disappearance of the diffraction peak is estimated at 29°C, whereas a slight difference is observed with the result found in the first chapter (36°C) probably due to a variation in the composition of Labrafil® M2125 CS.

Table 3.4. Evolution of the temperature of disappearance of the lamellar phase peak in function of the iron concentration.

Hydrating phase	Temperature
FF-PAA 3%	39°C
FF-PAAMA 3%	39°C
FF-PAAMA 0.3%	34°C
FF-PAAMA 0.03%	30°C
Water	29°C

It is apparent from these results that the phase separation still occurs in presence of FF even if it modifies some parameters such as bilayer thickness or « transition » temperature. This confirms the cryo-TEM observations (Figure 2.12) that clearly shown the presence of *Janus* particles even if FF grains are incorporated into the aqueous phase. However, further experiments have been done to understand why the FF grains are not incorporated in these *Janus* particles.

3.5.2. Optical microscopy

Figure 3.16 describes the behaviour of an aqueous FF droplet in Labrafil® with temperature from 60°C to 14°C. When the temperature decreases from 60°C to 14°C at 2°C/min, a phase separation distinctly appears around the FF droplets.

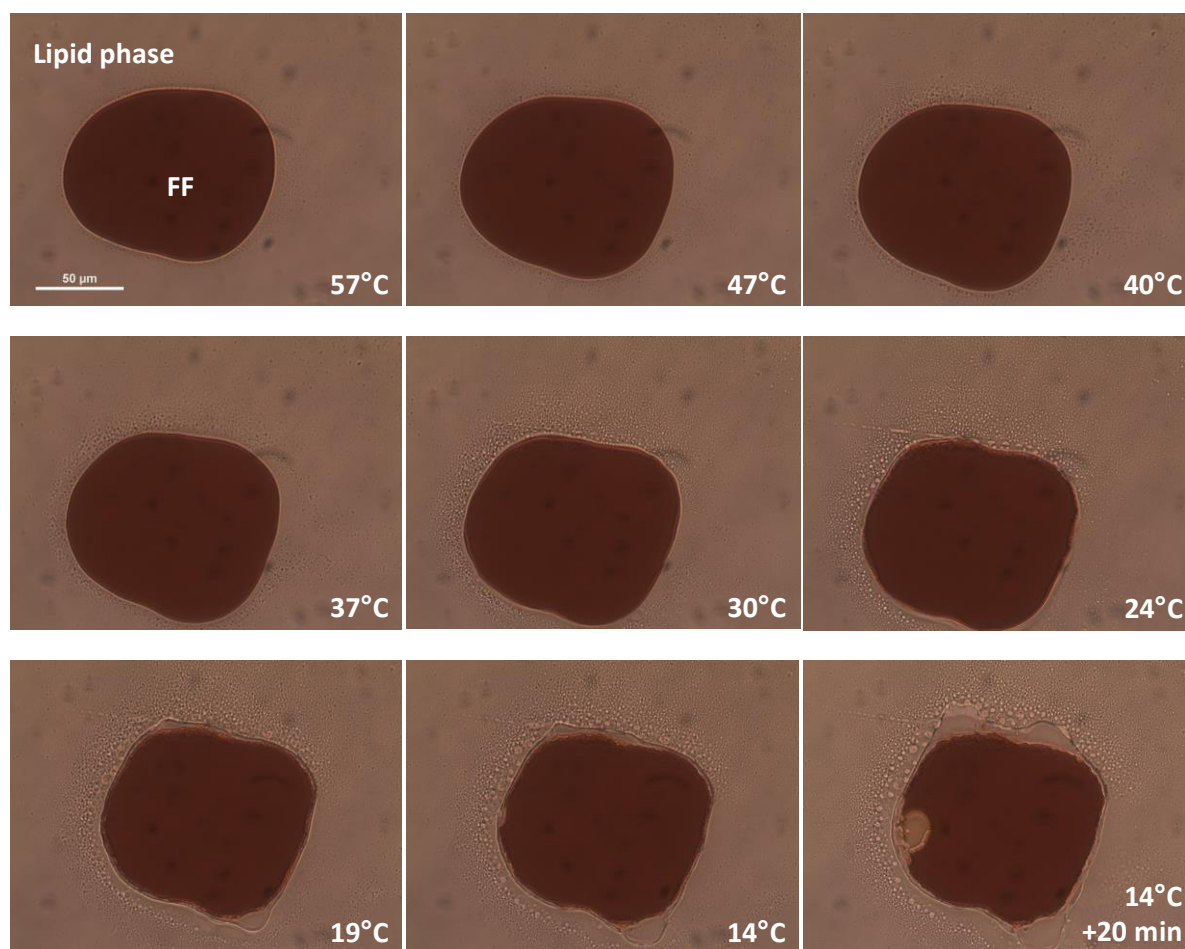


Figure 3.16. Optical microscopy pictures showing aqueous FF droplets into Labrafil® during cooling from 57°C to 14°C.

More precisely, the first step of this phase separation begins with the emergence of myelin figures which are visible at the FF – lipid interface at around 24°C (Figure 3.17). These figures are made of concentric bilayers obtained during the progressive hydration of lamellar structures that can be formed during the dissolution and swelling of surfactant lamellar phases [37]. The proposed mechanism of *Janus* nanoparticles formation is based on temperature dependant phase separation and the results of this experiment are in good agreement with the previous observations without FF. However, it is clearly apparent in these pictures that the new phase observed between FF and Labrafil® is certainly poor in FF grains as it do not described the typical brownish color of the iron oxide. This confirms the SAXS results suggesting the absence of mixing between FF grains and hydrated polyoxyglycerides. The most reasonable hypothesis to explain such results is the « particulate » state of the FF grains which would strongly limit their diffusion ability compared to water or surfactant molecules, consequently limiting the incorporation of FF into the aqueous compartment of the *Janus* nanoparticles.

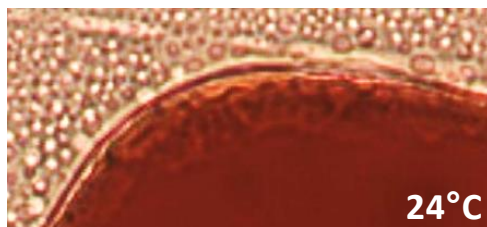


Figure 3.17 : Focus on myelin figures at 24°C.

When the temperature is then increased from 14°C to 50°C at 2°C/min (Figure 3.18), the phase separation reduces progressively the contact surface with the FF until complete dispersion in small drops in the lipid phase because the packing parameter of Labrafil® surfactants changes : close to 1 at room temperature ; > 1 at higher temperature, generating so-called inverse structures (small drops of water in lipid environment). This experiment corroborates the crucial role of the temperature already highlighted before.

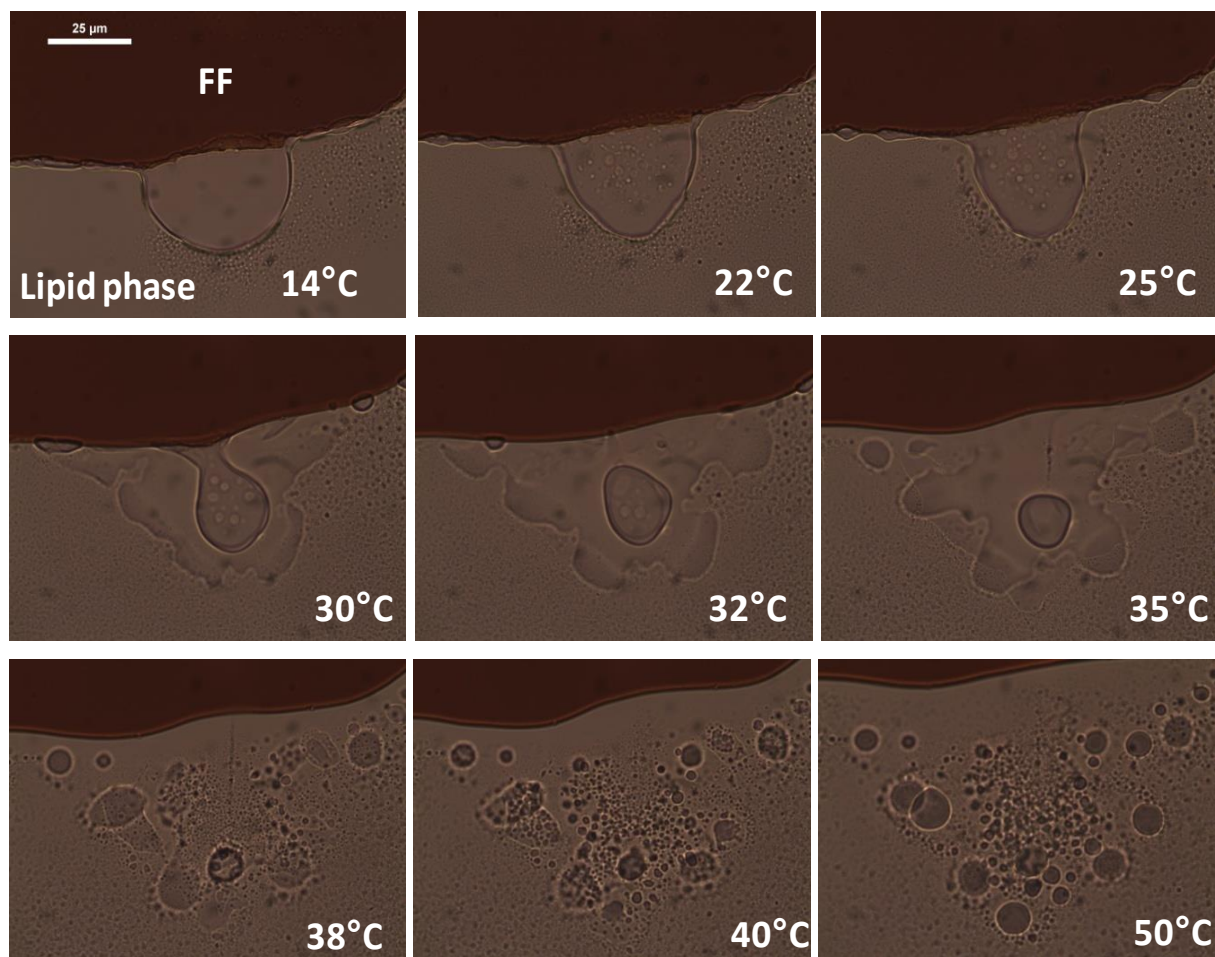


Figure 3.18. Optical microscopy pictures showing aqueous FF droplets into Labrafil® during heating from 14°C to 50°C.

4. Conclusion

This study describes the synthesis and characterizations of several aqueous superparamagnetic iron oxides nanoparticles for further encapsulation into the aqueous part of bicompartimented *Janus* nanoparticles. Polymer-stabilized maghemites were successfully prepared and the different analysis showed that the integrity of the iron oxide core is preserved after coating. Aqueous encapsulation trials were investigated, and data demonstrated that the maghemite grains are not incorporated into the *Janus* nanoparticles but the formation mechanism of these particles, based on a temperature dependent phase separation, is conserved in the presence of ferrofluid.

Two strategies should be now explored in order to load FF in the *Janus* nanoparticles. The first one is to try to incorporate the hydrophilic FF developed in the present work in preformed *Janus* nanoparticles thank to lyophilization or cooling/heating approaches that have been used sometimes to introduce large molecules into liposomes. The second way is to synthesize lipophilic FF and to investigate its incorporation into the lipid compartment of our anisotropic nanoparticles.

Acknowledgments

The authors would like to thank Ghislaine FREBOURG (Institut de Biologie Paris-Seine) for the cryo-TEM pictures.

References

- [1] Wang L-S, Chuang M-C, Ho JA. Nanotheranostics – a review of recent publications. *Int. J. Nanomedicine*. 2012;7:4679–4695.
- [2] Sumer B, Gao J. Theranostic nanomedicine for cancer. *Nanomed*. 2008;3:137–140.
- [3] Janib SM, Moses AS, MacKay JA. Imaging and drug delivery using theranostic nanoparticles. *Adv. Drug Deliv. Rev.* 2010;62:1052–1063.
- [4] Deveza L, Choi J, Yang F. Therapeutic Angiogenesis for Treating Cardiovascular Diseases. *Theranostics*. 2012;2:801–814.
- [5] Akbarzadeh A, Rezaei-Sadabady R, Davaran S, et al. Liposome: classification, preparation, and applications. *Nanoscale Res. Lett.* 2013;8:102.
- [6] Allen TM, Cullis PR. Liposomal drug delivery systems: From concept to clinical applications. *Adv. Drug Deliv. Rev.* 2013;65:36–48.
- [7] Al-Jamal WT, Kostarelos K. Liposomes: From a Clinically Established Drug Delivery System to a Nanoparticle Platform for Theranostic Nanomedicine. *Acc. Chem. Res.* 2011;44:1094–1104.
- [8] Bangham AD, Standish MM, Watkins JC. Diffusion of univalent ions across the lamellae of swollen phospholipids. *J. Mol. Biol.* 1965;13:238-IN27.
- [9] Martina M-S, Fortin J-P, Ménager C, et al. Generation of Superparamagnetic Liposomes Revealed as Highly Efficient MRI Contrast Agents for in Vivo Imaging. *J. Am. Chem. Soc.* 2005;127:10676–10685.
- [10] Massart R. Preparation of aqueous magnetic liquids in alkaline and acidic media. *IEEE Trans. Magn.* 1981;17:1247–1248.
- [11] Fauconnier N, Bee A, Roger J, et al. Synthesis of aqueous magnetic liquids by surface complexation of maghemite nanoparticles. *J. Mol. Liq.* 1999;83:233–242.

- [12] Fauconnier N, Bee A, Roger J, et al. Adsorption of gluconic and citric acids on maghemite particles in aqueous medium. *Trends Colloid Interface Sci. X.* 1996;212–216.
- [13] Ning S, Huang Q, Sun X, et al. Carboxymethyl dextran-coated liposomes: Toward a robust drug delivery platform. *Soft Matter.* 2011;7:9394.
- [14] Creixell M, Herrera AP, Latorre-Esteves M, et al. The effect of grafting method on the colloidal stability and in vitro cytotoxicity of carboxymethyl dextran coated magnetic nanoparticles. *J. Mater. Chem.* 2010;20:8539.
- [15] Sehgal A, Lalatonne Y, Berret J-F, et al. Precipitation–Redispersion of Cerium Oxide Nanoparticles with Poly(acrylic acid): Toward Stable Dispersions. *Langmuir.* 2005;21:9359–9364.
- [16] Fresnais J, Yan M, Courtois J, et al. Poly(acrylic acid)-coated iron oxide nanoparticles: Quantitative evaluation of the coating properties and applications for the removal of a pollutant dye. *J. Colloid Interface Sci.* 2013;395:24–30.
- [17] Monshi A, Foroughi MR, Monshi MR. Modified Scherrer Equation to Estimate More Accurately Nano-Crystallite Size Using XRD. *World J. Nano Sci. Eng.* 2012;02:154–160.
- [18] Smilgies D-M. Scherrer grain-size analysis adapted to grazing-incidence scattering with area detectors. Erratum. *J. Appl. Crystallogr.* 2013;46:286–286.
- [19] Patterson AL. The Scherrer Formula for X-Ray Particle Size Determination. *Phys. Rev.* 1939;56:978–982.
- [20] Petoukhov MV, Konarev PV, Kikhney AG, et al. ATSAS 2.1–towards automated and web-supported small-angle scattering data analysis. *Appl. Crystallogr.* 2007;40:s223–s228.
- [21] Cornell RM, Schwertmann U. *The Iron Oxides: Structure, Properties, Reactions, Occurrences and Uses.* John Wiley & Sons; 2003.
- [22] Cheng W, Tang K, Qi Y, et al. One-step synthesis of superparamagnetic monodisperse porous Fe₃O₄ hollow and core-shell spheres. *J. Mater. Chem.* 2010;20:1799.

- [23] Paterno LG, Fonseca FJ, Alcantara GB, et al. Fabrication and characterization of nanostructured conducting polymer films containing magnetic nanoparticles. *Thin Solid Films*. 2009;517:1753–1758.
- [24] Guivar JAR, Martínez AI, Anaya AO, et al. Structural and Magnetic Properties of Monophasic Maghemite (γ -Fe₂O₃) Nanocrystalline Powder. *Adv. Nanoparticles*. 2014;03:114–121.
- [25] Hai HT, Kura H, Takahashi M, et al. Facile synthesis of Fe₃O₄ nanoparticles by reduction phase transformation from α -Fe₂O₃ nanoparticles in organic solvent. *J. Colloid Interface Sci*. 2010;341:194–199.
- [26] Guibert C, Dupuis V, Peyre V, et al. Hyperthermia of Magnetic Nanoparticles: Experimental Study of the Role of Aggregation. *J. Phys. Chem. C*. 2015;119:28148–28154.
- [27] Vermöhlen K, Lewandowski H, Narres H-D, et al. Adsorption of polyacrylic acid on aluminium oxide: DRIFT spectroscopy and ab initio calculations. *Colloids Surf. Physicochem. Eng. Asp*. 2000;170:181–189.
- [28] Shukla N, Liu C, Jones PM, et al. FTIR study of surfactant bonding to FePt nanoparticles. *J. Magn. Mater*. 2003;266:178–184.
- [29] Liu Q, Xu Z. Self-assembled monolayer coatings on nanosized magnetic particles using 16-mercaptohexadecanoic acid. *Langmuir*. 1995;11:4617–4622.
- [30] Shan Z, Yang W-S, Zhang X, et al. Preparation and characterization of carboxyl-group functionalized superparamagnetic nanoparticles and the potential for bio-applications. *J. Braz. Chem. Soc*. 2007;18:1329–1335.
- [31] Moore RGC, Evans SD, Shen T, et al. Room-temperature single-electron tunnelling in surfactant stabilised iron oxide nanoparticles. *Phys. E Low-Dimens. Syst. Nanostructures*. 2001;9:253–261.
- [32] Lin C-L, Lee C-F, Chiu W-Y. Preparation and properties of poly(acrylic acid) oligomer stabilized superparamagnetic ferrofluid. *J. Colloid Interface Sci*. 2005;291:411–420.

- [33] Goloverda G, Jackson B, Kidd C, et al. Synthesis of ultrasmall magnetic iron oxide nanoparticles and study of their colloid and surface chemistry. *J. Magn. Magn. Mater.* 2009;321:1372–1376.
- [34] Hiraoka K, Shin H, Yokoyama T. Density measurements of poly (acrylic acid) sodium salts. *Polym. Bull.* 1982;8:303–309.
- [35] von der Lühe M, Günther U, Weidner A, et al. SPION@polydehydroalanine hybrid particles. *RSC Adv.* 2015;5:31920–31929.
- [36] Kunieda H, Shigeta K, Ozawa K, et al. Self-Organizing Structures in Poly(oxyethylene) Oleyl Ether-Water System. *J. Phys. Chem. B.* 1997;101:7952–7957.
- [37] Reissig L, Fairhurst DJ, Leng J, et al. Three-Dimensional Structure and Growth of Myelins. *Langmuir.* 2010;26:15192–15199.

INCORPORATION OF HYDROPHOBIC FERRO-FLUIDS INTO LIPID-BASED JANUS NANOPARTICLES

Elodie MILLART¹, Aude MICHEL², Jean-Blaise BRUBACH³, Christine MENAGER²,
Sylviane LESIEUR¹, Vincent FAIVRE^{1*}

¹ Institut Galien Paris-Sud, Université Paris-Saclay, Univ. Paris-Sud, Labex LERMIT ;
5 rue Jean-Baptiste Clément, 92296 Châtenay-Malabry, France

² Laboratoire PHENIX, Sorbonne Universités, UPMC, Université Paris 06, UMR CNRS 8234,
4 place Jussieu 75005 Paris, France

³ Ligne AILES, Synchrotron SOLEIL,
L'Orme des Merisiers Saint-Aubin, 91192 Gif-sur-Yvette Cedex

* Corresponding author

Tel. : +33 146835465; Fax: +33 146835312.

E-mail address : vincent.favre@u-psud.fr (Vincent FAIVRE).

ABSTRACT

In recent years, various nanotechnology platforms in the field of drug delivery have attracted important attention and, in particular, the magnetic nanoparticles have gained an unavoidable place in both diagnostics and therapy. This article describes the preparation and characterization of hydrophobic ferrofluids for their encapsulation in the lipid compartment of lipid-based *Janus* nanoparticles. Physico-chemical analysis permitted to choose the best lipid stabilizer for maghemite. Magnetic *Janus* nanoparticles were successfully prepared using a scalable process with pharmaceutically approved excipients. Further magnetic experiments demonstrated the superparamagnetic behavior of this innovative system.

KEYWORDS

Accumulation, Beycostat N B09, compartmented lipid nanoparticles, cryo-transmission electron microscopy, ferrofluid, Fourier-transform infrared spectroscopy, *Janus* lipid nanoparticles, high pressure homogenization, maghemite, magnetization, oleic acid, relaxometry, small-angle x-ray diffraction, SPION

1. Introduction

Nanoemulsions, defined as liquid-liquid biphasic dispersions at the nanometer scale, have growing interest as colloidal drug carriers, especially for intravenous administration, from parenteral nutrition to drug transportation [1–3], or for oral administration of poorly water-soluble drugs since they have been demonstrated to enhance drug bioavailability through the improvement of the intestinal absorption [4]. Furthermore, the specific advantages of NE over other nanotechnologies used for drug delivery, are their high loading capacity for lipophilic drug, formulation stability, ease of manufacture and their relatively low complexity [5]. Pharmaceutically used and approved NE are mostly composed of an oil phase dispersed in a continuous aqueous phase as droplets with submicronic size, preferentially with maximum radius below 200 nm [5]. Oil-in-water emulsions are an example of a nanoparticle platform that is capable of carrying both a high payload of hydrophobic materials in their core and eventually amphiphilic payload in their surfactant corona [6,7]. These materials could be active API [8–12] for therapeutic purposes or diagnostic agents such as SPION [13–17]. Furthermore, the co-encapsulation of both types of ingredient, for theranostic applications, has been extensively described in the literature [6,18–20] and seems to be of great interests for biomedical uses. However, even if they are easy to produce, NE-based systems have some limitations. First, they could not incorporate hydrophilic entities. Second, the solvent property of their constituting oils is often limited for molecules of interest. This solubilization limit is more pronounced in the field of coencapsulation as a competition between the two or more molecules can occur and reduce drastically the encapsulation rates. In order to overcome this drawback, bicompartmented lipid-based *Janus* nanoparticles have been developed. They are composed of a lipid compartment, an aqueous compartment and a lipid bilayer made of compounds FDA-approved. The two distinct sides of the *Janus* nanoparticles make them very interesting objects for the co-administration of two API with opposite solubilities. In the present work, we investigated the development of lipid superparamagnetic iron oxide nanoparticle as diagnostic agent, their encapsulation in the lipid part of *Janus* nanoparticles, their characterizations and potential applications in MRI and magnetic guidance.

2. Materials and Methods

2.1. Materials

All chemical reagents were purchased from Sigma-Aldrich, France and used as received. Beycostat N B09 was provided by CECA S.A., France. Oleic acid (OA, $282.46 \text{ g}\cdot\text{mol}^{-1}$) was purchased from Sigma-Aldrich. Gelucire® 50/13 (stearoyl macroglycerides), Labrafil® M 2125 CS (linoleyl polyoxyglycerides), and Labrafil® M 1944 CS (oleyl polyoxyglycerides) were given by Gattefosse S.A.S. (Saint-Priest, France). Phospholipon® 90G (soybean lecithin at 94 – 102% of phosphatidylcholine) was provided by Phospholipid GmbH, Lipoid Group (Köln, Germany). Water was purified through a Milli-Q water system (Millipore, France).

2.2. Methods

2.2.1. Maghemite nanoparticles synthesis

Aqueous solutions of maghemite ($\gamma\text{-Fe}_2\text{O}_3$) were synthesized following Massart's coprecipitation method [21]. An equimolar acidic solution of ferric (FeCl_3) and ferrous (FeCl_2) chlorides was prepared. Ammonia was then added quickly to this solution in order to coprecipitate the iron cations into Fe_3O_4 (magnetite). After stirring and washing with nitric acid, a solution of ferric nitrate was added to the mixture. It was then boiled for 30 minutes in order to oxidize the magnetite into maghemite ($\gamma\text{-Fe}_2\text{O}_3$). This step is characterized by a change in the color of the particles which turn from black to red-brown. The resulting dispersion was then washed with acetone and ether before being redispersed in water to obtain the acidic FF. The maghemite nanoparticles prepared by the Massart process [21] have a zero charge point at pH 7.4. By acting on the pH, it will be possible to create positive charges at acidic pH by protonation of the surface hydroxyl groups or negative at basic pH by deprotonation of these same groups. In our case, we can obtain an acidic ferrofluid (pH 1.75) by adding nitric acid.

2.2.2. Maghemite nanoparticles coating

Two types of functionalization were studied : oleic acid (OA) and Beycostat N B09 (BNE) coatings. OA is a biocompatible fatty acid and also an agent inducing the stability of many particle systems. It can play a role of a capping agent for the particles to form a protective monolayer through a strong bond. Nanoparticles with a hydrophobic coating through the attachment of the polar end groups (Figure 4.1) to the surface hence are obtained by mixing nude maghemite with OA at high temperature to form FF-OA.

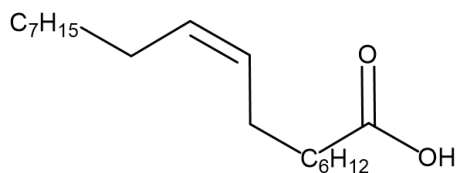


Figure 4.1. Oleic acid.

BNE is a phosphoric diester like anionic surfactant (Figure 4.2). It is directly adsorbed on the acidic FF. This surfactant makes possible the dispersion of the particles in many solvents like chloroform, phthalates, aromatics (benzene, styrene, toluene, ...), some silicone oils possessing aromatic rings (Rhodorsil 763), chlorinated solvents (CCl_4 ...), ether and many commercial oils.

For both stabilizers, adsorption of surfactants is performed in aqueous medium according to the general following procedure. 20 mol% of OA is mixed with the aqueous magnetic fluid and 20 mol% of NH_3 at $100^\circ C$ for 30 minutes. The obtained precipitate is separated from the supernatant by magnetic decantation and then washed three times with methanol. Methanol is removed by magnetic decantation. The same procedure is used with BNE : 200 g of BNE is mixed with the aqueous magnetic fluid and 200 mL of HNO_3 2M at $100^\circ C$ for 30 minutes. The obtained precipitate is separated from the supernatant by magnetic decantation and then washed three times with ethanol. Ethanol is removed by magnetic decantation and then heated to $90^\circ C$. All the particles are finally redispersed in chloroform to reach an iron-concentration of 1M.

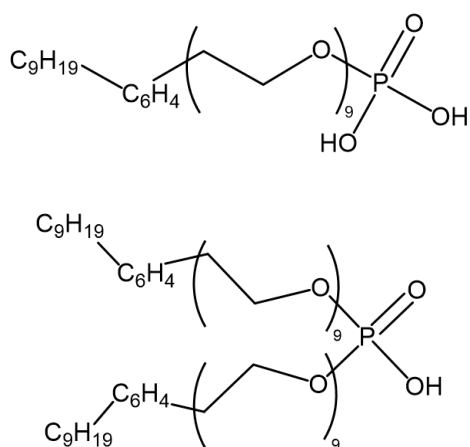


Figure 4.2. Phosphoric diester like anionic surfactant.

2.2.3. Infra-red (IR) spectroscopy

The IR spectra of the sample were recorded using a Bruker IFS 125 Fourier transform spectrometer under vacuum, at the AILES beamline of SOLEIL synchrotron ring (Saint Aubin, France). After solvent evaporation directly on the crystal, spectra were recorded with a resolution of 4 cm^{-1} with 200 scans per spectrum using the ATR (attenuated total reflectance) technique with a single reflexion diamond crystal. The absorbance ($A = -\log(I/I_0)$) was calculated by taking as a reference, I_0 , the ATR system without any sample.

2.2.4. SAXS ALBA

Time resolved combined small and wide angle X-ray scattering experiments were then carried out at the Non Crystalline Diffraction beamline, BL-11 of the Alba synchrotron radiation light facility of Cerdanyola del Vallès (Catalonia, Spain). The energy of the incident photons was 10.0 keV, equivalent to a wavelength, λ , of 1.24 \AA and the flux at the sample position was about 1012 photons per second. The SAXS diffraction pattern was collected by means of a CCD detector Quantum ADSC 210r with an active area of $210 \times 210\text{ mm}^2$ and an effective square pixel size of 103 mm with a depth of 16 bits. The sample-to-detector distance was set to about 2700 mm, resulting in a q range with a maximum value of 0.51 \AA^{-1} . Additionally, the WAXS diffraction pattern was collected by means of a CCD detector Rayonix LX255-HS with an active area of $85 \times 255\text{ mm}^2$ and an effective square pixel size of 44 mm with a depth of 16 bits. In this case, the sample-to-detector distance was set to 139.0 mm, corresponding to a maximum q value of 6.41 \AA^{-1} . This detector was tilt with a pitch of 26.7° . The exposure time, common to both detectors, was optimized in order to maximize the signal to noise ratio while avoiding detector saturation. Samples were confined in sealed quartz capillaries with an outside diameter of 1.6 mm and wall thickness of 0.01 mm and then insert in a Linkam HFSX-350-CAP hot stage with a temperature control within $\pm 0.1^\circ\text{C}$ and connected to a cooling system of liquid nitrogen. Simultaneous SAXS and WAXS patterns were acquired while the samples were kept at fixed temperature or were heated from 20°C to 60°C at a controlled rate of $2^\circ\text{C}\cdot\text{min}^{-1}$ depending on the experiments. In these experiments the scattering from water and that of the containing capillary was subtracted from the total scattering contribution. The data reduction was treated by pyFAI python code that is able to do azimuthal integrations from a previously calibrated file. The calibration files were created from well-known standards, i.e. Silver behenate and Cr_2O_3 for SAXS and WAXS respectively. The data were analyzed by using IgorPro 6 (Wavemetrics) to determine the Bragg reflection positions and tools from the ATSAS

suite (EMBL, Hambourg) to determine R_g of FF grains after their dispersion into Labrafil. First, AUTORG, a command-line program to estimate the R_g using the Guinier approximation, was used [22]. The value of R_g is estimated here from the best possible linear fit of $\ln[I(s)]$ versus s^2 (Guinier plot) where s is the scattering vector. This approximation is valid for sufficiently small scattering vectors (in the range up to $sR_g \leq 1.3$). In a second time, an evaluation of the particle distance distribution function, $p(r)$, was made to estimate R_g from the whole scattering signals. Second, AUTOGNOM automatically gives the distance distribution $p(r)$ function and R_g from the indirect Fourier transform of the whole scattering profile repeatedly using a regularization procedure implemented in the program GNOM. [9]

2.2.5. Preparation of magnetic nanodispersions by high-pressure homogenization process

7.7 mL of pre-heated (50°C) aqueous phase containing 2% (w/w) of Gelucire® 50/13 and 1% (w/w) of Phospholipon® 90G as surfactant was formed by using ultra-turrax (IKA® T10 basic, Germany) at 8500 rpm for 5 minutes. 2.5 g of FF-BNE in CHCl_3 were mixed with Labrafil® M 2125 CS or Labrafil® M1944 CS under vacuum to evaporate the CHCl_3 . Thereafter, 2 g of lipid phase containing Labrafil® M 2125 CS or Labrafil® M1944 CS and BNE-coated maghemite was added to the water phase at the same temperature and formed a pre-dispersion at 20 000 rpm for 5 minutes. The resulting dispersion was homogenized at the same temperature by using a one stage high pressure homogenizer (Stansted Fluid Power Ltd, UK) during 4 passes at 1000 bars. The final dispersions were stored in glass vials and cooled down slowly to room temperature.

2.2.6. Purification step

Separation of free FF-BNE non-entrapped into *Janus* nanoparticles was performed by centrifugation (Hettichzentrifugen, MIKRO 200, Germany). Centrifugation of 3 mL of sample at 7000 rpm for 20 min leads to two distinct phases : a very dark bottom phase and a supernatant phase. This operation is repeated twice more on the supernatant.

2.2.7. Iron assay

ICP-AES was performed on a Thermofisher iCAP6200 with a HNO_3 2% matrix. Samples were diluted 20000 times.

2.2.8. Drug loading (DL) and entrapment efficiency (EE)

The SPION loading (SpL) and the entrapment efficiency (EE) could be calculated by the following equations:

$$SpL (\%) = \left(\frac{W_{total\ of\ encapsulated\ SPION}}{W_{total\ of\ lipid}} \right) \times 100 \quad (1)$$

$$EE (\%) = \left(\frac{W_{total\ of\ encapsulated\ SPION}}{W_{total\ of\ SPION\ added}} \right) \times 100 \quad (2)$$

where, $W_{total\ of\ encapsulated\ SPION}$, $W_{total\ of\ SPION\ added}$ and $W_{total\ of\ lipid}$ were the weight of SPION encapsulated into nanoparticles, the initial weight of SPION in the formulation, and weight of lipid in system, respectively. Previous unpublished experiments showing that less than 5% of the initially weighted lipids were lost during the preparation process, the final lipid amount in the suspension was assimilated to the initial amount. The different weights of SPION were calculated from the iron assay results.

2.2.9. Particle size

Nanodispersions were stored at room temperature (20-23°C) for 8 months. The particle size of nanodispersions was measured using a Nano-ZS90 apparatus (Malvern, Instruments, Orsay, France). The average hydrodynamic diameter and Pdl were determined by QELS. The samples were diluted to 1/300 in Milli-Q water.

2.2.10. Cryogenic transmission electron microscopy (Cryo-TEM)

The morphology of nanodispersions was observed using a cryo-TEM system (JEM 2100, JEOL, Japan). All nanodispersions were diluted to 1/40 (v/v) in Milli-Q water. 10 μ L of samples were placed on a copper grid, and the solution excess was carefully removed by a filter paper. The vitrification of the film was achieved by rapidly plunging the grid into liquid ethane. The vitrified sample was then transferred to the microscope. The temperature was kept around -180°C during both the transfer and the viewing procedures in order to prevent sample perturbation and the formation of ice crystals.

2.2.11. Magnetic measurement

Magnetic characterizations were made on a vibrating sample magnetometer (home-made apparatus). Each analysis was performed with 1.5 mL of purified magnetic *Janus* nanodispersions and FF-BNE dispersed in Labrafil® at 25°C from 0 to 9000 Gauss. Data were analyzed using the Langevin function of paramagnetism convoluted with a log-normal distribution function of the particle sizes.

2.2.12. Relaxometry

Relaxation times were measured at 0.9 T using a Minispec MQ20 spectrometer (Bruker, France) thermostated at 25°C with a Julabo F25 bath. T_1 and T_2 were determined three times for each sample. Each analysis was performed with 1 mL of the purified magnetic *Janus* nanodispersions at five dilutions ranging from 1/10 to 1/60.

2.2.13. Magnetic accumulation : preliminary test

Magnetic guidance would result on a local accumulation of the loaded-particles when a magnet is applied in the region of interest. A preliminary and rudimentary experiment has been done by placing a magnet in front of an Eppendorf tube containing a dilution of *Janus* particles loaded with FF-BNE.

3. Results and Discussion

3.1. Characterizations

3.1.1. FT-IR

3.1.1.1. Oleic acid

The FT-IR spectra of the acidic FF, the OA and the OA-coated maghemite samples investigated here, in the 500-4000 cm^{-1} range, are presented in Figure 4.3. The characteristic absorption band of the Fe-O bond of $\gamma\text{-Fe}_2\text{O}_3$ can be observed at 537 cm^{-1} on the curve of FF-OA that we find at 531 cm^{-1} for the acidic FF. On the OA curve, the O-H out-of-plane band appears at 937 cm^{-1} . A strong absorption at around 1050 cm^{-1} for OA and shifted to 1284 cm^{-1} for FF-OA emerges from C-O single bond stretching revealing that OA is chemisorbed onto the maghemite nanoparticle surface as carboxylates [23]. For FF-OA, the carboxylate bound to maghemite nanoparticle surface shows symmetric (COO^-) stretching band at 1405 cm^{-1} and asymmetric (COO^-) stretching bands at 1522 cm^{-1} . The wave number separation between the symmetric (–

COO) and anti-symmetric ($-\text{COO}$) IR bands is 117 cm^{-1} , which is attributed to a chelating bidentate configuration where the COO^- group forms a covalent bond with the Fe atom [23]. The intensity of the C=O stretch band (1710 cm^{-1}) of the carboxyl group of the FF-OA, which is present at 1708 cm^{-1} in pure OA (Table 3.1), is considerably affected. Compared to the pure OA, the asymmetric CH_2 stretch shift to a lower frequency region, around 2918 cm^{-1} and the symmetric CH_2 stretch shift to 2849 cm^{-1} , indicating that the hydrocarbon chains in the monolayer surrounding the nanoparticles were in a close-packed, crystalline structure [23].

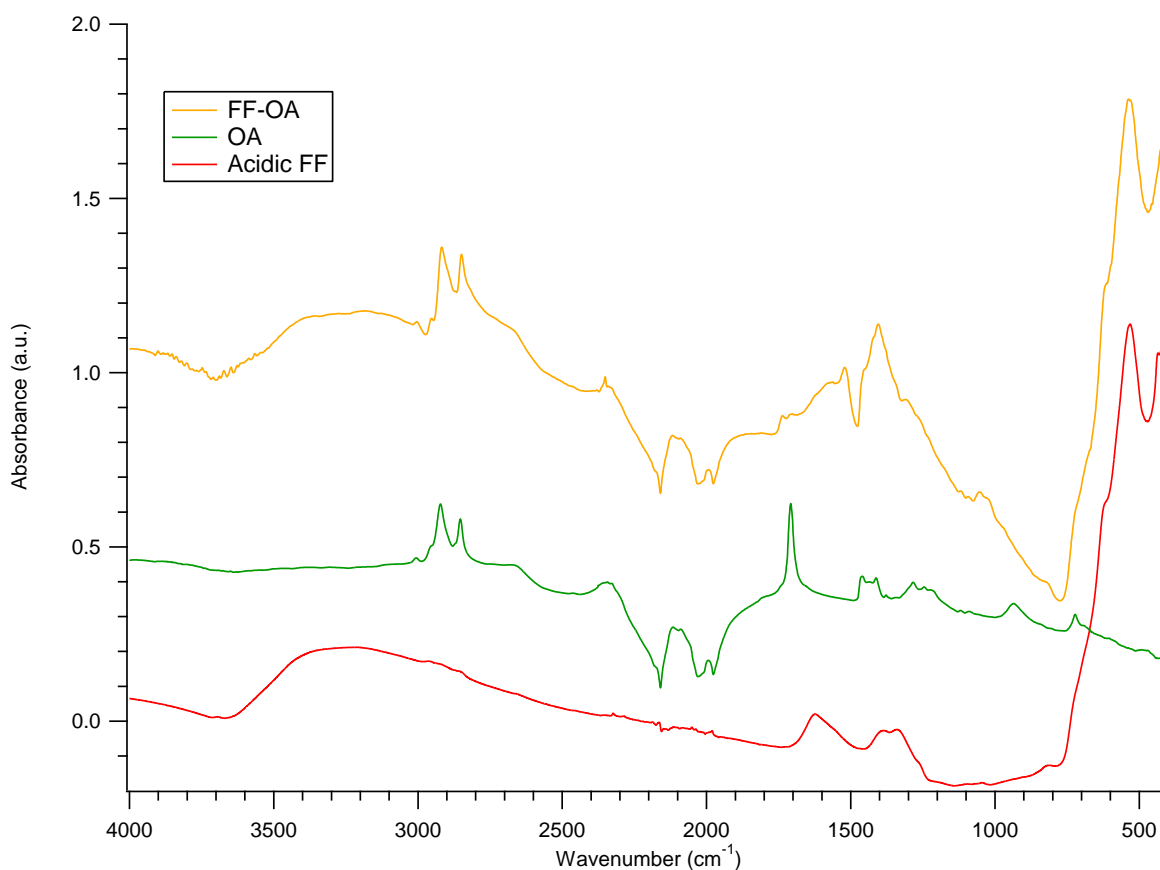


Figure 4.3. FTIR analysis of the acidic FF (red), the oleic acid (green) and the FF-OA (orange).

Table 4.1. IR band positions and assignments for acidic FF, OA and FF-OA. The area between 2000 and 2500 cm⁻¹ represents the absorbance of the diamond used.

Assignment	Wavenumber (cm ⁻¹)		
	Acidic FF	OA	FF-OA
v (Fe-O)	531	-	537
v (CH ₂)	-	722	-
v (OH) out-of-plane	-	936	-
v (C-O)	-	1284	1050
v (COO ⁻) symmetric	-	1412	1405
v (COO ⁻) asymmetric	-	1459	1522
v (C=O)	-	1708	1710
v (CH ₂) symmetric	-	2853	2849
v (CH ₂) asymmetric	-	2922	2918

3.1.1.2. BNE

The FT-IR spectra of the acidic FF, the BNE and the BNE-coated maghemite samples investigated also in the 500-4000 cm⁻¹ range are presented in Figure 4.3. The characteristic absorption bands of the Fe-O bond of γ -Fe₂O₃ can be observed at 532 cm⁻¹ and 619 cm⁻¹ on the curve of FF-BNE that we find at 531 cm⁻¹ and 624 cm⁻¹ for the acidic FF (Table 4.2). The peaks situated at 879 cm⁻¹ and 2870 cm⁻¹ are attributed to CH bonds. The large band at 949-1099 cm⁻¹ could coincide with the C-C stretching bond of the carbon skeleton of the BNE which is found at 1000-1086 cm⁻¹ in the FF-BNE. From 1248 cm⁻¹ to 1511 cm⁻¹, stretching bands of P=O function are appearing. The large band presents at 3088-3455 cm⁻¹ for BNE and FF-BNE correspond to the elongation of the aromatic rings and also to the CH₂ and OH stretches.

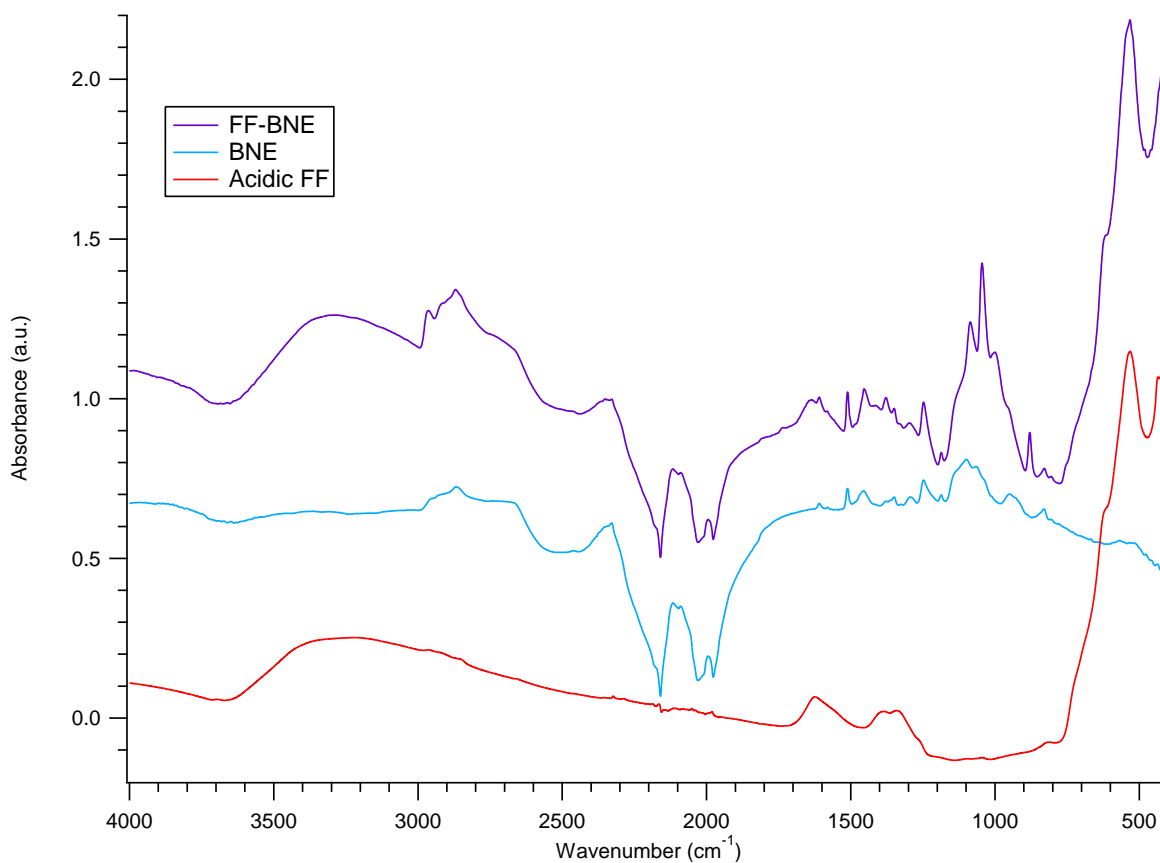


Figure 4.4. FTIR analysis of the acidic FF (red), the BNE (blue) and the FF-BNE (purple).

Table 4.2. IR band positions and assignments for acidic FF, BNE and FF-BNE. The area between 2000 and 2500 cm^{-1} represents the absorbance of the diamond used.

Assignment	Wavenumber (cm^{-1})		
	Acidic FF	BNE	FF-BNE
ν (Fe-O)	531	-	532
ν (Fe-O)	624	-	619
ν (CH)	-	879	879
ν (C-C)	-	949-1099	1000-1086
ν (P=O)	-	1248-1511	1248-1511
ν (CH)	-	2868	2870
ν (=C-H, C=C, CH ₂ , OH)	-	3088-3455	3088-3455

3.1.2. FF-Labrafils interactions : SAXS analysis

SAXS analysis were done to investigate i) the dispersibility of the FF grains into the Labrafil based lipid phase to select the best couples and ii) the influence of FF grains on the Labrafils behavior, notably the phase separation which induces the formation of the *Janus* nanoparticles. Dispersions containing $\sim 0.15\text{M}$ and 0.015M of iron were used during these experiments. The highest concentrations being too important, the diffusion signal masked the potential phase separation signal. Thus, only the results obtained with the lowest concentration will be presented in the following lines. Figure 4.5 represents the SAXS analysis of different Labrafil®-FF mixtures at 20°C . The first part of the graph allows Guinier analysis whereas the study of the whole curve gives the evaluation of the particle distance distribution function $p(r)$. Focusing on the stabilizers, we can distinguish two different profiles : one for the FF-OA containing samples and the other one for the dispersion with FF-BNE.

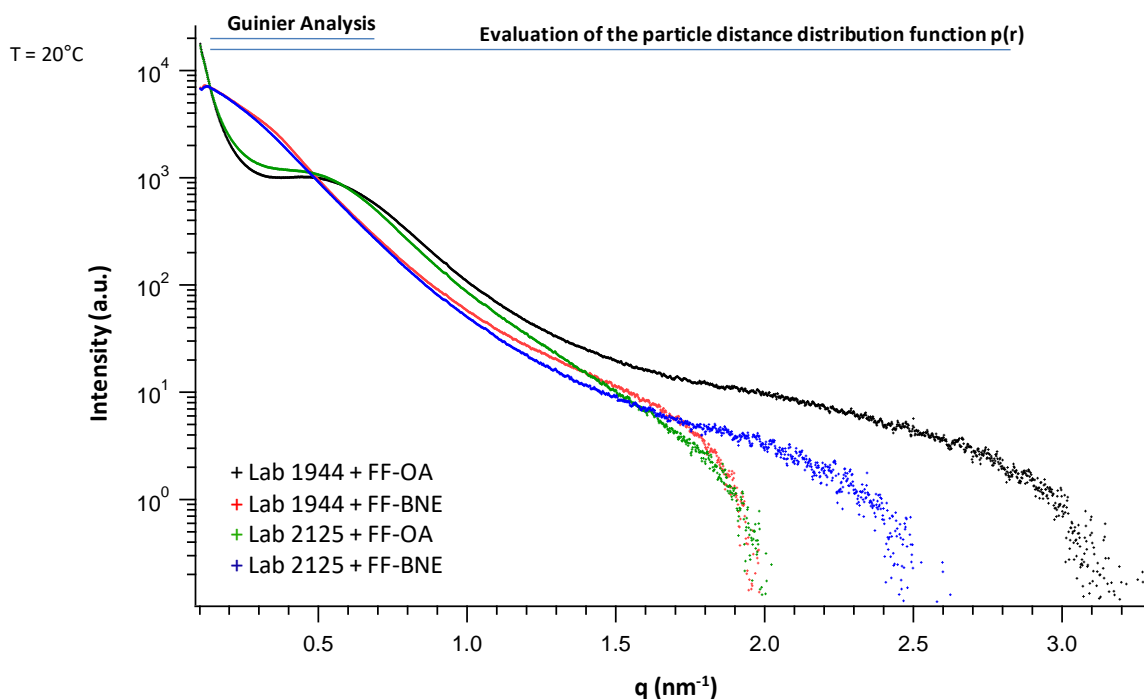


Figure 4.5. SAXS analysis of Labrafil® M1944 CS/FF-AO (black), Labrafil® M1944 CS/FF-BNE (red), Labrafil® M2125 CS/FF-AO (green) and Labrafil® M2125 CS/FF-BNE (blue) mixing.

On the Guinier analysis (Figure 4.6), mixtures containing FF-OA present a positive curvature which is characteristic of an aggregation in the system. Regarding the mixtures made with FF-

BNE, the obtained signal is linear. This can allow us to calculate the R_g of the particles present in the medium.

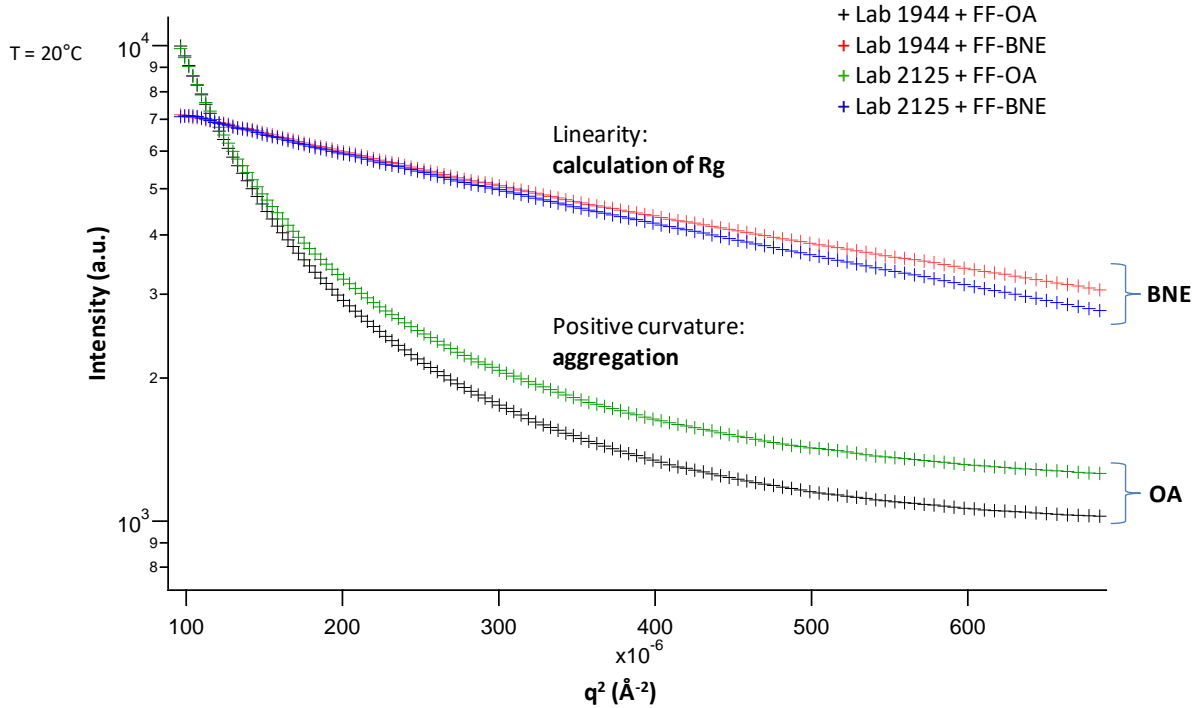


Figure 4.6. Guinier analysis of Labrafil® M1944 CS/FF-OA (black), Labrafil® M1944 CS/FF-BNE (red), Labrafil® M2125 CS/FF-OA (green) and Labrafil® M2125 CS/FF-BNE (blue) mixing.

The evaluation of the particle distance distribution function $p(r)$ (Figure 4.7) gives the R_g of the hydrophobic maghemite (FF-BNE) used in the mixtures. FF-BNE can be compared to monodisperse spheres and obtained R_g have good analogy with Guinier analysis. In Labrafil® M1944 CS, the R_g of FF-BNE is 5.2 nm which is very similar to that found in Labrafil® M2125 CS : 5.4 nm (Table 4.3). In case of FF-OA, an analysis of the distribution function has been done too. However, the monodispersed sphere model appeared as poorly adapted here and R_g from 16 to 20 nm where estimated. This confirms the aggregation of FF-OA grains after mixing with the Labrafils as suggested by the Guinier analysis.

Table 4.3. Comparison on the radius of gyration between Guinier analysis and $P(r)$ function analysis.

	Radius of gyration (nm)	
	Guinier Analysis	$P(r)$ function Analysis
FF-BNE / Labrafil M1944CS	5.7	5.2
FF-BNE / Labrafil M2125CS	5.8	5.4

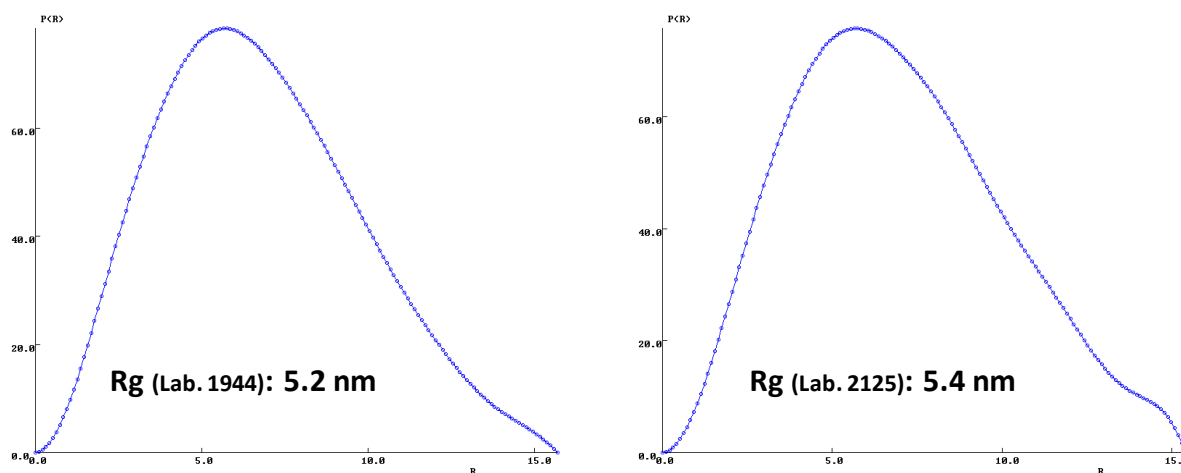


Figure 4.7. Evaluation of the particle distance distribution function $p(r)$ (extraction from the GNOM software interface).

SAXS experiments were carried out on several hydrated mixtures (10 wt% of water) containing pure Labrafil® M2125 CS, Labrafil® M2125 CS and FF-BNE or Labrafil® M2125 CS and FF-OA (Figure 4.8). On X-ray diffraction pattern, two diffraction peaks are detected into pure hydrated Labrafil characterizing the two first order of a lamellar phase with a period of 92 Å at 20°C. This lamellar organization was previously described in other Labrafil® M2125 batches (previous chapters) and was attributed to the presence of poly(oxyethylene)-6 unsaturated-C18 ester in Labrafils. If the Labrafil® is mixed with both FF-BNE and FF-OA, the diffraction peak is still present on the diffractogram but its position is shifted to larger distances. For both FF, we can estimate it at a period of 98 Å (Table 4.4).

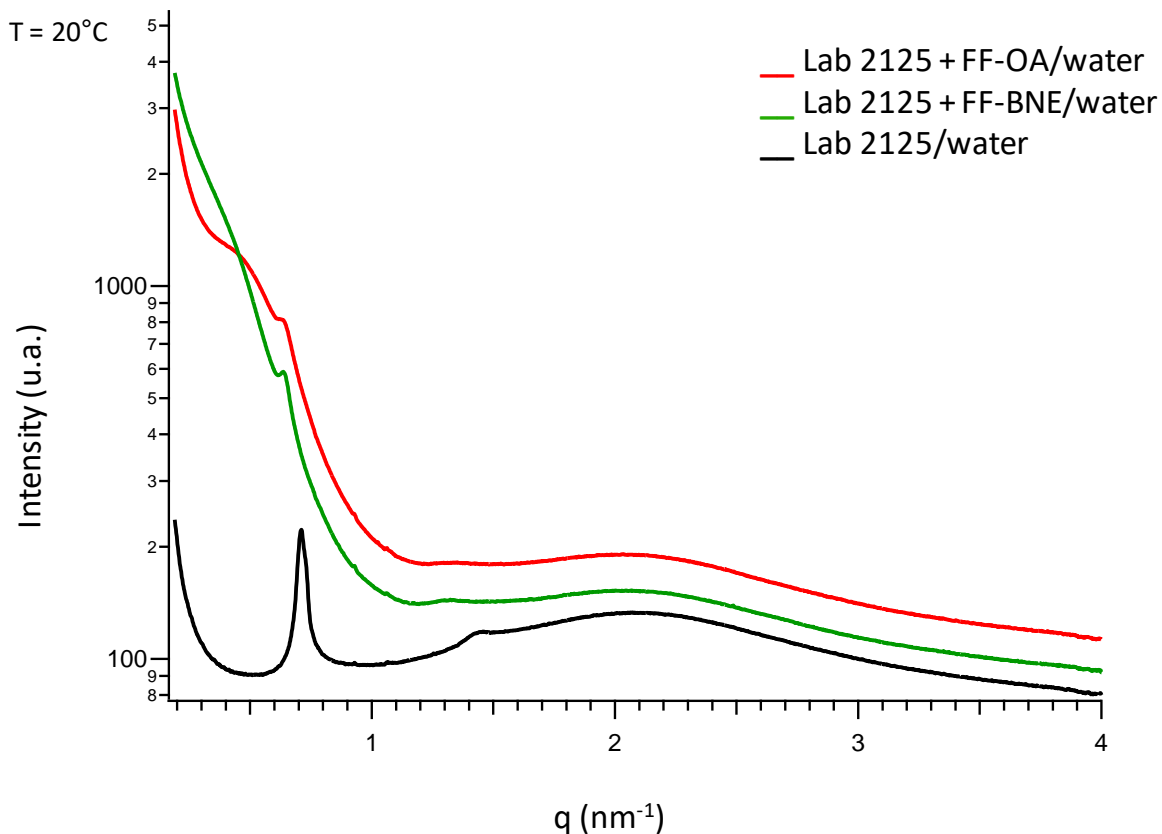


Figure 4.8. SAXS experiments on Labrafil® M2125 CS mixed with water (black), FF-BNE and water (green) or FF-OA and water (red).

Unfortunately, the quantification of the disappearance temperature of the peak is more difficult than with pure Labrafil or mixture with hydrophilic FF (chapter 2) because of the strong diffusion signal of the FF.

Table 4.4. Evolution of the thickness of the hydrated Labrafil® M2125 CS lamellar phase depending on the presence and type of hydrophobic FF.

Labrafil®/aqueous phase	d (Å)
2125 + FF-OA/water	98
2125 + FF-BNE/water	98
2125/water	92

Similar tendencies were observed with Labrafil® M1944 CS containing samples (Figure 4.9) in which the lamellar phase period increases from 85 to ~ 90 Å, at 20°C, in presence of hydrophobic FF (Table 4.5).

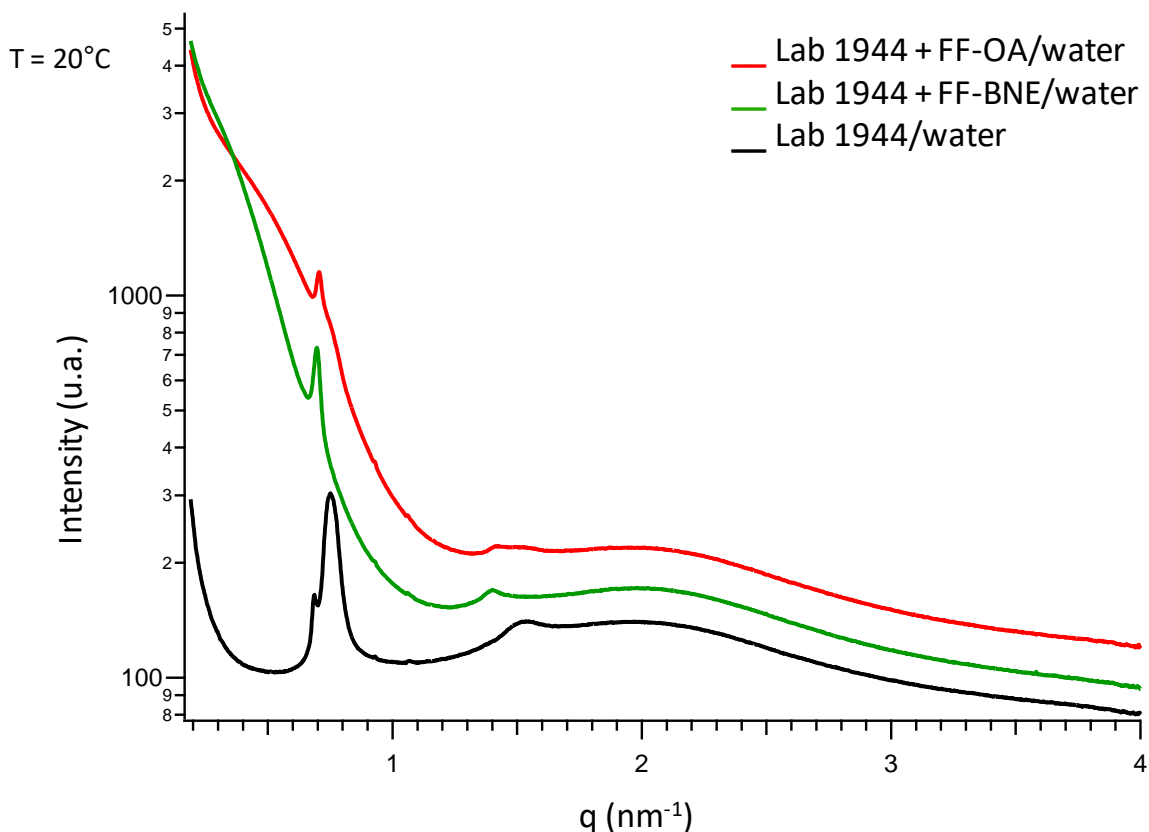


Figure 4.9. SAXS experiments on Labrafil® M1944 CS mixed with water (black), FF-BNE and water (green) or FF-OA and water (red).

Table 4.5. Evolution of the thickness of the hydrated Labrafil® M1944 CS lamellar phase depending on the presence and type of hydrophobic FF.

Labrafil®/aqueous phase	d (Å)
1944 + FF-OA/water	90
1944 + FF-BNE/water	89
1944/water	85

From all these experiments, it is possible to estimate that hydrophobic FF doesn't prevent the formation of a lamellar phase into hydrated Labrafils. Furthermore, the thickness of the lamellar

phase depends on the type of Labrafil, on the presence of FF but not on the type of stabilizer (OA or BNE). This suggests i) that the grains are not directly intercalated in the lamellar phase as its thickness is equal for dispersed (FF-BNE) and aggregated (FF-AO) FF and then ii) that the hydrophobic FF interact with the glyceridic fraction of the Labrafils. The slight difference in terms of lamellar thickness between FF-loaded and unloaded Labrafils would probably result from the diffusion background and from the Labrafil / water ratio which will be slightly different in the samples due to the presence of FF in some of them.

3.2. Incorporation trials in *Janus* nanoparticles

The objective of this part of the work is to encapsulate SPION in the lipid compartment of *Janus* nanoparticles. Because of the aggregation of FF-OA in the Labrafils, FF-BNE has been used for this purpose. To generate *Janus* nanoparticles, a HPH process is used by adding a lipid phase containing the hydrophobic FF in PEG vegetable oils (Labrafil® M2125 CS for FF-2125-JNP or Labrafil® M1944 CS for FF-1944-JNP) into an aqueous phase made of phospholipids (Phospholipon® 90G), non-ionic surfactant (Gélucire® 50/13) and water. After cooling at room temperature, a stable dispersion is obtained (Figure 4.10). The size of the nanoparticles remains of the order of 200 nm during the first 4 months and then increases considerably and a formation of aggregates is observed whereas the unloaded *Janus* nanoparticles remain stable at least 20 months at room temperature. No investigations have been done yet to understand the destabilization mechanism in that case. However, we can be hypothesize that the presence of free FF-BNE outside of the *Janus* nanoparticles (the particles were not purified before storage) may interfere with their stability. Indeed, several studies in the laboratory (unpublished data) have shown that the stability of these *Janus* nanoparticles is sensitive to the composition of the water phase.

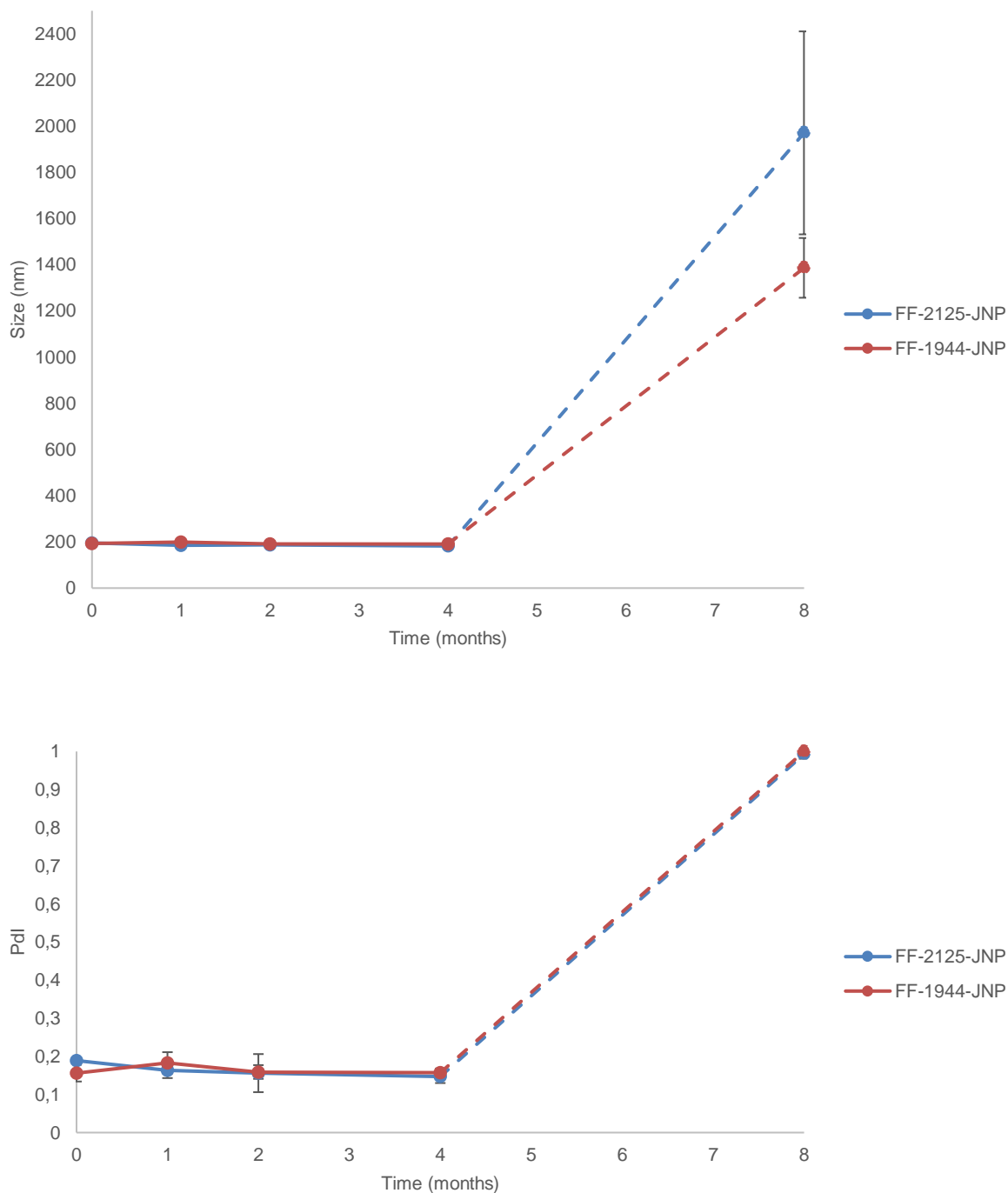


Figure 4.10. Evolution of the size of the nanodispersions with the time. Purified FF-2125-JNP in blue, purified FF-1944-JNP in red.

Cryo-TEM pictures (Figure 4.11) show magnetic grains inside the lipid part of bi-compartmented *Janus* nanoparticles.

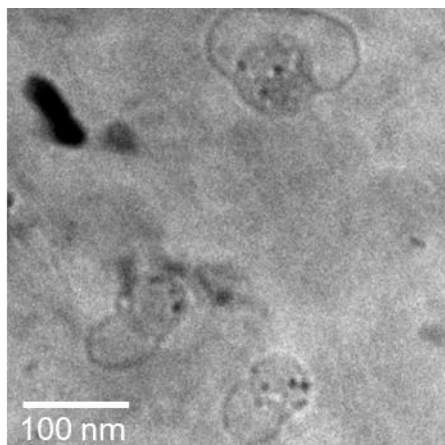


Figure 4.11. Cryo-TEM view of *Janus* nanoparticles.

The *Janus* nanoparticles are then purified by centrifugation in order to eliminate the non-encapsulated hydrophobic maghemite which would tend to precipitate in the aqueous phase. Iron concentrations are evaluated before and after purification step for each samples in order to determine the final iron concentration, the SPION loading and the entrapment efficiency with equations 1 and 2 (Table 4.6). For both samples, iron concentrations were around 70 mM, SPION loading close to 3% and entrapment efficiency in the [60-70%] range.

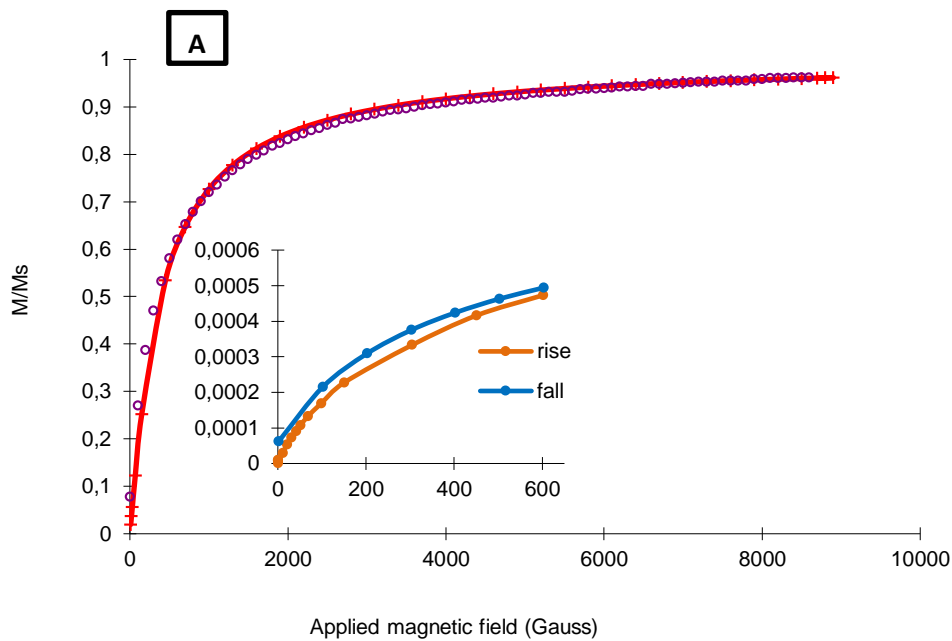
Table 4.6. Iron concentration, SPION loading and encapsulation efficiency in purified formulations.

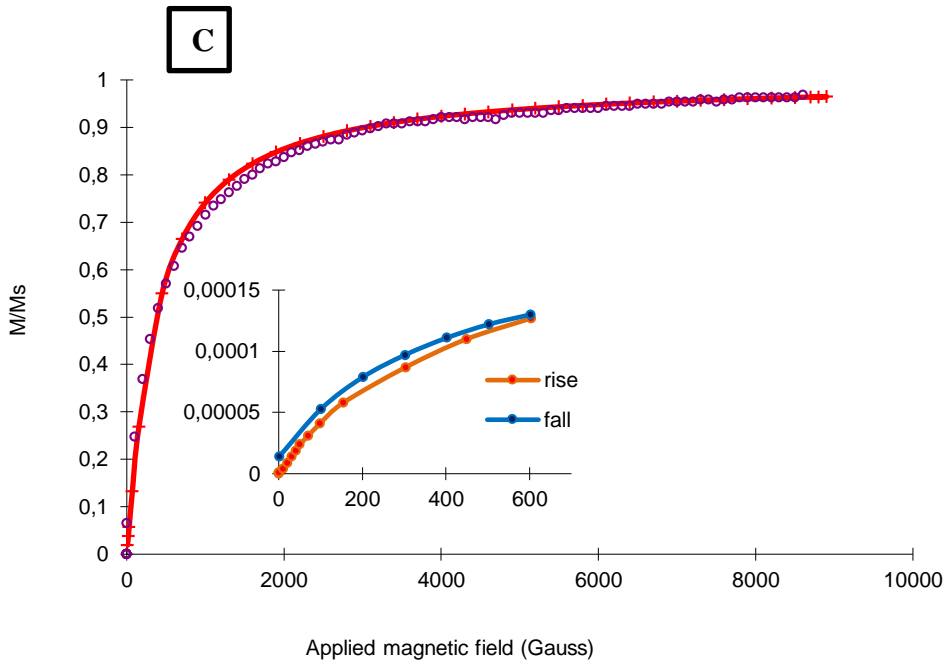
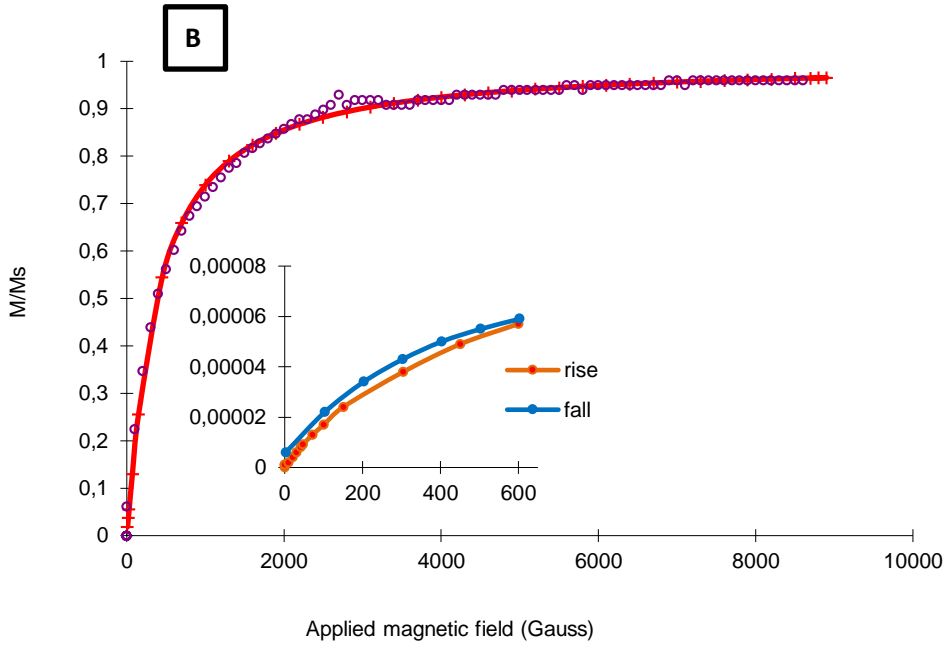
Sample	Iron concentration (mM)	SPION loading (%)	Entrapment Efficiency (%)
FF-2125-JNP	70	2.8	69.3
FF-1944-JNP	67	2.7	59.6

3.3. Magnetization

The magnetic properties of the purified *Janus* nanoparticles and FF-BNE dispersed in Labrafil® are determined by magnetometry. The aqueous dispersions are studied with a vibrating sample magnetometer (VSM). Figure 4.12 shows the evolution of the macroscopic magnetization M normalized by its saturation value M_s . The fit was calculated using the Langevin function of paramagnetism convoluted with a log-normal distribution function of the particle sizes. Both fitted curves are nearly superimposable and are characteristic of a superparamagnetic

behaviour, with a strong magnetic susceptibility, and a thin hysteresis at low magnetic fields [24]. This experiment was conducted with the FF-BNE dispersed in the two different Labrafil® (Figure 4.12 C and D). The parameters of this distribution are $D_{0VSM} = 8.2$ nm (maximum of the size distribution) and $\sigma_{VSM} = 0.4$ (standard deviation) for FF-BNE-2125 and, $D_{0VSM} = 8.7$ nm and $\sigma_{VSM} = 0.35$ for FF-BNE-1944. The same was done with purified *Janus* nanoparticles and the parameters of this distribution are $D_{0VSM} = 8.6$ nm and $\sigma_{VSM} = 0.4$ for FF-2125-JNP and, $D_{0VSM} = 8.3$ nm and $\sigma_{VSM} = 0.4$ for FF-1944-JNP. The results show a similar behavior between the free maghemite and the maghemite entrapped in the *Janus* nanoparticles indicating that the SPION's integrity is preserved when encapsulated in the *Janus* nanoparticles.





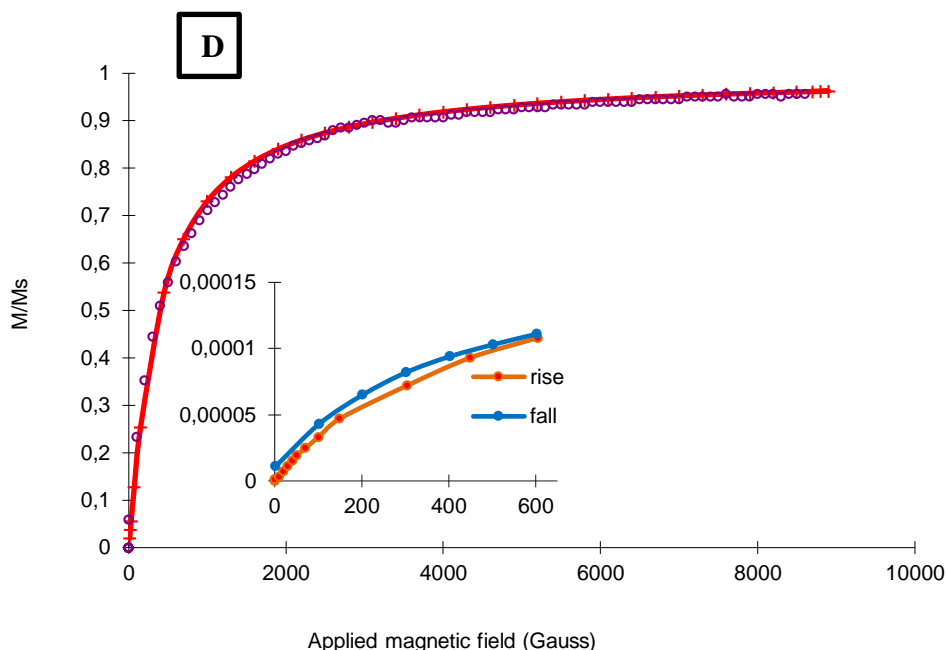


Figure 4.12. Magnetization of the studied nanodispersions versus magnetic field. A) FF-BNE-2125, B) FF-BNE-1944, C) purified FF-2125-JNP and D) purified FF-1944-JNP.

3.4. Relaxometry

As expected, the relaxation rates $1/T_1$ and $1/T_2$ for purified FF-2125-JNP and FF-1944-JNP increase linearly with iron concentrations over the range of concentrations considered in this study. This allows to calculate the relaxivities by determining the slopes (see bibliographic chapter).

r_1 values for FF-2125-JNP and FF-1944-JNP are found to be $2.9 \pm 0.5 \text{ mM}^{-1}\text{s}^{-1}$ and $4.3 \pm 0.6 \text{ mM}^{-1}\text{s}^{-1}$ respectively whereas r_2 values are quite different at $214 \pm 55 \text{ mM}^{-1}\text{s}^{-1}$ and $60 \pm 2 \text{ mM}^{-1}\text{s}^{-1}$ respectively (Table 4.7). The r_2/r_1 ratio which defines the effectiveness of a T_1 or T_2 contrast agent is calculated for both FF-2125-JNP and FF-1944-JNP and found to be 74 and 14 respectively which are much higher than the r_2/r_1 ratio of commercial contrast agents Resovist® and Endorem® at 6.2 and 4 respectively [25] allowing us to qualify our system as a good candidate for MRI contrast agent.

Table 4.7. Relaxivities r_1 and r_2 and r_2/r_1 ratio of purified FF-2125-JNP and FF-1944-JNP.

	r_1 (mM ⁻¹ s ⁻¹)	r_2 (mM ⁻¹ s ⁻¹)	r_2/r_1
FF-2125-JNP	2.9 ± 0.5	214 ± 55	74
FF-1944-JNP	4.3 ± 0.6	60 ± 2	14

Jarzyna *et al.* [6] developed a soybean oil-based NE containing commercial OA-SPION with mean hydrodynamic diameters of 30, 60 and 95 nm respectively, depending on the relative proportions of the different lipid components. ICP-MS analysis revealed nearly a 100% encapsulation efficacy of magnetite, then similar SPION number to droplet volume ratios, leading to r_1 values of 2.5 ± 0.4 mM⁻¹s⁻¹, 2.7 ± 0.3 mM⁻¹s⁻¹, 2.9 ± 0.3 mM⁻¹s⁻¹ at 1.41 T for the 30, 60, and 95 nm emulsions, respectively and high r_2 values of 76 ± 1 mM⁻¹s⁻¹, 136 ± 9 mM⁻¹s⁻¹ or 184 ± 7 mM⁻¹s⁻¹ at the same field. The corresponding r_2/r_1 ratios vary from 30 to 64. r_2/r_1 ratios from 43 to 81, with r_2 values from 230 to 320 mM⁻¹s⁻¹, were also measured at 25 MHz in cetyl palmitate SLN (~250 nm of hydrodynamic diameter) by Calucci and co-workers [26]. Interestingly, our relaxivity results are in the same ranges and confirm that the lipid compartment of the *Janus* particles has similarities with lipid-based nanodispersions.

Three main regimens are used to describe transverse relaxivity r_2 of SPION clusters : the motional average regime (MAR) in which the protons of freely diffusing water molecules explore all the possible values of magnetic fields during their diffusion in the neighboring of the particles, the static dephasing regime (SDR) in which water protons explore only a small volume around the particle compared to the hydrodynamic volume and the echo-limiting or partial refocusing regime (ELR or PRM) when relaxivity exhibits a strong dependence on the measuring sequence, notably on the chosen echo time [27]. It is generally admitted that inclusion in the motional average regime requires that $\tau_D \Delta\omega < 1$ with τ_D , the translational (or correlation) diffusion time and $\Delta\omega$, the equatorial Larmor frequency shift. These two parameters are related to the properties of the particles and the dynamics of protons with the following equations [28] :

$$\Delta\omega = \frac{\mu_0 \gamma M_v}{3} \quad (3)$$

$$\tau_D = \frac{R^2}{D} \quad (4)$$

where μ_0 is the vacuum magnetic permeability ($4\pi \times 10^{-7}$), γ is the proton gyromagnetic factor ($2.67513 \times 10^8 \text{ rads}^{-1}\text{T}^{-1}$), M_v , the magnetization at saturation extracted from the magnetization curves, R , here the radius of the lipid compartment and D , the water diffusion constant at experimental temperature ($2.3 \times 10^{-9} \text{ m}^2\text{s}^{-1}$).

When $1 < \tau_D \Delta\omega < \sim 20$, static dephased regime is the most adapted while partial refocusing model should be considered at higher values [29]. With overall magnetizations equal to 253 A.m^{-1} and 296 A.m^{-1} for FF-2125-JNP and FF-1944-JNP respectively and an oil droplet compartment radius that we estimated at $\sim 80 \text{ nm}$ by considering that both compartments have the same volume in the *Janus* nanoparticles, it is possible to calculate $\tau_D \Delta\omega$ values lower than 1. Transversal relaxivity of the *Janus* particles should then be governed by the motional average regime.

More deeply in the motional average regime, three different cases were distinguished [30] : the isotropically distributed spherical SPION model in which the SPION are isotropically dispersed and non-clustered in the suspension, the loose aggregates model in which SPION are homogeneously distributed in the oil droplet and the dense aggregates model in which higher SPION cluster densities are achieved by their close packing. In our system, the loose aggregates model seemed to be the most realistic as i) SPION are not freely dispersed in the whole suspension volume but only into the lipid oil compartment and ii) from the cryo-TEM pictures, confirmed by the low SPION loadings, the lipid compartment is not fully filled with SPION.

In this loose aggregates model, the transversal relaxivity can be calculated by a full model [30] or a validated simplified equation [29] described below :

$$r_2 = \frac{11.6 \times 10^{-12} d^2 M_v^2}{\varphi_{intra}} \quad (5)$$

where, d is the particle diameter (nm), meaning the oil droplet in our case, M_v , the saturation magnetization, and φ_{intra} , the intra-aggregate volume fraction of magnetic materials. This later parameter is ~ 0.0055 in our particles by considering the SPION loading (Table 4.5). It is interesting to note here that such intra-aggregate volume fraction of magnetic material is in the same range than the corresponding values calculated by Vuong et al. in their extensive comparison of SPION nanocarriers (liposomes, polymersomes, polymeric micelles, etc.). Unfortunately, compared with theoretical predictions, our measured transverse relaxivities are

significantly higher. Indeed, calculated transversal relaxivities were $\sim 5 \text{ mM}^{-1}\text{s}^{-1}$ while the measured ones are in the range $60\text{-}200 \text{ mM}^{-1}\text{s}^{-1}$.

Hak et al [30] deeply compare experimental transverse relaxivities of SPION dispersed into oil droplets as a function of clustering and magnetic field strength with the theoretical models previously presented. To summarize their results, only the loose aggregate model described correctly the dependence on oil droplet diameter, the dense aggregate model described best the dependence on number of SPION in the droplets while the static dephasing model described best the dependence on magnetic field strength. Considering absolute values, and compared to the experimental results, the values were slightly overestimated by static dephasing model, slightly underestimated by the dense aggregates model and more strongly underestimated by the other theories. In the case of the loose aggregate model, the values they measured were 10 to 20 times higher than the values they calculated, the same order of magnitude as our results. The discrepancy between transversal relaxivity absolute values calculated with this model and the experimental values has been also mentioned several times in the literature [31,32]. Based on literature review, mainly two reasons could explain the low predictability of the model. First, the presence of the PEG layer at the surface of the oil droplets in which the protons are bound and unlikely to exchange compared to bulk water [30,31]. This explanation is totally coherent with the morphology of our particles as they should be surrounded by a PEG₁₅₀₀ layer. Second, polydispersity of the dispersion and SPION distribution heterogeneities into the oil droplet have been also described as parameters that can significantly distend theories and experimental results [26,33].

3.5. Accumulation

In Figure 4.13 are compared dispersed *Janus* nanoparticles and the same suspension after several weeks of exposition to a magnet. A local accumulation is visible while the dispersing phase became clear. This confirms the incorporation of FF in the particles and their susceptibility to magnetic field.

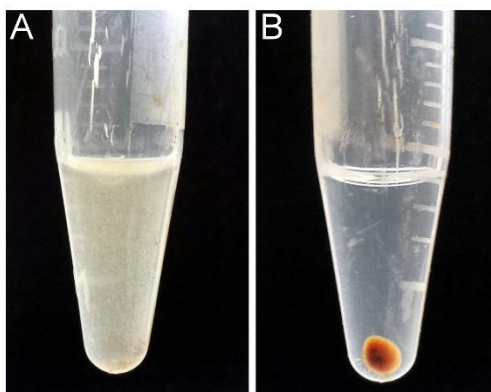


Figure 4.13. Dispersed Janus nanoparticles (A) and accumulated ones (B) after exposure to a magnet.

4. Conclusion

In this study, two surfactants were tested to stabilize superparamagnetic iron oxide nanoparticles in hydrophobic medium. After several characterizations, the BNE was selected as the best lipid stabilizer for further lipid encapsulation in *Janus* nanoparticles. FF-BNE were then entrapped in the lipid part of *Janus* nanoparticles and the obtained nanodispersions were purified before magnetic characterizations. Magnetization and relaxometric measurements were carried out in order to evaluate the superparamagnetic nature of the prepared *Janus* nanoparticles. Attempts will be made in further investigations to assess the potential hyperthermia activity of the magnetic *Janus* nanoparticles and a hydrophilic API may be incorporated in the aqueous compartment in order to confer a theranostic application to these new nanoobjects.

References

- [1] Gupta A, Eral HB, Hatton TA, et al. Nanoemulsions: formation, properties and applications. *Soft Matter*. 2016;12:2826–2841.
- [2] Singh Y, Meher JG, Raval K, et al. Nanoemulsion: Concepts, development and applications in drug delivery. *J. Controlled Release*. 2017;252:28–49.
- [3] Salcido A. Equilibrium Properties of the Cellular Automata Models for Traffic Flow in a Single Lane. *Cell. Autom.-Simplicity Complex*. InTech; 2011. p. 159–172.
- [4] Bates TR, Carrigan PJ. Apparent absorption kinetics of micronized griseofulvin after its oral administration on single- and multiple-dose regimens to rats as a corn oil-in-water emulsion and aqueous suspension. *J. Pharm. Sci.* 1975;64:1475–1481.
- [5] Sainsbury F, Zeng B, Middelberg AP. Towards designer nanoemulsions for precision delivery of therapeutics. *Curr. Opin. Chem. Eng.* 2014;4:11–17.
- [6] Jarzyna PA, Skajaa T, Gianella A, et al. Iron oxide core oil-in-water emulsions as a multifunctional nanoparticle platform for tumor targeting and imaging. *Biomaterials*. 2009;30:6947–6954.
- [7] Sarker D. Engineering of Nanoemulsions for Drug Delivery. *Curr. Drug Deliv.* 2005;2:297–310.
- [8] Ragelle H, Crauste-Manciet S, Seguin J, et al. Nanoemulsion formulation of fisetin improves bioavailability and antitumour activity in mice. *Int. J. Pharm.* 2012;427:452–459.
- [9] Morsi N, Ibrahim M, Refai H, et al. Nanoemulsion-based electrolyte triggered in situ gel for ocular delivery of acetazolamide. *Eur. J. Pharm. Sci.* 2017;104:302–314.
- [10] Shakeel F, Alanazi FK, Raish M, et al. Pharmacokinetic and in vitro cytotoxic evaluation of cholesterol-rich nanoemulsion of cholesteryl-succinyl-5-fluorouracil. *J. Mol. Liq.* 2015;211:164–168.

- [11] Ge W, Hu P-Z, Huang Y, et al. The antitumor immune responses induced by nanoemulsion-encapsulated MAGE1-HSP70/SEA complex protein vaccine following different administration routes. *Oncol. Rep.* 2009;22:915–920.
- [12] Chuan YP, Zeng BY, O’Sullivan B, et al. Co-delivery of antigen and a lipophilic anti-inflammatory drug to cells via a tailorable nanocarrier emulsion. *J. Colloid Interface Sci.* 2012;368:616–624.
- [13] Bakandritsos A, Zboril R, Bouropoulos N, et al. The preparation of magnetically guided lipid based nanoemulsions using self-emulsifying technology. *Nanotechnology.* 2010;21:055104.
- [14] Nikolaev BP, Eliseev OV, Marchenko YY, et al. Preparation of Magnetite Nanoemulsion Stabilized by Tween 81 for MRI Contrast Enhancement. *AIP Conf. Proc.* 2010;1311:458–465.
- [15] Tong S, Hou S, Zheng Z, et al. Coating Optimization of Superparamagnetic Iron Oxide Nanoparticles for High T2 Relaxivity. *Nano Lett.* 2010;10:4607–4613.
- [16] Rodríguez-Burneo N, Busquets M, Estelrich J. Magnetic Nanoemulsions: Comparison between Nanoemulsions Formed by Ultrasonication and by Spontaneous Emulsification. *Nanomaterials.* 2017;7:190.
- [17] Lahiri BB, Ranoo S, Zaibudeen AW, et al. Magnetic hyperthermia in magnetic nanoemulsions: Effects of polydispersity, particle concentration and medium viscosity. *J. Magn. Magn. Mater.* 2017;441:310–327.
- [18] Gianella A, Jarzyna PA, Mani V, et al. Multifunctional Nanoemulsion Platform for Imaging Guided Therapy Evaluated in Experimental Cancer. *ACS Nano.* 2011;5:4422–4433.
- [19] Deddens LH, Jarzyna PA, Griffioen AW, et al. RGD-Functionalized Superparamagnetic Nanoemulsions for Target-Specific Imaging of Tumor Angiogenesis. *Proc Intl Soc Mag Reson Med.* 2010;18:3749.

- [20] Jarzyna PA, Deddens LH, Kann BH, et al. Tumor Angiogenesis Phenotyping by Nanoparticle-facilitated Magnetic Resonance and Near-infrared Fluorescence Molecular Imaging. *Neoplasia*. 2012;14:964–973.
- [21] Massart R. Preparation of aqueous magnetic liquids in alkaline and acidic media. *IEEE Trans. Magn.* 1981;17:1247–1248.
- [22] Petoukhov MV, Konarev PV, Kikhney AG, et al. ATSAS 2.1—towards automated and web-supported small-angle scattering data analysis. *Appl. Crystallogr.* 2007;40:s223–s228.
- [23] Zhang L, He R, Gu H-C. Oleic acid coating on the monodisperse magnetite nanoparticles. *Appl. Surf. Sci.* 2006;253:2611–2617.
- [24] Bacri J-C, Perzynski R, Salin D, et al. Magnetic colloidal properties of ionic ferrofluids. *J. Magn. Magn. Mater.* 1986;62:36–46.
- [25] Qin J, Laurent S, Jo YS, et al. A High-Performance Magnetic Resonance Imaging T2 Contrast Agent. *Adv. Mater.* 2007;19:1874–1878.
- [26] Calucci L, Grillone A, Redolfi Riva E, et al. NMR Relaxometric Properties of SPION-Loaded Solid Lipid Nanoparticles. *J. Phys. Chem. C*. 2017;121:823–829.
- [27] Gillis P, Moyny F, Brooks RA. OnT2-shortening by strongly magnetized spheres: A partial refocusing model. *Magn. Reson. Med.* 2002;47:257–263.
- [28] Gossuin Y, Orlando T, Basini M, et al. NMR relaxation induced by iron oxide particles: testing theoretical models. *Nanotechnology*. 2016;27:155706.
- [29] Vuong QL, Berret J-F, Fresnais J, et al. A Universal Scaling Law to Predict the Efficiency of Magnetic Nanoparticles as MRI T2-Contrast Agents. *Adv. Healthc. Mater.* 2012;1:502–512.
- [30] Hak S, Goa PE, Stenmark S, et al. Transverse relaxivity of iron oxide nanocrystals clustered in nanoemulsions: Experiment and theory. *Magn. Reson. Med.* 2015;74:858–867.

- [31] Carvalho A, Goncalves C, Corvo M, et al. Development of New Contrast Agents for Imaging Function and Metabolism by Magnetic Resonance Imaging. *Magn. Reson. Insights*. 2017;10:1–4.

- [32] Xie X, Zhang C. Controllable Assembly of Hydrophobic Superparamagnetic Iron Oxide Nanoparticle with mPEG-PLA Copolymer and Its Effect on MR Transverse Relaxation Rate. *J. Nanomater.* 2011;2011:1–7.

- [33] Pöselt E, Kloust H, Tromsdorf U, et al. Relaxivity Optimization of a PEGylated Iron-Oxide-Based Negative Magnetic Resonance Contrast Agent for T2-Weighted Spin-Echo Imaging. *ACS Nano*. 2012;6:1619–1624.

GENERAL DISCUSSIONS

Discussion

Beside the points already discussed in the experimental chapters, several aspects must be commented with more attention or completed with some additional studies which were not incorporated in the previous sections.

On the formation mechanism

Many techniques have been developed to generate *Janus* (nano)particles. In general, they are divided into three main methods : masking, bottom-up assemblies and controlled phase separation [1]. Masking was developed simply by the modification of one side of preformed particles. Briefly, homogeneous nanoparticles are trapped at a surface so that one hemisphere is exposed and modified by a chemical that changes the particle properties. Finally, the masking agent is removed, and *Janus* objects are released. Depending on the 2D- or 3D-growth of the second component, patchy or more dumbbell-like particles could be prepared. Bottom-up assemblies concern self-assembly of specially designed di- or triblock copolymers or the attachment of preformed precursor particles. The constituting components self-assemble following their preferential ways of either minimum local or global free energy or favored kinetics, achieving structures of robust mechanical stability. In some occasion, molecular interaction within “ligand-receptor” shells can also provide a way to prepare anisotropic objects. Controlled phase separations could occur from i) volume segregation where two incompatible substances were mixed to form a perfect mixture and then separated into domains, within a single particle, thanks to a separation trigger, ii) surface nucleation of a second compartment on a preformed seed or iii) co-jetting of laminar flow of different materials.

The SAXS experiments and direct observations we made with optical microscopes during that work strongly suggest a controlled phase separation mechanism with volume segregation. The evaporation of a solubilizing solvent is the most useful trigger for that separation [2]. In our case, we don't solubilize one of the formulation component, the solubility of which would depend on the evaporation of a solvent. However, it seems, from our results, that the physico-chemical properties and the solubility of ethoxylated fraction of the Labrafils, after hydration, strongly depend on temperature. Temperature appears as the probable trigger of the phase separation in our system.

To underline the role of temperature, interfacial tension experiments have been done on Labrafils. Indeed, such behavior with temperature is related to phase inversion temperature that has been extensively studied for emulsions stabilized by nonionic ethoxylated surfactants. For such emulsions, which are heated or cooled beyond the phase inversion temperature, typical changes in morphology are observed. The emulsion inverts by going from an oil-in-water to an water-in-oil emulsion or *vice versa*. This means that the spontaneous curvature of the interfacial film changes sign (positive – negative) and passes a flat form where the curvature is zero [2]. This point is the balanced point where the interfacial tension is at its minimum. By following the interfacial tension of Labrafils droplets (rising drop) into water, we determined phase inversion temperatures around 40°C-43°C for these products. This result is consistent with the phase inversion temperatures that we estimated from SAXS experiments and optical microscope observations, which were 36°C and 40°C respectively (It should be mention that Labrafil batches were different for all these experiments).

These remarks corroborate the idea that the driven force of the phase separation here should be the solubility properties of the ethoxylated surfactants contained in Labrafils.

Very interestingly, nanoparticles having a great morphological analogy with our system have been produced by the group of D. Wouessidjewe and A. Geze [3]. But, these objects were obtained by a nanoprecipitation method which consisted of injecting an organic phase containing phospholipids (lecithin, DMPC) and alkyl (C6) cyclodextrin into an aqueous phase under magnetic stirring. Following nanoprecipitation, solvent was removed under reduced pressure. This informs us that nanoobjects with important shape similarities could be produced even with significantly different materials and preparation protocols. In the latter case, it is reasonable to consider that the diffusion - evaporation of the solubilizing solvent, which will modify the solubility of the components of interest, should take part in the formation mechanism. Once again, in absence of solvent, the equivalent trigger in our process could be only the effect of temperature on ethoxylated surfactants. Finally, it is reassuring to note that *Janus* nanoparticles formation mechanism could be enlarged to other formulations and processes and does not only depend on our complex raw materials (Labrafils).

On the Labrafils

These are different commercial products of transesterified ethoxylated vegetable oils with the trade name Labrafil. Concerning the products we used, Labrafil® M1944CS (Oleoyl polyoxyl-

6 glycerides) is obtained from partial hydrolysis and esterification of kernel oil, and Labrafil® M2125CS (Linoleoyl polyoxyl-6 glycerides) is obtained from corn oil. Annex 1 describes the difference in terms of fatty acids composition.

Three other fundamental parameters in the composition of the Labrafils must be cited here: i) the ratio between the ethoxylated fatty acids fraction and the glyceridic fraction (mono-, di- and triglyceride), ii) the proportion of monoesters versus diesters in the ethoxylated fraction and iii) the polyethoxyl chain length distribution. From the supplier information, it is only known that the glyceridic fraction is higher than 60 weight%, and then the ethoxylated fraction lower than 40%. Due to the hemisynthesis protocols, PEG chains in the Labrafils could be esterified by one or two fatty acids (at both extremities of the polymer chain), leading to two- or tri-blocks surfactants. The ratio between mono- and diesters is available in the literature for some products (Gelucire 50/13 for example) but unfortunately not for Labrafils. At last, the mean ethylene oxide group number constituting the PEG chain is 6 but the number distribution is not fully described by the supplier. This complex and partially unknown composition of the Labrafils is a strong limitation in our investigations as it is difficult to completely dissect the nanoparticles formation mechanism from a physico-chemical point of view. Thank to a collaboration with a group involved in lipidomic (LipSys², Faculty of Pharmacy, Paris-Saclay), chromatography and mass spectrometry analysis are in progress in order to significantly improved the knowledge on the composition of Labrafils and equivalent products. More than twenty species have been identified and quantified at this time.

On the impact of Gelucire 50/13 and Phospholipon

All along the manuscript and in the previous paragraphs, we focused our interest on the properties of the Labrafils. However, it is apparent from the first results of this work (Figure 2.2 b,d) that both Gelucire 50/13 and Phospholipon 90G have their own role on the *Janus* particle building. Indeed, in absence of Phospholipon 90G, mainly classical NE droplets have been obtained and the dispersion is not stable enough in absence of Gelucire 50/13. Complementary experiments in the laboratory demonstrated it is possible to substitute Phospholipon 90G by other phospholipids as DMPC or DPPC and Gelucire 50/13 by other macroglycerides having HLB >12 as polyoxyethylene (40) stearate.

This was not detailed in the chapter dealing with hydrophilic ferrofluids but some additional investigations have been done on Gelucire 50/13 and Phospholipon 90G in order to understand

the influence of some parameters such as pH on the process feasibility. Indeed, because FF-PAAMA and FF-PAA are more stable at pH 10 than pH 7 or 5.5, first incorporation trials were made in basic conditions. It was possible to obtain stable dispersions at pH 10 but the two compartments of the JNP were dissociated. Indeed, on cryo-TEM pictures, independent oil droplets (dark) and uni- or multi-lamellar vesicles were clearly visible. Structural investigations have been done on Synchrotron beamline (Elettra, Trieste, Italy) which allows to reach larger lamellar period than the laboratory equipment. The beam intensity is also advantageous to identify structures as micelles or non-lamellar organizations, i.e. cubic or hexagonal phases. Compared to pure water, the structural behavior of one of the formulation stabilizer, Gelucire® 50/13, is affected by the pH. At the same hydration rate (80%), this macroglyceride self-organizes into a lamellar structure ($d = 158 \text{ \AA}$) at pH 10 while the SAXS profile in pure water (pH~5.5) suggests the presence of discrete structures into the sample as already observed in the laboratory [4]. A modification of the packing parameter of the Gelucire® 50/13, which is the main constituent of the JNP interfacial layer should result on curvature constrains and possibly on the separation of the compartments. The results at pH 10 are significantly different to that in pure water or pH 7 which are totally compatible with the preparation process [5]. For its part, the structural behavior of Phospholipon 90G was not significantly modified by the hydration media we investigated as the lamellar phases we got in all the cases had periods of 64.3 \AA , 64.2 \AA and 64.7 \AA for pure water, pH 7 and pH 10 solutions respectively.

To better understand these mysterious *Janus* nanoparticles, notably why the two compartments appear separated in some conditions (of pH here), studies on packing parameters should be a possible strategy. Indeed, this packing parameter describes the shape of surfactants and allows to give an idea of the self-assemblies generated by surfactants. Thus, this parameter should be around 1 to produce lamellar structures while a parameter $\sim 1/3$ leads to spherical object with high local curvatures. In other words, it means that in our system, the sum of the surfactants constituting the bilayer around the aqueous compartment should have a mean packing parameter ~ 1 . This mean packing parameter would be of course dependent on the presence of Phospholipon 90G in the mixture or on the temperature, pH and ionic strengths for ethoxylated surfactants coming both from Gelucire 50/13 and Labrafils.

On hydrophilic FF incorporation

The results of the second experimental chapter clearly showed that incorporation of hydrophilic FF into the aqueous compartment of the *Janus* particles is very limited, maybe impossible, when FF are incorporated in the aqueous phase during the preparation particles. By analogy with liposomes, it is maybe possible to envisage a post-loading into preformed *Janus* particles. Ionic gradient methods have been often used for this purpose [6]. However, due to the size of the FF grains, they seem not adapted here and it would be more consistent to consider methods which would generate transient alteration and pores in the layer surrounding the aqueous compartment. Lyophilization / rehydration cycles, congealing / decongealing cycles and electroporation could be of great interest here. Some freeze-drying tests were carried out. First without any cryoprotectant, a partial dehydration was observed and the samples had a compact appearance. Other trials were made with different cryoprotectants : mannitol 5%, 10%, 15% ; glucose 5%, 10%, 15% ; saccharose 10% with all the same result : a good dehydration occurred but the redispersion was not possible and aggregates appeared. Studies should be pursued in this area.

On hydrophobic FF incorporation

Hydrophobic FF stabilized with phospho-ester like surfactant (BNE) clearly gave the most promising results during this PhD thesis. From the diagnostic application point of view, the next step will be *in vivo* magnetic resonance imaging. Concerning the therapeutic application, the challenge is now to encapsulate an API in the hydrophilic compartment. Most of the encapsulation trials made in the laboratory deal with encapsulation of hydrophobic molecules. Thus, molecules such as chloroxylenol, triclosan or quercetin ($\log P > 2$) were efficiently encapsulated and protected in the lipid compartment of the *Janus* nanoparticles. Preliminary experiments with hydrophilic molecules, caffeine or a short peptide, have shown that the presence of these exogenous molecules did not interfere with the particle formation as anisotropic particles were still obtained at the end of the process. However, the ratios between encapsulated and non-encapsulated API have to be quantified. Regarding the results obtained with the hydrophilic FF, i.e. the absence of grain flux during the phase separation, the molecular weight of the hydrophilic API could appear as a critical parameter and should be considered with care. Hyaluronic acids, with different molecular weights, are good candidates to investigate this aspect.

On IV administration

To conclude this general discussion, the route of administration must be commented out, especially the toxicity of raw materials and the dispersing vehicle used.

The excipients incorporated in our nanoparticles have different levels of approval from the pharmaceutical authorities. Attested by their use as NE stabilizers or in liposomes for parenteral administration, phospholipid mixtures are approved for IV route. As of today, the Labrafils were approved for oral and topical applications in European Pharmacopeia while the US Pharmacopeia allows the injection of « PEG vegetable oils » at a maximum concentration of 5% (7% for IM and SC routes) (Labrafils Regulatory Data Sheet, Gattefossé). At last, in previous works from the laboratory (unpublished data), Gelucire 50/13 has been used, also with Phospholipon 90G and at the same concentration than in *Janus* particles, to stabilize solid lipid nanoparticles. These nanoparticles were non-cytotoxic (MTT test) until a total concentration of 200 µg/mL and were well tolerated after IV administration in mice (1g of nanoparticles/kg). Of course, all these data have to be confirmed on *Janus* nanoparticles but they are encouraging.

Because the osmolarity will be of prime importance in case of parenteral administration, preliminary experiments have been done by substituting pure water, used in the original process, by NaCl solution (150 mM) or citrate buffer (pure or containing citrated-FF). Unfortunately, the preparation became very unstable and it was not possible to achieve a good dispersion in these conditions. Thus, the ionic strength of the aqueous phase seems to be also a critical parameter of the process as salts and buffers have a strong effect on the physical stability of the final dispersions which tend to macroscopically separate with time. Synchrotron investigations have been done on Gelucire 50/13 and Phospholipon 90G to clarify the effect of salts and/or ionic strength on their structural organization. Within the studied concentration ranges (max. 150 mM) and for both ion type (NaCl, citrate), we did not observe significant structural modification of both excipients compared to their behavior after hydration with pure water (“On the impact of Gelucire 50/13 and Phospholipon” section of this discussion). The diffraction peaks slightly shifted but the types of structure were similar suggesting this could probably not explain the instability of the dispersion in presence of ions and buffers.

To deepen this problematic, it would be necessary now to investigate inversion phase phenomena due to the temperature. Indeed, it is well known that most of salts and buffers strongly decrease phase inversion temperature [7] and would totally modify the “equilibrium”

during our preparation process. The ethoxylated surfactants from Labrafils will be more hydrophobic than hydrophilic on larger range of temperature (Phase inversion temperature $\ll 40^{\circ}\text{C}$). Preliminary surface tension measurement results go in this direction.

As it is not possible to prepare *Janus* nanoparticles directly into buffer / saline solutions with our current knowledge, we considered the dilution of the preformed nanoparticles into saline solution. With a 150 mM NaCl solution, cryo-TEM observations clearly indicated that the two compartments of blank nanoparticles were still stuck together, but with shrinkage of the aqueous one. Perfectly known for natural cells as red blood cells, this phenomenon is also documented for liposomes under hyperosmotic stress [8]. Of course, it needs to pay special attention to this problem for further development of our particles for IV administration, as it could induce leakage of the encapsulated API from the hydrophilic compartment to blood stream. This uncontrolled release would also depend on the API properties.

References

- [1] Tran L-T-C, Lesieur S, Faivre V. Janus nanoparticles: materials, preparation and recent advances in drug delivery. *Expert Opin. Drug Deliv.* 2014;11:1061–1074.
- [2] Sjöblom J, editor. *Emulsions and emulsion stability*. 2nd ed. Boca Raton: Taylor & Francis; 2006.
- [3] Geze A, Choisnard L, Demé B, et al. Toward a better understanding of the structure of amphiphilic cyclodextrins bCDA / phospholipid-based nanoaggregates. Montpellier; 2004.
- [4] El Hadri M, Achahbar A, El JK, et al. Lyotropic behavior of Gelucire 50/13 by XRD, Raman and IR spectroscopies according to hydration. *Chem. Phys. Lipids.* 2016;200:11–23.
- [5] Millart E, Faivre V. Janus nanoparticles: Formation mechanisms and destabilization. *Annu. Rep. ELETTRA Austrian SAXS Beamline*; 2015.
- [6] Gubernator J. Active methods of drug loading into liposomes: recent strategies for stable drug entrapment and increased in vivo activity. *Expert Opin. Drug Deliv.* 2011;8:565–580.
- [7] Dong R, Hao J. Complex Fluids of Poly(oxyethylene) Monoalkyl Ether Nonionic Surfactants. *Chem. Rev.* 2010;110:4978–5022.
- [8] Ménager C, Cabuil V. Reversible Shrinkage of Giant Magnetoliposomes under an Osmotic Stress. *J. Phys. Chem. B.* 2002;106:7913–7918.

GENERAL CONCLUSIONS AND PERSPECTIVES

In the field of drug delivery, theranostic nanocarriers and FDC products necessitate the improvement of ingenious carriers able to co-encapsulate several compounds of interest. *Janus* nanoparticles are one of the interesting carriers because it is a promising system to implement the requirements needed in drug delivery among many nanotechnologies such as liposomes, polymer particles, ...

In the context of this study, the first aim was to investigate the possibility to produce *Janus* nanoparticles with a scalable process and only with marketed and pharmaceutically approved lipid-based excipients. Different lipid phases have been combined into the formulations. The nanoparticles have been characterized from their long-term physical stability such as size, zeta potential, microscopic structure and supramolecular organization. In this PhD thesis, a focus has been done on the formation mechanism.

The second goal of this work was to elaborate a hydrophilic ferrofluid and to encapsulate it in the aqueous compartment of *Janus* nanoparticles. The compatibility between aqueous ferrofluids and the HPH process used to make the *Janus* nanoparticles was evaluated in term of stability of the nanodispersions. Two polymers, PAA and PAAMA were chosen as the best stabilizers to coat the nude maghemite in aqueous medium. Several physicochemical characterizations were performed in order to show the grafting between the polymers and the iron core of the maghemite and also to demonstrate that the integrity of the iron oxide core is preserved after coating with polymers. After some aqueous encapsulation trials, we found that the maghemite grains are not incorporated into the *Janus* nanoparticles but the formation mechanism of these particles, based on a temperature dependent phase separation, is conserved in the presence of ferrofluid.

The third purpose of this thesis was to prepare a hydrophobic ferrofluid compatible with the lipid compartment of the *Janus* nanoparticles. Two lipid stabilizers were grafted on the surface of nude maghemite : a fatty acid (OA) and a phospho-diester like surfactant (BNE). After some characterizations, we found that the BNE was a better stabilizer in term of stability than the OA justifying why FF-BNE was chosen to be encapsulated in the lipid part of the *Janus* nanoparticles. Once purified by centrifugation, the magnetic *Janus* nanoparticles were found to have much higher r_2/r_1 ratio than those of commercial contrast agents allowing us to qualify our system as a good candidate for MRI contrast agent. Magnetization experiments done on the purified particles demonstrated that the superparamagnetism behavior of the SPION is preserved after encapsulation in the *Janus* nanoparticles.

In conclusion, the general aim of the present thesis was to propose a formation mechanism of the *Janus* nanoparticles, to incorporate a diagnostic agent in one or the other of the two compartments and to characterize the new objects obtained.

Regarding the perspectives at short term, we got good results in relaxometry measurements and it could be interesting to evaluate the magnetophoretic mobility of the magnetic *Janus* nanoparticles and the SPL respectively to demonstrate their ability to do magnetic targeting and hyperthermia treatment. The main advantage of the *Janus* nanoparticles is their capacity of co-encapsulate a hydrophilic and a hydrophobic compound. The next step would be to incorporate a hydrophilic drug in the aqueous compartment of the *Janus* nanoparticles whereas the SPION would be entrapped in the lipid part in order to obtain a new theranostic tool.

In the longer term, the *Janus* nanoparticles are intended to be administered to the patient by injection. Thus, it could be favorable to carry out some *in vitro* experiments to determine the cytotoxicity of the nanoparticles and their stability in biologically relevant media.

ANNEX

1. Lipids

Lipid phases (Labrafils) used in this work are based on polyoxylglycerides (or macroglycerides). They were supplied as gift samples from Gattefossé S.A. (Saint-Priest, France).

These are several marketed products of transesterified ethoxylated vegetable oils with the trade name Labrafil [1]. In the present work, we used Labrafil[®] M1944CS (Oleoyl polyoxyl-6 glycerides), obtained from kernel oil, and Labrafil[®] M2125CS (Linoleoyl polyoxyl-6 glycerides), obtained from corn oil. Both of them contain a mean of 6 ethoxy units. Table A1 summarizes the composition and most important physicochemical properties of both products (data from the supplier).

Table A.1. Properties of Labrafil[®] M1944CS and Labrafil[®] M2125CS

Properties	Labrafil[®] M1944CS	Labrafil[®] M2125CS
Composition		
Palmitic acid (C16)	4.0 to 9.0 %	4 to 20%
Stearic acid (C18)	≤ 6.0 %	≤ 6.0 %
Oleic acid (C18:1)	58.0 to 80.0 %	20.0 to 35.0%
Linoleic acid (C18:2)	15.0 to 35.0 %	50.0 to 65.0%
Linolenic acid (C18:3)	≤ 2.0 %	≤ 2.0 %
Arachidic acid (C20)	≤ 2.0 %	≤ 1.0 %
Eicosenoic acid (C20:1)	≤ 2.0 %	≤ 1.0 %
Physical form	Liquid at 40 °C	Liquid at 45 °C
Viscosity at 20 °C	75 to 95 mPa.s	70 to 90 mPa.s
HLB	4	4
Acid number	≤ 2.00 mg KOH/g	≤ 2.00 mg KOH/g
Saponin number	150 to 170 mg KOH/g	150 to 170 mg KOH/g
Iodine number	75 to 95 g I ₂ /100g	90.0 to 110.0 g I ₂ /100g
Solubility	Very soluble in methylene chloride; soluble in n-hexan Insoluble in ethanol Dispersed in water	Soluble in chloroform, methylene chloride Insoluble in ethanol Dispersed in water

2. Surfactants

2.1. Gelucire® 50/13

Gelucire® 50/13 was kindly gift from Gattefossé S.A. (Saint-Priest, France). This excipient composes primarily a mixture of poly(ethyleneglycol) (PEG) 1500 mono- and diesters with palmitic (C16) and stearic (C18) acid with a mean HLB value about 13 [2]. It is adaptable to a variety of formulation process and can be used, among others, for the development of solid dispersions of hydrophobic drugs in order to improve their oral bioavailability [3–6].

2.2. Phospholipon® 90G

Phospholipon® 90G was received as a gift sample from Phospholipid GmbH (Nattermannalle, Germany). This is a purified, de-oiled, and granulated soy lecithin with a high phosphatidylcholine content (94-100%), lysophosphatidylcholine (max. 4%) and tocopherol (0.3%). It is used as raw material forming of liposomes and mixed micelles, moisturizer, emulsifier for pharmaceutical dermatology, cosmetics and personal care products. It is also used as a solubilizer for drugs and encapsulation of active compounds

References

- [1] Fiedler HP, editor. Lexikon der Hilfsstoffe für Pharmazie, Kosmetik und angrenzende Gebiete. Aulendorf i. Württ: Ed. Cantor; 1971.
- [2] Khan N, Craig DQM. The influence of drug incorporation on the structure and release properties of solid dispersions in lipid matrices. *J. Controlled Release.* 2003;93:355–368.
- [3] Passerini N, Perissutti B, Moneghini M, et al. Characterization of carbamazepine–Gelucire 50/13 microparticles prepared by a spray-congealing process using ultrasounds. *J. Pharm. Sci.* 2002;91:699–707.
- [4] Vippagunta SR, Maul KA, Tallavajhala S, et al. Solid-state characterization of nifedipine solid dispersions. *Int. J. Pharm.* 2002;236:111–123.
- [5] Fini A, Moyano JR, Ginés JM, et al. Diclofenac salts, II. Solid dispersions in PEG6000 and Gelucire 50/13. *Eur. J. Pharm. Biopharm.* 2005;60:99–111.
- [6] Qi S, Marchaud D, Craig DQM. An investigation into the mechanism of dissolution rate enhancement of poorly water-soluble drugs from spray chilled gelucire 50/13 microspheres. *J. Pharm. Sci.* 2010;99:262–274.
- [7] Ash M, Ash I. Handbook of green chemicals. 2. ed. Endicott, NY: Synapse Information Resources, SIR; 2004.

Titre : Nanoparticules lipidiques de type *Janus* à compartiment superparamagnétique : du procédé de mise en œuvre aux applications théranostiques

Mots clés : BNE, homogénéisation haute pression, nanoparticules *Janus* lipidiques, OA, PAA/PAAMA, SPION

Résumé : Depuis quelques années, notre laboratoire développe des nanoparticules lipidiques bicompartimentées originales produites par homogénéisation haute pression, un procédé transposable à grande échelle, à partir d'excipients pharmaceutiques validés par différentes pharmacopées (Eur., USP, JP).

Ces particules appartiennent ainsi à la famille des nano-objets *Janus* puisqu'elles sont organisées en deux sous-structures juxtaposées : une moitié est constituée d'une gouttelette huileuse alors que l'autre moitié est composée d'une structure vésiculaire et renferme un cœur aqueux délimité par une bicouche phospholipidique.

En plus de la biocompatibilité intrinsèque des lipides constitutants, un tel système représente un outil potentiellement très intéressant et

valorisable du point de vue pharmaceutique et biomédical capable d'incorporer séparément et de co-véhiculer des substances hydrophiles et lipophiles aux activités distinctes, par exemple un agent d'imagerie médicale et un principe actif pour coupler diagnostique et thérapie.

Ici, nous nous sommes intéressés à charger les nanoparticules *Janus* avec un fluide magnétique composé de nanocristaux d'oxyde de fer (ferrofluide, FF), actif en tant qu'agent de contraste efficace en IRM, étant magnétiquement contrôlable et permettant d'envisager un traitement par hyperthermie.

Tour à tour, des FF hydrophiles ou lipophiles compatibles avec le procédé de production ont été développés en étudiant différentes voies de stabilisation des nanocristaux en fonction du compartiment d'encapsulation.

Title : Lipid-based *Janus* nanoparticles with superparamagnetic compartment : from the implementation process to the theranostic applications

Keywords : BNE, high pressure homogenization process, *Janus* lipid nanoparticles, OA, PAA/PAAMA, SPION

Abstract : In recent years, our team has developed original compartmented lipid nanometer-sized particles produced by high pressure homogenization, a scalable process, with pharmaceutically approved excipients.

The particles actually belong to the family of *Janus* nano-objects as they are organized in two juxtaposed substructures : one half is a droplet of liquid-state lipids while the other half is vesicle-like and encloses an aqueous core delimited by a phospholipid-containing bilayer shell.

Added to the intrinsic biocompatibility of the constituting lipids, such a system provides a potentially very valuable tool in pharmaceutical and biomedical fields, able to separately

incorporate and co-convey hydrophilic and lipophilic substances with distinct activities, for example, a medical imaging agent and a drug for coupling diagnosis and therapy.

Here, we are interested in loading *Janus* nanoparticles with a magnetic fluid composed of superparamagnetic iron oxide nanocrystals (ferrofluid, FF), indeed as efficient contrast agent for magnetic resonance imaging (MRI), being magnetically targetable and providing ability for hyperthermia treatment.

Alternately, hydrophilic or lipophilic FF compatible with the production process have been developed by investigating different stabilization pathways of the nanocrystals depending on the encapsulation compartment.

